EXPERIMENTAL EVALUATION OF AN ANALYSIS FRAMEWORK FOR SIMULATING THE COUPLED BEHAVIOR OF SHAPE MEMORY ALLOY-BASED MORPHING RADIATORS

A Thesis

by

CHRISTOPHER LIONEL BERTAGNE

Submitted to the Office of Graduate and Professional Studies of
Texas A&M University
in partial fulfillment of the requirements for the degree of

MASTER OF SCIENCE

Chair of Committee,	John Whitcomb
Co-Chair of Committee,	Darren Hartl
Committee Member,	William Schneider
Head of Department,	Rodney Bowersox

August 2016

Major Subject: Aerospace Engineering

ABSTRACT

Thermal control is an important aspect of spacecraft design, particularly in the case of crewed vehicles, which must maintain a precise internal temperature at all times in spite of sometimes drastic variations in the external thermal environment and internal heat loads. The successes of the Apollo, Space Shuttle, and International Space Station programs have shown that this can be accomplished for short-term missions to the Moon and long-term missions to Low Earth Orbit (LEO); however, crewed spacecraft traveling beyond LEO are expected to encounter more challenging thermal conditions with significant variations in both the heat rejection requirements and environment temperature. Such missions will require radiator systems with high turndown ratios, defined as the ratio between the maximum and minimum heat rejection rates achievable by the radiator system. Current radiators are only able to achieve turndown ratios of 3:1, far less than the 12:1 turndown ratio which is expected to be required on future missions. An innovative radiator concept, known as a morphing radiator, uses the temperature-induced shape change of shape memory alloy (SMA) materials to achieve a turndown ratio of at least 12:1. Predicting the behavior of morphing radiators requires analysis tools that are capable of accurately representing the driving physics. However, developing mathematical and computational models of morphing radiators is challenging due to the presence of a unique type of two-way thermomechanical coupling. This coupling is not present in traditional, fixed-geometry radiators and has not been widely considered in the literature. Furthermore, although many existing simulation tools are capable of analyzing certain types of thermomechanically coupled problems, general problems involving radiation and deformation cannot be modeled natively in these tools. This work presents an analysis framework which has been developed to overcome these present shortcomings. Several

example problems are used to demonstrate the ability of the framework to simulate realistic problems involving morphing radiators. In addition, a prototype morphing radiator was designed, fabricated, and subsequently tested in a thermal environment similar to one in which the radiator is expected to operate on a future mission. Following the experimental study, a detailed finite element model of the prototype was developed and executed using the framework. In spite of some discrepancies resulting from shortcomings in the SMA constitutive model, the model predictions generally agree with the experimental data, giving confidence that the framework is able to accurately represent the thermomechanical coupling present in morphing radiators.

To my family

ACKNOWLEDGMENTS

I would like to begin by expressing my deepest gratitude to my parents for their unfailing support. They have always encouraged me to pursue my passions and have instilled in me a sense of determination that has served me well during my time as a graduate student. Next, I would like to thank Dr. Hartl, as I would not be where I am today if it were not for his guidance and inspiration. I first met Dr. Hartl during my penultimate semester as an undergraduate, when I took a particular structural analysis and design elective (AERO 405) which he taught that semester. I learned many lessons in AERO 405, including why I shouldn't pull all-nighters to finish projects. The following semester, I approached Dr. Hartl to do undergraduate research with him and he presented me with a choice of several projects to work on. One of those projects involved modeling morphing radiators and would go on to become the project described in this thesis. My committee members, Dr. Whitcomb and Dr. Schneider, have also provided valuable feedback at several key points and I am grateful for their input. I must also acknowledge Thomas Cognata, Darren Hartl, and Rubik Sheth for their initial work on the morphing radiator concept in 2013, which was funded under a grant from the Space Technology Mission Directorate (STMD) at NASA. Their preliminary findings helped pave the way for my fellowship application later that year. I would also like acknowledge the following students who helped me in various ways throughout my graduate career: Keith Ballard, Jorge Chong, Austin Cox, Edwin Peraza-Hernandez, Brian Lester, Miranda Nelson, Roger Ramirez, John Rohmer, and Rob Wheeler. Finally, I would like to acknowledge the funding I have received through the NASA Space Technology Research Fellowship (NSTRF) program under grant NNX14AM44H. I must also acknowledge the following individuals at NASA Johnson Space Center for their invaluable assistance in completing my work:

James Brown, Lisa Erickson, Scott Hansen, Moses Navarro, Karen Pickering, Matt Ruane, Joe Settles, Rubik Sheth, Fred Smith, and Eugene Ungar.

TABLE OF CONTENTS

Page

LIST OF FIGURES

FIGURE Page

LIST OF TABLES

TABLE Page

1. INTRODUCTION

On April 12, 1961, cosmonaut Yuri Gagarin became the first human to fly in space when he completed an orbit of the Earth in his Vostok I spacecraft. Less than one month later, Alan Shepard became the first American astronaut in space and shortly thereafter, John Glenn became the first American to complete an orbit of the Earth. In the 55 years that have followed, numerous innovations have made longer manned spaceflights possible. 1971 saw the launch of the first space station, Salyut I, operated by the Soviet Union; the United States' first space station, Skylab, was launched several years later and flew until 1979. The Russian space station Mir, which remained in Low Earth Orbit from 1986 to 2001, was the first space station intended for long-term stays; the record for the longest spaceflight (437 days) was set by a Russian cosmonaut onboard Mir. In 1998, construction began on the International Space Station, which has been continuously occupied since November 2, 2000 and is expected to remain in operation until 2024 or later.

In 1968, Frank Borman, James Lovell, and William Anders became the first humans to travel beyond Low Earth Orbit (LEO) when they completed ten orbits of the Moon during the Apollo 8 mission. However, since the final Moon landing in 1972, no human has traveled beyond Low Earth Orbit. In recent years, there has been considerable interest in manned space missions beyond LEO: NASA and other organizations are planning return missions to the Moon as well as subsequent manned missions to Mars [45]. Unlike the Apollo spacecraft, which were designed for short-duration missions, future crewed spacecraft will be required to support long-duration missions with little to no resupply capability. There are a number of technical challenges which must be overcome in order to make long-term missions such as these safe and affordable; NASA has published a series of documents outlining

the specific technology areas in which further development is needed in order to enable long-term crewed missions beyond Low Earth Orbit. This work focuses on developments in one of those technology areas, namely that of *thermal control.*

Modern crewed spacecraft are composed of a number of systems which must interact in order to ensure the overall success of the mission. Examples of spacecraft systems include the structures system, which provides mechanical support to all other systems; the power system, which supplies electrical power to the spacecraft; and the propulsion system, which allows the spacecraft to change its velocity and orientation [68]. One of the most important systems onboard every spacecraft is the *thermal control system* [18, 68], sometimes known as the *thermal management system* [46]. The primary task of the thermal control system (TCS) is to maintain the temperature of all equipment as well as any occupants onboard within acceptable ranges over the entire course of the mission [46]. The TCS must be able to accomplish this goal in spite of any variations in the external thermal environment and internal heat loads from the other systems, as exceeding the temperature limits can result in damage to the other systems, potentially leading to mission failure.

The thermal control system is a particularly important aspect of crewed spacecraft, as crewed vehicles must be able to maintain a precise cabin temperature between 20 and 25°C at all times to ensure crew safety and comfort [68]. Although the Apollo, Space Shuttle, and International Space Station programs have demonstrated that this can be accomplished for short-duration missions to the Moon and long-duration missions to Low Earth Orbit, future human-rated spacecraft designed for long-term missions beyond LEO are expected to experience large variations in the external thermal environment. As a result, these spacecraft will face a more challenging set of thermal control requirements. In many cases, the heat rejection needs will be contrary to the capacity of the thermal environment, i.e., the TCS will be required to reject a

high heat load to a warm orbital environment and a low heat load to colder transit environments. For example, the mission profile for the now-canceled Altair lunar lander would have required the TCS to reject 500 W to an environment at 4 K during cruise and 4,500 W to an environment at 215 K during surface operations [17]; future crewed missions to Mars are expected to encounter a similar set of requirements. This non-fortuitous relationship between the thermal environment and the heat rejection needs at the spacecraft level requires a radiator system with a high *turndown ratio*. The turndown ratio, defined as the ratio between the maximum and minimum heat rejection capabilities of the TCS [60], is one of the primary measures of overall TCS performance. Future missions beyond Low Earth Orbit are predicted to require turndown ratios of approximately 12:1 [49]. Current radiator systems, which are only able to achieve turndown ratios of 3:1 [46], are generally sized for the maximum heat rejection requirement in the warmest continuous environment. This ensures the spacecraft will never overheat; however, a radiator designed in this manner will be oversized for periods of low heat rejection and is prone to freezing [49]. TCS design is further complicated by the need to transport heat from crewed internal portions of the vehicle to the radiators without risking crew exposure to toxic working fluids.

The aforementioned factors drive the current state-of-the-art TCS architecture for crewed vehicles: a two-fluid-loop heat transport system in conjunction with body-mounted or deployable radiators [46]. Figure 1.1 shows a simplified schematic of a two-fluid-loop thermal control system: an inner loop acquires heat from the cabin and an outer loop circulates fluid through the radiator system; an interface heat exchanger allows the two loops to exchange heat while remaining physically isolated from each other. This architecture allows a nontoxic working fluid (e.g. propylene glycol-water solution) to be used in the inner loop and a low-freezing-point coolant (most of which are highly toxic) to be used in the radiator system. Although the two-loop

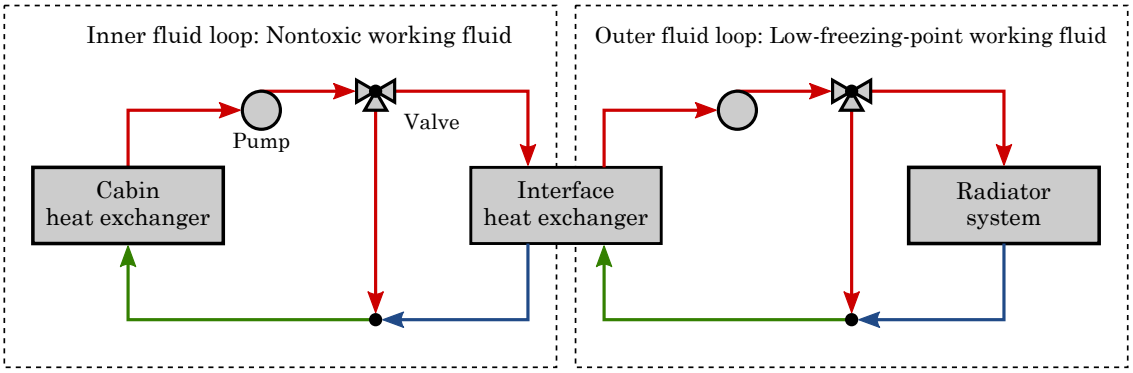

Figure 1.1: Schematic of a dual-fluid-loop thermal control system with a traditional radiator system.

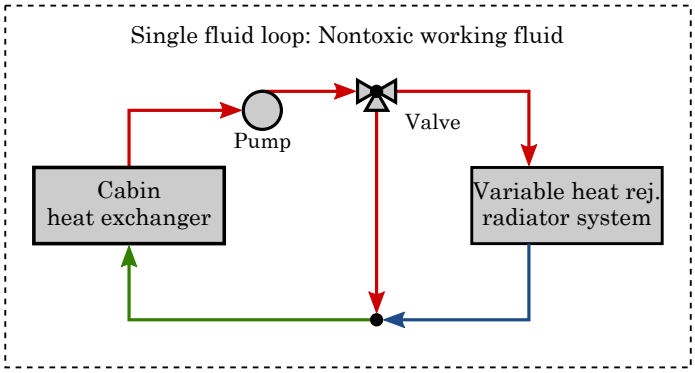

Figure 1.2: Schematic of a single-loop thermal control system with a variable heat rejection radiator system.

design achieves a sufficiently high turndown ratio while avoiding crew exposure to toxic fluids, it does so at the expense of increased system mass and complexity due to the additional hardware required (e.g. pumps, heat exchangers, etc.); previous trade studies have shown that a two-loop TCS is approximately 25% heavier than a similarly-performing single-loop system, such as that shown in Fig. 1.2 [49].

There have been a number of efforts to improve TCS performance by developing *variable heat rejection radiators* [27]. Examples include digital radiators [17, 42], roll-

out fin radiators [33, 55], variable-emissivity radiators [1], and freezable radiators [60]. A recently-proposed radiator known as a *variable-geometry*, or *morphing* radiator achieves variable heat rejection via shape change [8]. Such a design would employ the temperature-dependent phase change of shape memory alloy (SMA) materials to reconfigure a radiator's shape and thus adapt the rate of heat rejection to evolving vehicle requirements. This type of radiator can achieve the high turndown ratios necessary to enable single-loop thermal control of a vehicle using a nontoxic, high-freezing-point working fluid.

Shape memory alloys are metallic materials that exhibit a temperature-activated, diffusionless phase transformation between two solid phases known as *martensite* and *austenite*. This phase transformation can be used to create solid-state actuators which are capable of generating approximately 5% actuation strain at stresses on the order of 500 MPa. SMA actuators have already been successfully deployed in a number of aerospace applications [24, 30]. Examples include stepper motors for solar flaps onboard a satellite [66, 19], variable geometry chevrons [23, 40, 5, 24] and slat-cove fillers onboard transport aircraft [64, 65], torque tubes for twisting aircraft wings [24], and deployment mechanisms for solar arrays onboard a satellite [7, 19, 69]. Shape memory alloys are ideally suited for constructing morphing radiators, as the inherent temperature dependence of the material allows the radiator to reconfigure passively with no need for external power, control, or sensing instrumentation.

Figure 1.3 shows a morphing radiator design, known as the *flexible* design, which combines the response of shape memory alloy material with a thermally conductive and linearly elastic biasing structure to create a radiator panel that reconfigures passively in response to changes in temperature [8]. The radiator consists of a circular composite panel fixed to the spacecraft along the panel's line of symmetry. The panel is given a high-emissivity coating on the inner (concave) surface, shown with

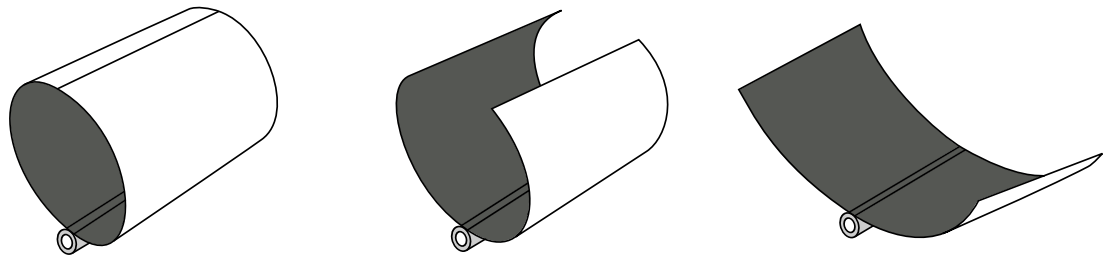

(a) Closed shape for minimum heat rejection.

(b) Semi-open shape for intermediate heat rejection.

(c) Open shape for maximum heat rejection.

Figure 1.3: Schematic representation of a flexible morphing radiator panel. Light and dark shading represents low- and high-emissivity coatings, respectively.

dark shading, and low-emissivity coating on the outer (convex) surface, shown with light shading. A shape memory alloy sheet attached to the outermost surface of the panel allows the radiator to morph between various shapes depending on the temperature of the panel. When sufficiently cold, the radiator takes on the circular shape shown in Fig. 1.3a. As the temperature in the radiator increases due to a warmer ambient environment and/or increase in the heat load, the SMA begins to open the radiator to an intermediate configuration, such as that shown in Fig. 1.3b. Figure 1.3c shows the fully-open, maximum-heat-rejection shape. This morphing behavior is fully reversible: a subsequent decrease in temperature will cause the radiator to return to the minimum-heat-rejection shape.

Figure 1.4 shows a potential design of a radiator system which incorporates a number of individual SMA-actuated morphing panels. In this design, warm fluid from the cabin enters the radiator system via an inlet header, shown in red. The inlet header distributes the fluid to several parallel flow tubes to which a number of morphing radiator panels are attached. At the end of the flow tubes, an outlet header collects the now-cooled fluid and returns it to the cabin. This design allows

each radiator panel to respond to the local fluid temperature at its attachment point. In high heat rejection mission phases, all of the panels would take on the open shape to maximize the heat rejection; this state is shown in Fig. 1.4a. Figure 1.4b shows an intermediate heat rejection scenario, in which the panels near the outlet header begin to close to minimize the heat rejection once the working fluid has reached the desired temperature. Figure 1.4c shows the minimum heat rejection shape, corresponding to low heat rejection mission phases, in which all of the panels are in the closed, circular configuration.

Figure 1.5 shows an alternate morphing radiator system, known as the *rigid* design, consisting of two rigid radiator panels, each of which is actuated by two coaxial shape memory alloy torque tubes. Warm fluid from the spacecraft cabin would flow through the inner torque tube and circulate through the radiator panel. The cooled fluid then flows back to the spacecraft through the annular region between the two torque tubes. Insulation placed around the inner torque tube prevents heat from being transferred from the warm inlet fluid to the cool return fluid through the torque tube. As in the previous design, one side of each panel is given a high-emissivity coating while the opposite side is given a low-emissivity coating. The torque tubes allow the rigid panels to rotate in response to changes in temperature. During periods of high heat rejection, the torque tubes would orient the panels horizontally as shown in Fig. 1.5a, which maximizes the view of the high emissivity surface to space and results. As the fluid temperature decreases, the torque tubes would begin to rotate the panels toward each other, as shown in Fig. 1.5b. During periods of low heat rejection, the radiator would take on the fully-closed configuration shown in Figure 1.5c, which minimizes the view of the high emissivity surface to space.

Both morphing radiator designs—the flexible design shown in Fig. 1.4 and the rigid design shown in Fig. 1.5—will tend to maintain a fluid outlet temperature in

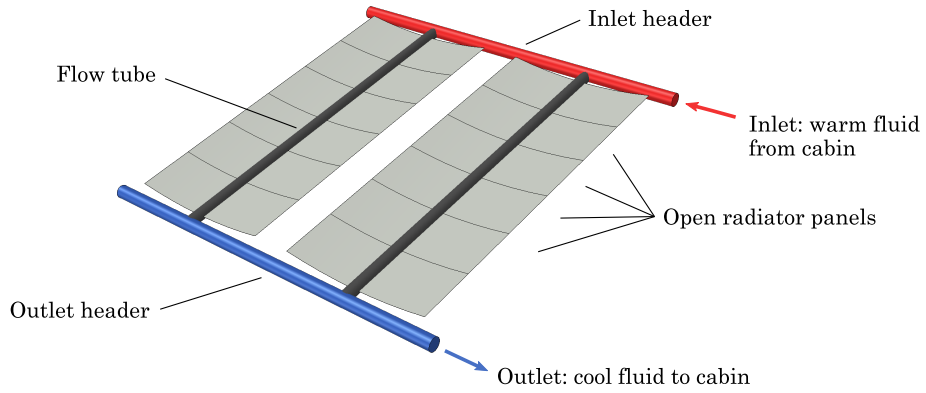

(a) Maximum heat rejection: all panels fully open.

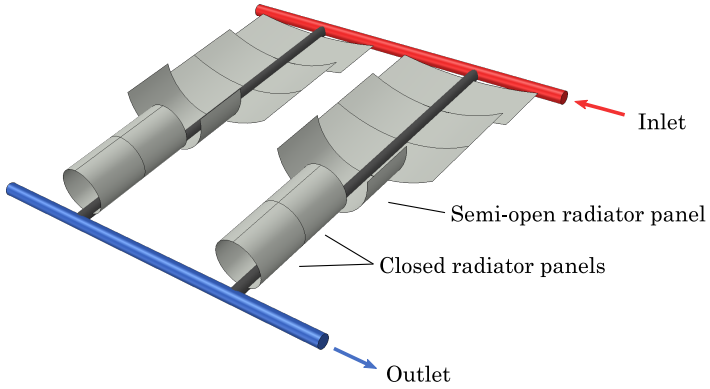

(b) Intermediate heat rejection: some panels open; some panels closed.

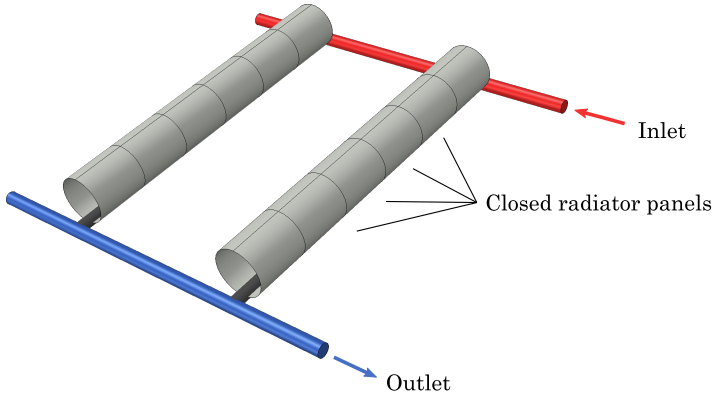

(c) Minimum heat rejection: all panel fully closed.

Figure 1.4: Proposed morphing radiator system showing inlet and outlet headers and parallel flow tubes with multiple morphing radiator panels attached.

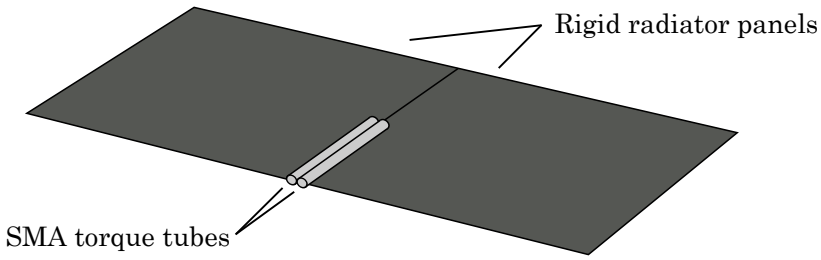

(a) Maximum heat rejection: panels fully open.

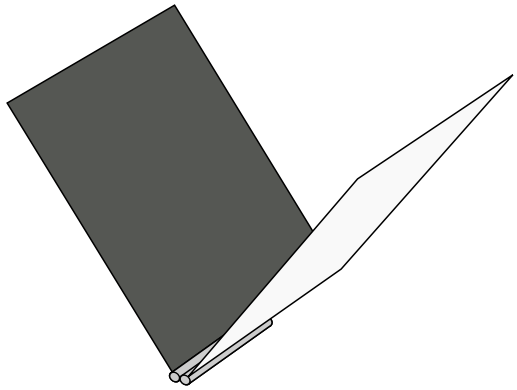

(b) Intermediate heat rejection: panels partway open.

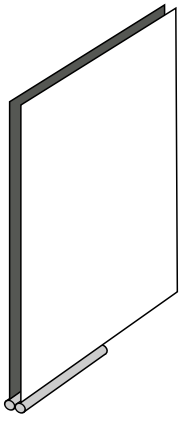

(c) Minimum heat rejection: panels fully closed.

Figure 1.5: Alternate morphing radiator system design consisting of two rigid radiator panels actuated by torque tubes. Light and dark shading represents low- and high-emissivity coatings, respectively.

the range of the transformation temperatures of the SMA material (between A_f and M_f), a behavior that can simplify the design of the TCS. These designs also have the potential to achieve turndown ratios of at least 12:1 [8], far exceeding the turndown ratios achievable with current state-of-the-art technology. Adopting a single-loop TCS with a morphing radiator system will reduce the TCS mass by approximately 25% while also simplifying vehicle design [49]. Thus, the SMA morphing radiator concept is truly revolutionary in its potential to improve several figures of merit simultaneously, including decreases in system mass and complexity as well as increases in reliability and versatility.

The goals of this effort are to develop, demonstrate, and evaluate analysis tools to support the design of future morphing radiator systems such as those described above. As will be shown, morphing radiators that use thermally-activated smart materials (e.g. SMAs) for actuation exhibit a complex thermomechanical coupling which arises due to the constitutive behavior of the material and the presence of geometry-dependent radiation boundary conditions. This coupling is not present in traditional, fixed-geometry radiators and has not been widely considered in the literature. Although many existing simulation tools are capable of analyzing certain types of thermomechanically-coupled problems, general problems involving radiation and non-rigid deformation cannot be modeled natively in these tools. To overcome this present shortcoming, an analysis framework has been developed which employs a technique known as a *partitioned analysis procedure* [15]. This approach is characterized by decoupling the field equations into separate thermal and structural *partitions*, each of which uses its own dedicated solver. The coupling is represented by exchanging field data between the partitions during runtime via boundary conditions. The partitioned approach is particularly advantageous as it enables existing high-fidelity analysis tools to be used to simulate general problems involving morphing radiators.

The remainder of the thesis is organized as follows: Chapter 2 provides background information regarding radiation heat transfer, describes the constitutive behavior of shape memory alloys in detail, and explains the nature of the thermomechanical coupling present in SMA morphing radiators. Chapter 3 discusses the development of the framework in detail and presents the results of several example problems which demonstrate its present capabilities. Chapter 4 describes the experimental study which considered a prototype morphing radiator. In Chapter 5, a detailed model of the prototype, which allows the physical accuracy of the framework to be evaluated, is developed and implemented. Finally, Chapter 6 concludes the thesis and provides suggestions for future work.

2. BACKGROUND AND THEORY

2.1 Thermal Radiation

Along with conduction and convection, *radiation* is one of the primary modes of heat transfer [43, 48]. In contrast to the other two modes, which transfer energy via molecular interactions, thermal radiation involves the transfer of energy via electromagnetic waves[1]. Consequently, radiation does not require a medium in order for two bodies to exchange energy. Radiation is a complex phenomenon and a complete description of its nature is beyond the scope of this thesis; for a comprehensive treatment, the reader is referred to resources such as the works of Modest [43] or Howell & Siegel [29]. Instead, this section summarizes the aspects of radiation that most pertain to this work and presents the corresponding equations.

One of the fundamental concepts in the theory of radiation is the *black body*. A black body (or surface) is defined as an object (surface) which absorbs all radiation that strikes it, regardless of the wavelength [31]. The heat flux emitted by a black body, denoted by $\dot{q}_b^e$, depends only on the fourth power of its absolute temperature T, as given by the Stefan-Boltzmann law,

$$\dot{q}_b^e = \sigma T^4, \tag{2.1}$$

where σ is the Stefan-Boltzmann constant[2]. Assuming the temperature is uniform over the body, the rate of emission, in units of power, is given by

$$\dot{Q}_b^e = \sigma A T^4, \tag{2.2}$$

[1] In general, the term "radiation" may be used to refer to electromagnetic radiation, particle radiation, or acoustic radiation. In this work, the term will be used exclusively to refer to electromagnetic radiation

[2] In SI units, $\sigma = 5.67 \cdot 10^{-8}\,\mathrm{W/(m^2{\cdot}K^4)}$.

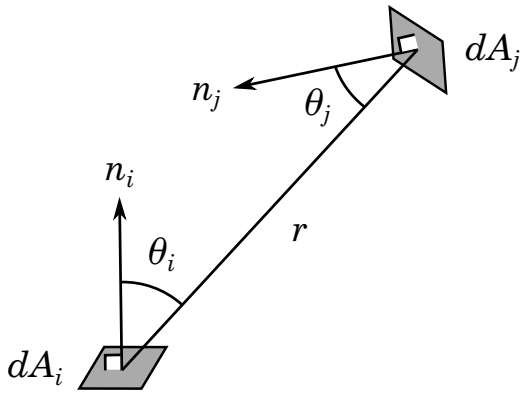

Figure 2.1: Radiative heat transfer between two differential areas.

where A is the surface area of the body. An important characteristic of radiation is its dependence on geometry, which is represented by a quantity known as the *view factor*, sometimes referred to as the *shape factor*, *angle factor*, or *configuration factor*. The view factor from surface i to surface j, which will be denoted by $F_{i\to j}$, is defined as the fraction of radiation emitted by surface i which strikes surface j directly. Note that this definition excludes any radiation that may reflect off of a third surface before reaching surface j. The view factor between two finite surfaces may be computed via

$$F_{i\to j} = \frac{1}{A_i}\int_{A_i}\int_{A_j}\frac{\cos\theta_i\cos\theta_j}{\pi r^2}dA_i dA_j, \tag{2.3}$$

where r is the distance between the differential areas dA_i and dA_j and θ_i and θ_j are defined as shown in Fig. 2.1. It is possible to evaluate this expression for certain simple geometries, and there are view factor catalogs which provide the view factor for a number of cases [29]. However, it is difficult or impossible to evaluate Eq. 2.3 analytically for general geometries. Therefore, view factors are often determined numerically rather than analytically. Note that $F_{i\to j} \neq F_{j\to i}$ in general. The correct

relationship between $F_{i\to j}$ and $F_{j\to i}$ is given by

$$A_i F_{i\to j} = A_j F_{j\to i}, \tag{2.4}$$

which is known as the *reciprocity theorem* [48]. Using the Stefan-Boltzmann law (Eq. 2.2) and the definition of view factor, the radiation emitted by an isothermal black surface i that strikes a second isothermal black surface j is given by

$$\dot{Q}^b_{i\to j} = \sigma A_i F_{i\to j} T_i^4. \tag{2.5}$$

Likewise, the radiation emitted by surface j that strikes surface i is given by

$$\dot{Q}^b_{j\to i} = \sigma A_j F_{j\to i} T_j^4. \tag{2.6}$$

Thus, by applying the reciprocity theorem (Eq. 2.4), the net rate of heat exchange from surface i to surface j can be written as

$$\dot{Q}^{net,b}_{i\to j} = \dot{Q}_{i\to j} - \dot{Q}_{j\to i} = \sigma A_i F_{i\to j}(T_i^4 - T_j^4). \tag{2.7}$$

Equations 2.5 and 2.6 imply that the two surfaces exchange energy even if they are at the same temperature, provided that $F_{i\to j} \neq 0$. However, the net exchange between the two surfaces is zero, as stated by Eq. 2.7. For a problem with N isothermal surfaces, the net radiation from surface i to the other surfaces is given by

$$\dot{Q}^{net,b}_i = \sum_{j=1}^{N} \sigma A_i F_{i\to j}(T_i^4 - T_j^4), \tag{2.8}$$

which represents a set of N equations for $2N$ unknowns (namely, the temperature and net heat transfer rate associated with each surface). An additional N equations result from a complete set of boundary conditions, in which either the temperature or net heat transfer rate (or a relationship between these quantities) is specified for each surface. Note that for a general problem involving N black surfaces, there are N^2 view factors.

Most real surfaces do not act like black bodies, therefore, a second concept is introduced: the *grey body*. A grey body (or surface) is characterized by a nondimensional term known as the *total hemispherical emissivity* or simply *emissivity*, $0 < \epsilon < 1$. The emissivity is defined as the ratio of the energy emitted by the grey body to the energy emitted if it were black at the same temperature. The heat flux emitted by a grey body is then given by

$$\dot{q}_g^e = \sigma \epsilon T^4, \tag{2.9}$$

and the rate of emission, in units of power, is given by

$$\dot{Q}_g^e = \sigma \epsilon A T^4. \tag{2.10}$$

The rate of heat transfer between two grey surfaces is most easily expressed in terms of *transfer factors*, which are analogous to the view factors defined for black surfaces. However, the transfer factor, which will be denoted by $\mathscr{F}_{i \to j}$, includes radiation emitted by surface i which reflects off of intermediate surfaces before reaching j. (Recall that the view factor only considers radiation which travels *directly* from surface i to surface j.) Whereas the view factors depend solely on the geometry of the surface involved, the transfer factors also depend on the emissivities of the two surfaces. Once the view factors have been determined, the transfer factors can be computed with

the following procedure. First, a set of intermediate parameters, known as the $\hat{F}$ parameters is computed via following system of equations [48]

$$\hat{F}_{i-j} = F_{i-j} + \sum_{k=1}^{N}(1-\epsilon_k)F_{i-k}\hat{F}_{k-j} \qquad \text{for} \quad i,j = 1,2,...,N. \tag{2.11}$$

Although it may seem that Eq. 2.11 is a system of N^2 equations with N^2 unknowns, it can instead be solved as N independent sets of equations, each with N unknowns, which is easier to implement and faster to solve [48]. Once the $\hat{F}$ parameters have been computed, the transfer factors can be computed by

$$\mathscr{F}_{i-j} = \epsilon_i \epsilon_j \hat{F}_{i-j}. \tag{2.12}$$

Then, the net rate of heat transfer from a grey surface i to a second grey surface j (analogous to Eq. 2.7) is given by

$$\dot{Q}_{i\to j}^{net,g} = \sigma A_i \mathscr{F}_{i\to j}(T_i^4 - T_j^4). \tag{2.13}$$

Likewise, for a problem involving N isothermal grey surfaces, the net radiation from surface i to the other surfaces is given by

$$\dot{Q}_{i}^{net,g} = \sum_{j=1}^{N} \sigma A_i \mathscr{F}_{i\to j}(T_i^4 - T_j^4). \tag{2.14}$$

As before, Eq. 2.14 represents a system of $2N$ equations for N unknowns; the remaining N equations needed to define the system come from boundary conditions.

2.2 Shape Memory Alloys

Shape memory alloys (SMAs) are a class of smart material with the ability to change shape in response to variations in temperature and/or stress [34, 50]. This behavior

is due to a diffusionless phase transformation between two solid phases known as *martensite*, which is the low temperature phase, and *austenite*, which is the high temperature phase. In the martensite phase, shape memory alloy material is capable of undergoing large deformation without permanent damage. Upon heating into the austenite phase, the deformation is recovered, even in the presence of applied stresses. This behavior can be used to create solid-state actuators which are capable of generating up to approximately 7% actuation strain at stresses on the order of 500 MPa. One of the most well-known examples of this principle is Boeing's Variable Geometry Chevron (VGC), which used shape memory alloys to actuate the chevrons at the back of an engine nacelle [6, 5, 40]. During takeoff, the chevrons were canted slightly into the bypass air to reduce engine noise. During cruise, when the ambient temperature is significantly lower, the SMA-based chevrons retracted automatically into a low-drag configuration. As the aircraft descended to warmer conditions for landing, the chevrons returned to their low-noise position. Other aerospace applications for shape memory alloys include torque tubes for actuating aircraft control surfaces [24, 26, 59], stepper motors for solar flaps [19], active hinges for deploying solar arrays on spacecraft [7, 69], and an SMA arm as part of an experiment onboard the Mars Pathfinder [19].

Shape memory alloys are ideally suited for use in morphing radiators. SMAs have the highest actuation energy density among smart materials [34]. Additionally, due to the inherent temperature dependence of the SMA, there is no need for external power, instrumentation, or control systems in order to achieve the desired heat rejection variability. Finally, there is already a variety of shape memory material with transformation temperatures in the ranges needed by a morphing radiator.

There are a number of models that seek to describe the nonlinear and hysteretic constitutive behavior of shape memory alloys [37, 52, 54]. The model used herein is

based on the phenomenological model of Lagoudas et al. [35] with modifications to the hardening functions to allow partial cycles to be represented more accurately. Using the approach taken by Lagoudas et al. [4, 34, 36], we begin by choosing an appropriate set of independent state variables. Since the martensitic phase transformation is driven by changes in stress and temperature, it is natural to select the Cauchy stress tensor $\boldsymbol{\sigma}$ and absolute temperature T as the external state variables. Additionally, three internal state variables are chosen: the transformation strain tensor $\boldsymbol{\varepsilon}^t$, martensitic volume fraction ξ, and transformation hardening energy g^t. The Gibbs free energy G for the overall SMA is then defined as a function of the independent state variables by

$$G(\boldsymbol{\sigma}, T, \boldsymbol{\varepsilon}^t, \xi, g^t) = (1-\xi)G^A(\boldsymbol{\sigma}, T) + \xi G^M(\boldsymbol{\sigma}, T) + G^{mix}(\boldsymbol{\sigma}, \boldsymbol{\varepsilon}^t, g^t). \tag{2.15}$$

In this expression, G^A and G^M represent the thermoelastic contributions to the Gibbs free energy from the austenite and martensite phases, respectively. Assuming a quadratic stress dependence, G^A and G^M are given by

$$G^A = -\frac{1}{2\rho}\boldsymbol{\sigma} : \boldsymbol{S}^A\boldsymbol{\sigma} - \frac{1}{\rho}\boldsymbol{\sigma} : \boldsymbol{\alpha}^A(T - T_0) + c\left[(T - T_0) - T\ln\left(\frac{T}{T_0}\right)\right] - s_0^A T + u_0^A, \tag{2.16a}$$

$$G^M = -\frac{1}{2\rho}\boldsymbol{\sigma} : \boldsymbol{S}^M\boldsymbol{\sigma} - \frac{1}{\rho}\boldsymbol{\sigma} : \boldsymbol{\alpha}^M(T - T_0) + c\left[(T - T_0) - T\ln\left(\frac{T}{T_0}\right)\right] - s_0^M T + u_0^M, \tag{2.16b}$$

and the mixing term, which represents the interaction between martensite and austenite, is given by

$$G^{mix}(\boldsymbol{\sigma}, \boldsymbol{\varepsilon}^t, g^t) = -\frac{1}{\rho}\boldsymbol{\sigma} : \boldsymbol{\varepsilon}^t + \frac{1}{\rho}g^t. \tag{2.17}$$

The parameters $\boldsymbol{S}$, s_0, and u_0 represent the compliance tensor, specific reference entropy, and specific reference internal energy, respectively. Each of these parameters is assumed to be different for the two phases (i.e., $\boldsymbol{S}^A \neq \boldsymbol{S}^M$, etc. in general). The parameters ρ, c, and $\boldsymbol{\alpha}$ represent the mass density, specific heat, and thermal expansion tensor, respectively; these parameters are assumed to be constant regardless of phase. Note that the phase-dependent parameters are assumed to follow the rule of mixtures in terms of the martensitic volume fraction ξ. For example, the compliance tensor $\boldsymbol{S}(\xi)$ is defined as

$$\boldsymbol{S}(\xi) = (1-\xi)\boldsymbol{S}^A + \xi\boldsymbol{S}^M. \tag{2.18}$$

Applying the Coleman-Noll Procedure [9, 10, 11, 41] to Eq. 2.15 provides the following expressions for the total strain $\boldsymbol{\varepsilon}$ and entropy s:

$$\boldsymbol{\varepsilon} = -\rho\frac{\partial G}{\partial \boldsymbol{\sigma}} = \boldsymbol{S}(\xi)\boldsymbol{\sigma} + \boldsymbol{\alpha}(\xi)(T - T_0) + \boldsymbol{\varepsilon}^t, \tag{2.19}$$

$$s = -\frac{\partial G}{\partial T} = \frac{1}{\rho}\boldsymbol{\sigma} : \boldsymbol{\alpha}(\xi) + c\ln\left(\frac{T}{T_0}\right) + s_0(\xi). \tag{2.20}$$

The equations governing the evolution of the transformation strain are given by

$$\dot{\boldsymbol{\varepsilon}}^t = \dot{\xi}\boldsymbol{\Lambda}^t, \tag{2.21a}$$

$$\boldsymbol{\Lambda}^t = \begin{cases} \dfrac{3}{2}H^{cur}(\bar{\sigma})\dfrac{\boldsymbol{\sigma}'}{\bar{\sigma}} & \text{if} \quad \dot{\xi} > 0 \\ \dfrac{\boldsymbol{\varepsilon}^{t-r}}{\xi^r} & \text{if} \quad \dot{\xi} < 0 \end{cases}, \tag{2.21b}$$

$$\boldsymbol{\sigma}' = \boldsymbol{\sigma} - \frac{1}{3}\text{tr}(\boldsymbol{\sigma})\mathbf{I}, \tag{2.21c}$$

$$\bar{\sigma} = \sqrt{\frac{3}{2}\boldsymbol{\sigma}' : \boldsymbol{\sigma}'}, \tag{2.21d}$$

$$H^{cur}(\bar{\sigma}) = \begin{cases} H_{min} & \text{if} \quad \bar{\sigma} \leq \bar{\sigma}_{crit} \\ H_{min} + (H_{max} - H_{min})(1 - e^{-k(\bar{\sigma} - \bar{\sigma}_{crit})}) & \text{if} \quad \bar{\sigma} > \bar{\sigma}_{crit} \end{cases}, \tag{2.21e}$$

where $\boldsymbol{\Lambda}^t$ is the *transformation direction tensor*, $\boldsymbol{\sigma}'$ is the deviatoric part of the stress tensor, $\bar{\sigma}$ is the Mises equivalent stress, and $\boldsymbol{\varepsilon}^{t-r}$ and ξ^r are the transformation strain tensor and martensitic volume fraction at transformation reversal, respectively. H_{min}, H_{max}, k, and $\bar{\sigma}_{crit}$ are experimentally-determined parameters governing the transformation strain magnitude for full transformation. Likewise, the evolution of the hardening energy is given by

$$\dot{g}^t = f^t\dot{\xi}, \tag{2.22a}$$

$$f^t = \begin{cases} \dfrac{1}{2}a_1\left(1 + \hat{\xi}_{fwd}(\xi)^{n_1} - (1 - \hat{\xi}_{fwd}(\xi))^{n_2}\right) + a_3 & \text{if} \quad \dot{\xi} > 0 \\ \dfrac{1}{2}a_2\left(1 + \hat{\xi}_{rev}(\xi)^{n_3} - (1 - \hat{\xi}_{rev}(\xi))^{n_4}\right) - a_3 & \text{if} \quad \dot{\xi} < 0 \end{cases}, \tag{2.22b}$$

$$\hat{\xi}_{fwd}(\xi) = \frac{1}{1 - \xi^f}\xi - \frac{\xi^f}{1 - \xi^f}, \tag{2.22c}$$

$$\hat{\xi}_{rev}(\xi) = \frac{1}{\xi^r}\xi, \tag{2.22d}$$

where f^t is the hardening function and ξ^f and ξ^r are the martensitic volume fraction at the end of reverse and forward transformation, respectively. The parameters n_1, n_2, n_3, and n_4 are determined experimentally. The transformation criterion is formulated in terms of a transformation function Φ^t defined by

$$\Phi^t = \begin{cases} \Pi - Y^t & \text{if} \quad \dot{\xi} > 0 \\ -\Pi - Y^t & \text{if} \quad \dot{\xi} < 0 \end{cases} \tag{2.23}$$

and constrained by

$$\Phi^t \leq 0, \qquad \dot{\xi}\Phi^t = 0, \qquad 0 \leq \xi \leq 1. \tag{2.24}$$

In Eq. 2.23, Π is the thermodynamic driving force, defined by

$$\Pi(\boldsymbol{\sigma}, T, \xi) = \boldsymbol{\sigma} : \boldsymbol{\Lambda}^t + \frac{1}{2}\boldsymbol{\sigma} : \Delta\boldsymbol{S}\boldsymbol{\sigma} + \boldsymbol{\sigma} : \Delta\boldsymbol{\alpha}(T - T_0) + \rho\Delta s_0 T - \rho\Delta u_0 - f^t, \tag{2.25}$$

where the Δ operator denotes the difference in a material parameter (i.e., $\Delta\boldsymbol{S} = \boldsymbol{S}^M - \boldsymbol{S}^A$, etc.) and Y^t is assumed to be a linear function of stress given by

$$Y^t = Y_0^t + D\boldsymbol{\sigma} : \boldsymbol{\Lambda}^t. \tag{2.26}$$

In Eqs. 2.22, 2.23, 2.25, and 2.26, $\rho\Delta s_0$, $\rho\Delta u_0$, a_1, a_2, a_3, Y_0^t, and D are model parameters which may be expressed in terms of the phase diagram parameters (M_s, M_f, A_s, A_f, C^A, and C^M) and the transformation strain parameters (H_{min}, H_{max}, k,

and $\bar{\sigma}_{crit}$) [35]:

$$\rho\Delta s_0 = \left.\frac{-2\left(C^M C^A\right)\left[H^{cur}(\sigma)+\sigma\frac{\partial H^{cur}}{\partial\sigma}(\sigma)+\sigma\left(\frac{1}{E^M}-\frac{1}{E^A}\right)\right]}{C^M+C^A}\right|_{\sigma=\sigma^*}, \tag{2.27a}$$

$$D = \left.\frac{\left(C^M - C^A\right)\left[H^{cur}(\sigma)+\sigma\frac{\partial H^{cur}}{\partial\sigma}(\sigma)+\sigma\left(\frac{1}{E^M}-\frac{1}{E^A}\right)\right]}{\left(C^M+C^A\right)\left[H^{cur}(\sigma)+\sigma\frac{\partial H^{cur}}{\partial\sigma}(\sigma)\right]}\right|_{\sigma=\sigma^*}, \tag{2.27b}$$

$$a_1 = \rho\Delta s_0(M_f - M_s), \tag{2.27c}$$

$$a_2 = \rho\Delta s_0(A_s - A_f), \tag{2.27d}$$

$$a_3 = \frac{\rho\Delta s_0}{2}(M_s + A_f), \tag{2.27e}$$

$$Y_0^t = \frac{\rho\Delta s_0}{2}(M_s - A_f) - a_3. \tag{2.27f}$$

2.3 Thermomechanical Coupling

Problems in which the independent field variables of interest influence each other are said to be *coupled*. *Thermomechanical coupling* is the particular type of coupling that arises when the temperature field in a body depends on the displacement field and vice versa. The primary goal of a thermomechanically coupled analysis is to predict the evolution of these two fields, which may be functions of both time and space. This section presents the equations which govern a thermomechanically-coupled problem. In the following discussion, the temperature field will be denoted by $T = \hat{T}(\mathbf{x}, t)$ and the displacement field will be denoted by $\mathbf{u} = \hat{\mathbf{u}}(\mathbf{x}, t)$, where $\mathbf{x}$ represents a point in the deformed configuration [20, 38]. The evolution of the temperature field in an anisotropic material is governed by the balance of energy, the local form of which is given by [34, 51, 58]

$$\rho c\dot{T} = -\mathrm{div}(\mathbf{q}) + \boldsymbol{\sigma} : \dot{\boldsymbol{\varepsilon}} + \rho r. \tag{2.28}$$

In this equation, ρ and c denote the mass density and specific heat capacity, respectively, $\dot{T} \equiv \partial T/\partial t$ denotes the partial derivative of the temperature with respect to time, $\mathbf{q}$ is the heat flux, $\boldsymbol{\sigma}$ is the Cauchy stress tensor, $\dot{\boldsymbol{\varepsilon}}$ is the strain rate, and r represents an internal heat source per unit mass. The relationship between temperature and heat flux for a general material is given by

$$\mathbf{q} = -\mathbf{k}\,\mathrm{grad}\,(T) \tag{2.29}$$

where $\mathbf{k}$ is the second-order thermal conductivity tensor [51] which acts on the gradient of temperature. The local form of the balance of linear momentum is given by [38]

$$\rho\ddot{\mathbf{u}} = \mathrm{div}(\boldsymbol{\sigma}) + \mathbf{b}, \tag{2.30}$$

where $\ddot{\mathbf{u}} \equiv \partial^2\mathbf{u}/\partial t^2$ is the material acceleration and $\mathbf{b}$ is the body force vector per unit volume.

The constitutive equation relating stress and strain in a typical linearly elastic material is given by

$$\boldsymbol{\sigma} = \boldsymbol{C}\left[\boldsymbol{\varepsilon} - \boldsymbol{\alpha}(T - T_0)\right] \tag{2.31}$$

where $\boldsymbol{C}$ is a fourth-order tensor known as the *elasticity tensor* and $\boldsymbol{\varepsilon}$ is the linearized strain tensor, given by

$$\boldsymbol{\varepsilon} = \frac{1}{2}\left[\nabla\mathbf{u} + (\nabla\mathbf{u})^{\mathsf{T}}\right]. \tag{2.32}$$

For a shape memory alloy, the constitutive equation is given by

$$\boldsymbol{\sigma} = \boldsymbol{C}(\xi)\left[\boldsymbol{\varepsilon} - \boldsymbol{\varepsilon}^t - \boldsymbol{\alpha}(T - T_0)\right], \tag{2.33}$$

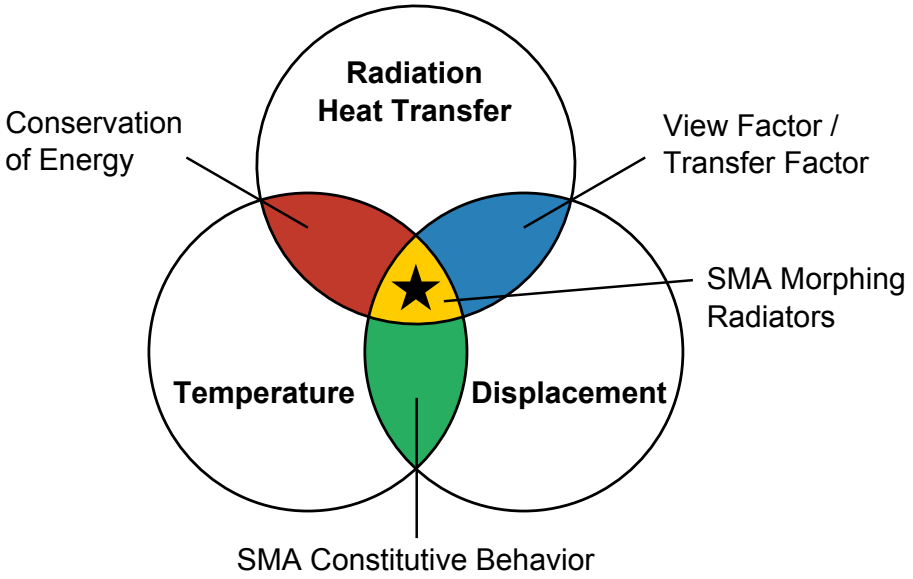

Figure 2.2: Diagram showing the phenomena and their relationships in a general problem involving shape memory alloys and radiation boundary conditions.

where $\boldsymbol{\varepsilon}^t$ denotes the transformation strain which depends on stress and temperature, as described in Section 2.2.

Figure 2.2 gives a schematic representation of the phenomena and their relationships for a general problem involving shape memory alloys and radiation boundary conditions. The circles represent the phenomena and the colored overlapping regions represent relationships between the phenomena. For example, temperature and heat flux are related via the balance of energy (Eq. 2.28), heat flux and displacement are related via the geometry-dependent view factors (Eq. 2.8) or transfer factors (Eq. 2.14), and the shape memory alloy constitutive behavior relates changes in temperature to changes in displacement (See Sec. 2.2 above). Modeling the behavior of morphing radiators requires consideration of all three of these phenomena, shown with the star in the center of the figure. The physics of this class of problem have not been widely considered in the literature. Ramesh, Balaji, and Venkateshan considered

the effects of cavity radiation on radiating fins, but the geometry remained fixed throughout the problem [56]. Naumann likewise conducted optimization of a radiator with fixed geometry [47]. Juhasz and Peterson present a number of innovative radiator designs, including variable surface area radiators with roll-out fins, however none of these designs involve shape memory alloys and therefore do not exhibit the same type of thermomechanical coupling [33].

Existing codes such as Ansys, Abaqus, NASTRAN, and others are capable of analyzing many coupled temperature-displacement problems, such as those involving heat conduction and convection [12, 44, 62]. However, the addition of radiation boundary conditions increases the complexity of the problem, as any changes in geometry require view factors to be recalculated. As described in Sec. 2.1, computation of view factors for general geometry is an expensive operation which requires a number of calculations proportional to the square of the number of interacting surfaces [67]. Since traditional radiators have fixed geometry, there has been little need to include support for such computationally-expensive boundary conditions within a coupled temperature-displacement analysis; therefore, most simulation codes only allow radiation boundary conditions to be included in a pure thermal analysis. The result is that problems involving radiation and deformation are difficult or impossible to model natively in many existing commercial analysis tools. There are also external code interfaces which enable existing analysis tools to simulate coupled problems. One of these, MpCCI [32], was explored for this work. Although MpCCI is able to exchange temperature data, it is unable to send the displacement field (i.e., geometry) to the thermal analysis; therefore, it cannot be used to model the behavior of morphing radiators. One of the primary goals of this work is to develop a means by which general problems of this type may be analyzed. The following chapter will discuss one such approach.

3. ANALYSIS APPROACH, FRAMEWORK IMPLEMENTATION, AND EXAMPLE PROBLEMS[1]

Owing to the two-way coupling between the temperature and displacement fields, shape memory alloy morphing radiators are challenging to model in most existing simulation tools. This chapter describes an analysis approach which can be used to simulate general problems involving morphing radiators. The details of the approach itself and subsequent implementation are now discussed.

3.1 Analysis Approach

Henceforth, it will be assumed that the structural response is quasi-static, i.e., at every instant in time, the material is assumed to be in equilibrium. Additionally, it is assumed that there is no body force. With these assumptions, the structural equation reduces to

$$\mathbf{0} = \mathrm{div}(\boldsymbol{\sigma}) \tag{3.1}$$

and the conservation of energy reduces to

$$\rho c_p \dot{T} = -\mathrm{div}(\mathbf{q}). \tag{3.2}$$

Note that, as a result of the quasi-static assumption, Eq. 3.1 does not depend explicitly on time.

Physically, the fields of interest are continuous functions in both space and time. However, as a result of the nonlinear and hysteretic behavior of the shape memory alloy (See Sec. 2.2) and the complicated nature of radiation boundary conditions (See

[1]Portions of this material reprinted from the Proceedings of the Active and Passive Smart Structures and Integrated Systems Conference (2015), DOI 10.1117/12.2175739 [2], by permission of SPIE.

Sec. 2.1), it is difficult or impossible to derive an analytical solution to the system of equations defined by Eqs. 3.1 and 3.2 for general problems involving morphing radiators. Therefore, the remainder of this work will be concerned with developing approximate solutions to this system. The first step in developing an approximate solution to the governing partial differential equations is to discretize the temperature and displacement fields in space [57]:

$$T = \hat{T}(\mathbf{x}, t) = \sum_{i=1}^{N} T_i(t)\psi_i(\mathbf{x}) \quad , \tag{3.3a}$$

$$\mathbf{u} = \hat{\mathbf{u}}(\mathbf{x}, t) = \sum_{i=1}^{N} \mathbf{u}_i(t)\psi_i(\mathbf{x}) \quad . \tag{3.3b}$$

The set of functions denoted by $\psi_i(\mathbf{x})$ is known as the set of *interpolation functions*[2] [57]. The spatial approximations in Eqs. 3.3a and 3.3b lead to a set of ordinary differential equations for the nodal variables $T_i(t)$ and $\mathbf{u}_i(t)$. The fields may also be discretized in time [57]:

$$T = \hat{T}(\mathbf{x}, t_s) = \sum_{i=1}^{N} T_i(t_s)\psi_i(\mathbf{x}), \quad s = 0, 1, ... \quad , \tag{3.4a}$$

$$\mathbf{u} = \hat{\mathbf{u}}(\mathbf{x}, t_s) = \sum_{i=1}^{N} \mathbf{u}_i(t_s)\psi_i(\mathbf{x}), \quad s = 0, 1, ... \quad . \tag{3.4b}$$

The further approximations in Eqs. 3.4a and 3.4b allow the set of ordinary differential equations to be converted into a set of algebraic equations. For a thermomechanically

[2]It is possible to use interpolation functions which depend on both time and space, however, in this work, it is assumed that the interpolation functions depend on space only.

coupled problem, the system may be expressed as

$$\begin{bmatrix} K_{\theta\theta}(T,\mathbf{u}) & K_{\theta u}(T,\mathbf{u}) \\ K_{u\theta}(T,\mathbf{u}) & K_{uu}(T,\mathbf{u}) \end{bmatrix} \begin{Bmatrix} T \\ \mathbf{u} \end{Bmatrix} = \begin{Bmatrix} q(T,\mathbf{u}) \\ f(T,\mathbf{u}) \end{Bmatrix}. \tag{3.5}$$

In the preceding system, the K_{ij} terms represent the coefficient sub-matrices while q and f represent generalized structural and thermal loads. In general, each of the terms in this equation may be a function of the independent variables. For example, the SMA constitutive behavior, which depends on both temperature and stress (i.e. displacement) is represented in the K_{uu} and $K_{u\theta}$ terms. Thus, Eq. 3.5 is a nonlinear, inhomogeneous system of algebraic equations subject to a set of initial conditions of the form

$$\begin{Bmatrix} T(0) \\ \mathbf{u}(0) \end{Bmatrix} = \begin{Bmatrix} T^{(0)} \\ \mathbf{u}^{(0)} \end{Bmatrix}. \tag{3.6}$$

For problems involving most common types of boundary conditions, the system in Eq. 3.5 may be solved readily using a numerical technique such as Newton's method. However, the introduction of geometry-dependent radiation boundary conditions in the thermal equation complicates the solution procedure, as this type of boundary condition depends strongly on both the displacement and temperature. Recall the expression for the net rate of heat transfer from a grey surface i to the other surfaces in the problem, given by

$$\dot{Q}_i^{net,g} = \sum_{j=1}^{N} \sigma A_i \mathscr{F}_{i\to j}(T_i^4 - T_j^4), \tag{3.7}$$

where σ is the Stefan-Boltzmann constant, A_i is area of surface i, and $\mathscr{F}_{i\to j}$ is the transfer factor from surface i to surface j, which is a non-dimensional parameter defined as the fraction of radiation emitted by the surface i that strikes surface j.

As described in Chapter 2, these factors are highly dependent on geometry, which presents an additional challenge when including boundary conditions of this form in a thermomechanically coupled problem. Furthermore, determination of the transfer factors is a very computationally-expensive process for arbitrary geometry, requiring a number of calculations proportional to the square of the number of interacting surfaces [67]. For non-coupled thermal problems in which the geometry remains fixed for all time, these factors need only be computed once at the beginning of the analysis; however, in a coupled analysis, they must be recomputed for every incremental change in displacement. Since traditional radiators have fixed geometry, there has been little need to include support for radiation boundary conditions of the form in Eq. 3.7 in a coupled thermomechanical analysis procedure; therefore, most existing analysis tools only allow radiation boundary conditions to be included in a pure thermal analysis. The result is that coupled problems involving radiation boundary conditions are difficult or impossible to model natively in most existing commercial analysis tools.

This shortcoming may be addressed by moving to a technique known as *partitioned analysis procedure*, in which a fully-coupled set of field equations is decoupled into two or more smaller systems known as *partitions* that are solved independently of each other [15, 53]. The partitions are executed incrementally in an alternating series and exchange data as the solution progresses in order to represent the effect of the coupling. This approach is frequently employed in fluid-structure interaction (FSI) problems [13, 28, 70]. For a thermomechanically coupled problem, the system in Eq. 3.5 is separated into *thermal* and *structural* partitions. The thermal partition may be written as

$$\begin{bmatrix} K_{\theta\theta}(T, \bar{\mathbf{u}}) & K_{\theta u}(T, \bar{\mathbf{u}}) \end{bmatrix} \begin{Bmatrix} T \\ \bar{\mathbf{u}} \end{Bmatrix} = q(T, \bar{\mathbf{u}}). \tag{3.8}$$

In this expression, the overbar $(\bar{\cdot})$ is used to indicate that the displacement field is fixed and specified in the thermal partition. Therefore, temperature field is the only unknown in this equation. Likewise, the structural partition may be written as

$$\left[K_{u\theta}(\bar{T},\mathbf{u}) \quad K_{uu}(\bar{T},\mathbf{u})\right] \begin{Bmatrix} \bar{T} \\ \mathbf{u} \end{Bmatrix} = f(\bar{T},\mathbf{u}), \tag{3.9}$$

where the displacement field is unknown and the temperature field is fixed and specified. Note that the constitutive behavior of the shape memory alloy is represented in the coefficient matrices K_{uu} and $K_{u\theta}$.

The primary advantage to this approach is that each partition need only solve for a single unknown field; the thermal partition is responsible for solving for the temperature field, while the structural partition is responsible for solving for the displacement field. Since the displacement field (i.e., geometry) remains fixed in the thermal partition, radiation boundary conditions of the form in Eq. 3.7 are straightforward to include in the thermal partition. Equations 3.8 and 3.9 can be rearranged to define operators for the solution process of the thermal and structural partitions, which will be denoted by

$$\begin{aligned} \mathbf{u} &= \mathbf{S}(\mathbf{u},\bar{T}) \equiv {K_{uu}}^{-1}\left(f(\mathbf{u},\bar{T}) - K_{u\theta}\bar{T}\right) \\ T &= \mathbf{T}(\bar{\mathbf{u}},T) \equiv {K_{\theta\theta}}^{-1}\left(q(\bar{\mathbf{u}},T) - K_{\theta u}\bar{\mathbf{u}}\right). \end{aligned} \tag{3.10}$$

Note that the above expressions are written in an implicit form, with the independent field variables appearing on both sides of their respective equations. Now that the partitions have been defined, a particular execution method must be chosen. There are a number of methods available, each with its own advantages and disadvantages. The simplest method, known as the *sequential staggered procedure*, uses a time-explicit

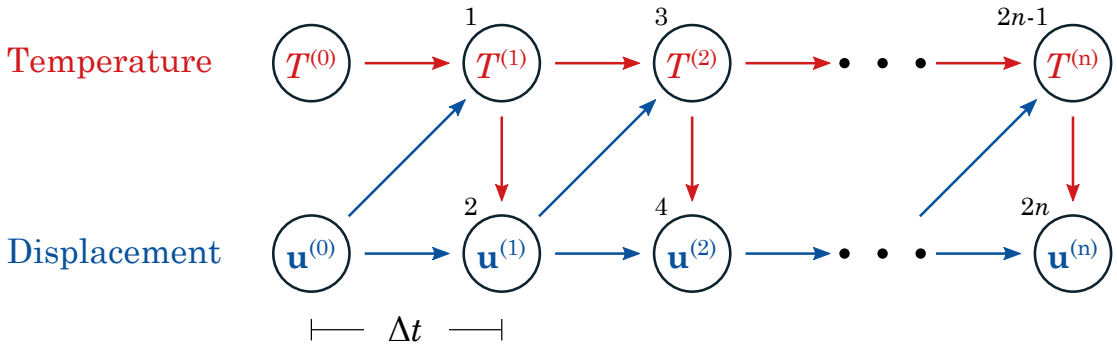

Figure 3.1: Flowchart for the staggered solution procedure used to simulate the thermomechanically coupled behavior of SMA-based morphing radiators. Partitions are executed in an alternating series.

integration scheme which executes the partitions in an incremental, alternating fashion and exchanges data between the partitions at each increment [15]. Figure 3.1 shows a graphical representation of the sequential staggered procedure. The time-discretized temperature and displacement fields are shown across the top and bottom of the figure, respectively, and superscripts are used to denote the state of the field at a particular instant in time (i.e., $T^{(n)} \equiv T(t_n)$). Arrows indicate the flow of data between the partitions and the simulation time increases from left to right.

The procedure begins with a set of known initial conditions, namely, an initial temperature field, denoted by $T(0) = T^{(0)}$ and an initial displacement field, denoted by $\mathbf{u}(0) = \mathbf{u}^{(0)}$. Since the shape memory alloy behavior is driven entirely by changes in temperature in the absence of externally-applied forces [34], the thermal partition is executed first. The thermal partition uses the initial conditions to advance the temperature field by one time increment, yielding $T^{(1)} = T(t_1)$. This temperature field is then passed to the structural partition, which solves for the displacement field $\mathbf{u}^{(1)} = \mathbf{u}(t_1)$ corresponding to $T^{(1)}$. At this point, both partitions have been executed

and the fields of interest have been evolved by one time increment. To begin the second increment, the geometry (i.e., displacement field) from the first increment, $\mathbf{u}^{(1)}$, is passed to the thermal partition, which advances the temperature field by an additional time increment, yielding $T^{(2)}$. The new temperature field is subsequently sent to the structural partition which updates the displacement field accordingly, yielding $\mathbf{u}^{(2)}$. This process simply repeats until the end of the simulation is reached after a desired number of time increments. Owing to its time-explicit integration approach, this method gives rise to a first-order time accurate solution method in time which requires sufficiently small timesteps to achieve accurate results; the nature of the problem dictates a suitable step time. More advanced methods are capable of achieving second-order time accuracy at the expense of additional complexity [13], however, this work has only considered the sequential staggered procedure described above.

3.2 Framework Implementation

Although the sequential approach described in the previous section could be implemented in a variety of analysis tools, Abaqus was used for this work. A number of features in Abaqus make it an ideal choice for implementing the framework [12]. In particular, Abaqus has support for both structural and thermal analysis procedures. Although there is no fundamental requirement that the thermal and structural partitions be implemented in the same tools, doing so generally simplifies implementation. In addition, Abaqus has the ability to include custom constitutive models via a User Material Subroutine (UMAT), which is essential to model the nonlinear and hysteretic behavior of shape memory alloys described previously. Finally, Abaqus provides a scripting interface in the Python programming language that enables every aspect of the analysis to be automated, including model creation, analysis execution,

and post-processing. This is an essential feature, as it would be prohibitively time consuming to implement the partitioned approach depicted above manually.

A custom framework was developed in Python to allow the partitions to be created and executed in an automated fashion; Figure 3.2 shows a diagram of the framework as implemented. The boxes represent individual analysis runs of the two partitions (Thermal and Structural), while arrows denote data transfer between the analyses. The order of execution is shown via the numbering in the upper-left corner of each box. Additionally, the simulation time at the end of each analysis is shown in parentheses following the partition name.

The framework begins with an initial step (marked *0* in Fig. 3.2), which defines the initial geometry and temperature field. No analysis takes place during this step; this is indicated with a dashed border in place of a solid border. The framework then begins the first increment with the thermal partition (*1*). The thermal analysis evolves the temperature field for one time increment considering the transient effects of radiation, conduction, and heat capacitance within the material. The global simulation time advances by the same time increment, from t_0 to t_1. Next, the structural partition is executed (*2*). The structural analysis determines the behavior of the shape memory alloy in response to the temperature field that was calculated in the first thermal analysis. This behavior is assumed to be quasi-static; consequently, the global simulation time does not advance at the completion of the structural analysis. Once the thermal and structural partitions have completed, the first increment is complete.

To begin the second increment, the framework creates a new instance of the thermal component (*3*). The newly-created thermal analysis uses the previous temperature field (from *1*) as an initial condition, along with the new geometry (from *2*) to advance the thermal solution by an additional time increment. The global simulation time also advances from t_1 to t_2. The new temperature field is passed

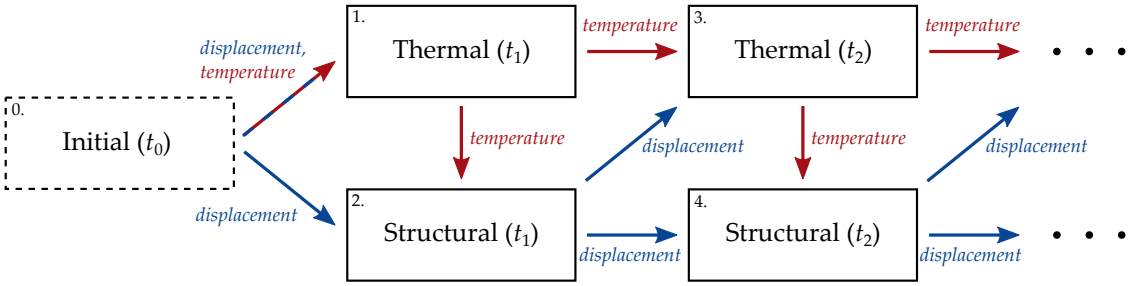

Figure 3.2: Implementation of the staggered solution procedure used by the analysis framework.

to the subsequent structural analysis and the framework continues executing the components in an alternating series until the total simulation time is reached.

In the limit that the time increment approaches zero, the framework will approach the fully-coupled behavior of the problem. Of course, practical limitations prevent taking arbitrarily small time steps. As the time step decreases, the total number of increments increases. There is a substantial overhead associated with creating a new analysis at each step, and this parasitic cost is proportional to the number of increments. Thus, as the time step decreases, the overhead becomes increasingly significant.

The remainder of this chapter presents a series of example problems which were used to demonstrate the application of the staggered solution procedure described above toward several problems involving morphing radiators.

3.3 Example Problem 1: Rigid Morphing Radiator

The first example problem considers a representative morphing radiator assembly consisting of three parts: a shape memory alloy torque tube [16, 39] and two identical thin, rigid, radiator panels. Figure 3.3 shows a schematic diagram of the radiator assembly used in the example problem. The radiator panels are $1.5\,\text{m} \times 1.5\,\text{m} \times 1\,\text{mm}$.

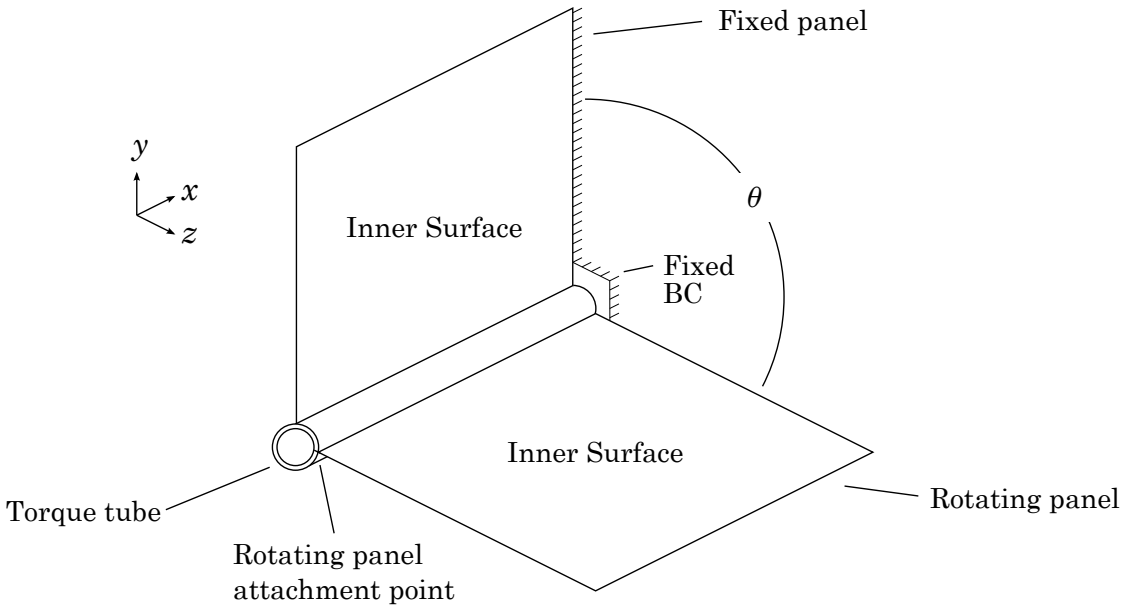

Figure 3.3: Diagram of the radiator assembly used in Example Problem 1.

The torque tube is 1.5 m in length with an outer diameter of 25 mm and an inner diameter of 24 mm. The vertical radiator panel remains fixed for all time and is not attached to the torque tube. The second radiator panel is attached to the otherwise unconstrained $-x$ face of the torque tube at a single point (indicated in Fig. 3.3). The angle between the two panels, denoted by θ, is equivalent to the thermally-induced actuation angle of the SMA torque tube. The $+x$ face of the torque tube is assigned a fixed boundary condition that constrains the face against displacement in the x direction as well as rotation in the yz plane. The torque tube is assumed to have been trained such that the free end rotates about the x-axis as the shape memory alloy undergoes strain recovery during the transformation from martensite to austenite [39]. This recovery of tube rotation during heating, known as the *shape memory effect* [34], causes the panel to rotate about the x-axis in unison with the free end of the torque tube.

The inner surface of each panel is able to radiate to the opposite panel as well as to the surroundings, while the outer surface of each panel is assumed to be insulated and, therefore, not capable of emitting radiation. Identical thermal properties (density, specific heat, and thermal conductivity) are assigned to each of the three parts. A uniform and constant heat load per unit volume is applied to the entire assembly. Both panels and the torque tube are assumed to be at the same uniform temperature throughout the simulations. Additionally, the effect of gravity is neglected. Note that these assumptions are not required for the computational analysis, but are included primarily to simplify the development of a mathematical model, which is described below.

The radiator is initially in the fully-closed configuration (i.e., $\theta(0) = 0$) with a uniform initial temperature of 50 K. This temperature is below M_s of the shape memory alloy; therefore, the torque tube begins in the martensite phase. In this state, the shape memory alloy is assumed to have a nonzero transformation strain as a result of previous training [39]. The two panels have no means of heat rejection in this configuration, since the two radiating surfaces are facing each other directly and the outward-facing sides are assumed to be insulated. As time progresses, the temperature in the assembly increases due to the applied heat load until the shape memory alloy begins to transform into austenite, resulting in the recovery of the transformation strain and rotation of the torque tube [34]. This causes the rotating panel to open away from the fixed panel ($\theta > 0$), allowing heat to be rejected to the surroundings. The shape memory alloy continues to transform until it has fully transformed into austenite ($T > A_f$). At this point, the angle between the panels has reached its maximum ($\theta = \theta_{max}$). Note that this particular example problem considers the behavior of the radiator exclusively under heating (reverse transformation). Table

Table 3.1: Material properties and other parameters used in the first example problem.

Parameter	**Value**
ϵ	0.85
c_p	329 J/kg·K
ρ	6450 kg/m^3
T_S	5 K
M_s	358 K
M_f	300 K
A_s	325 K
A_f	375 K
C^M	12.0 MPa/K
C^A	15.5 MPa/K
H_{max}	0.0286
β_τ	13.2 MPa
θ_{max}	135 deg
$\dot{q}$	1.0 MW/m^3

3.1 gives values of material properties and other parameters used in this problem. These properties correspond to the model of Hartl, et al [25].

A reduced-order model was developed for the first example problem for the purpose of direct verification. Assuming the temperature is identical in both radiator panels, there is no net heat exchange between them. This allows the model to simply consider one of the radiator panels. The energy balance for the panel is given by

$$mc_p\dot{T} = \dot{q}V - \sigma\epsilon A F_{P\to S}(\theta)(T^4 - T_S^4). \tag{3.11}$$

In the preceding equation, m, V, and $T(t)$ represent the mass, volume, and temperature, respectively, of the radiator assembly. The temperature of the surroundings, denoted by T_S, is assumed to remain constant. The angle between the two panels is denoted as θ, and $\dot{q}$ represents the constant uniform heat load per unit volume.

The function $F_{P\to S}(\theta)$ gives the view factor from the panel to the surroundings as a function of the angle between the two panels according to

$$F_{P\to S}(\theta) = 1 - F_{P\to P}(\theta), \tag{3.12}$$

where $F_{P\to P}$ is the view factor for two rectangles sharing a common edge and separated by an arbitrary angle θ. A general expression for this function may be found in several rescources [14, 21, 29]; due to its complexity, the expression will not be included here.

In Eqs. 3.11 and 3.12, θ itself is a function of temperature considering the behavior of the shape memory alloy torque tube. As mentioned above, this example focuses on the behavior of the torque tube as the shape memory alloy undergoes reverse transformation from martensite to austenite. A simplified constitutive model was derived for a torque tube from the three-dimensional shape memory alloy constitutive model of Lagoudas, et al. [35] and was modified to consider training of torque tubes via the introduction of an internal back stress [39, 25, 16]. The torque tube is assumed to be a prismatic cylinder under stress-free conditions such that

$$M = \frac{J\tau}{r} = 0, \tag{3.13}$$

where M is an externally-applied moment, J is the polar moment of area, τ is the shear stress, and r is the outer radius of the torque tube. For stress-free conditions, the shear strain in the tube is exclusively due to transformation. Thus, the twist angle of the tube, denoted by φ, can be written as[3]

$$\varphi = \theta = \frac{\gamma L}{r} = \frac{\gamma^t L}{r}, \tag{3.14}$$

[3]Since the rotating panel is attached to the end of the torque tube, the angle between the panels (θ) is identical to the twist angle of the torque tube.

where γ is the engineering shear strain, γ^t is the shear strain due to transformation, and L is the length of the torque tube. The evolution equation for the transformation strain during reverse transformation is

$$\dot{\gamma^t} = \dot{\xi}\Lambda_\gamma^t \qquad \Lambda_\gamma^t = \frac{\gamma^{t-r}}{\xi^r}, \tag{3.15}$$

where γ^{t-r} and ξ^r represent the transformation shear strain and martensitic volume fraction at transformation reversal, respectively. The torque tube is assumed to have been cooled to full martensite during manufacturing, thus $\xi^r = 1$. This implies that the initial value of γ^t, denoted γ_0^t, is identical to γ^{t-r} and that

$$\gamma^t = \xi\Lambda_\gamma^t. \tag{3.16}$$

Further, the transformation shear strain at transformation reversal is defined in terms of the conventional constitutive model parameters H_{max}, k, and β_t (see. Table 3.1), per

$$\gamma^{t-r} = \gamma_0^t = \sqrt{3}H_{max}\left[1 - e^{-k\sqrt{3}\beta_r}\right]. \tag{3.17}$$

Assuming stress-free conditions, the transformation function reduces to

$$\Phi_{rev}^t = -\rho\Delta s_0 T + \rho\Delta u_0 + \frac{1}{2}a_2\left[1 + \xi^{n_3} - (1-\xi)^{n_4}\right] + a_3 - Y_0^t = 0, \tag{3.18}$$

where $\rho\Delta s_0 T$, $\rho\Delta u_0$, a_2, a_3, n_3, n_4, and Y_0^t are model parameters that are calibrated from the stress-temperature phase diagram of the shape memory alloy [35].

Equations 3.11, 3.14, 3.16, and 3.18 define a system of equations in four unknown variables: θ, T, γ^t, and ξ. Due to the presence of an integral term in the view factor expression (see [14, 21, 29]) and the nonlinearity introduced by the shape

memory alloy constitutive model, a closed-form analytical solution does not exist for this system. Instead, the reduced-order model was implemented in MATLAB and Simulink. Simulink is a graphical modeling tool integrated with MATLAB that provides a number of numerical solvers. For this work, the `ode45` solver was used with a maximum step size of 0.5 s.

For the first example problem, the high-fidelity model was executed using the coupled framework with four different values for the time step: 100 s, 50 s, 20 s, and 10 s, corresponding to 10%, 5%, 2%, and 1% of the total simulation time. A maximum step size of 0.5 s was used for the reduced-order model. Three quantities were tracked throughout the simulations: the radiator temperature (which is assumed to be uniform), the angle between the panels, and the rate of heat rejection via radiation of a single panel. For each quantity, two figures are presented; the first figure shows the time history of the quantity, and the second figure plots the absolute error in the quantity with respect to the reduced-order model. Figures 3.4–3.6 present these plots.

Figure 3.4a shows the time history of the temperature in the radiator. The solution can be understood as having three distinct phases. During the first phase of the simulation, the temperature of the radiator increases as a result of the applied heat. Since the radiator is fully closed during this phase, the temperature increase is linear with time until the temperature reaches A_s, which occurs at $t = 160$ s. This marks the beginning of the second phase, during which the radiator panel opens away from the fixed panel, from 0 to 135 deg. The temperature increase continues to be approximately linear with time during the first portion of the second phase, but as the radiator opens, the slope of the temperature plot decreases. The panel continues to heat until the temperature reaches A_f, which occurs at $t = 460$ s. In the final phase, the shape memory alloy has finished transforming into austenite,

and the rotating panel has reached a steady-state configuration of 135 deg. The temperature approaches a steady-state value of approximately 385 K. Figure 3.4b shows the error in temperature and illustrates the strong dependency of the accuracy of the framework on choice of time step. The maximum transient error is 4.3 K occurring at $t = 300$ s when using a time step of 100 s. As the time step decreases, the maximum transient error decreases to 0.4 K when using a time step of 10 s. The magnitude of the steady-state error is less than 0.75 K for all simulations.

Figure 3.5a shows the time history of the angle between the radiator panels. The three phases are seen clearly on this plot. The first phase corresponds to $\theta = 0$ deg and ends at $t = 160$ s. During the second phase, the radiator opens from 0 deg to 135 deg. Note that the time history of the panel angle is nonlinear during this phase, which is a consequence of the nonlinearity in the temperature (see Eqs. 3.15 and 3.18). Figure 3.5a also clearly shows a time lag which is introduced by the framework due to the combination of an explicit coupled integration procedure and relatively large time steps. This time lag is the primary cause of the significant transient error shown in Fig. 3.5b.

The time lag in the geometry also affects the radiation heat transfer rate, which can be seen in Figures 3.6a and 3.6b. For small time steps, the framework tracks the reduced-order model closely. For larger time steps, the transient error increases significantly. In spite of this, the framework solutions all converge upon zero steady-state error.

In general, the suitability of one value of time step over another will depend on the nature of the problem. For this particular problem, the simulations all approach the same steady-state values for each of the quantities of interest. This is because the steady-state temperature is above the austenitic finish temperature (A_f) at which point the torque tube has a specific, known rotation. In this case, a large time step

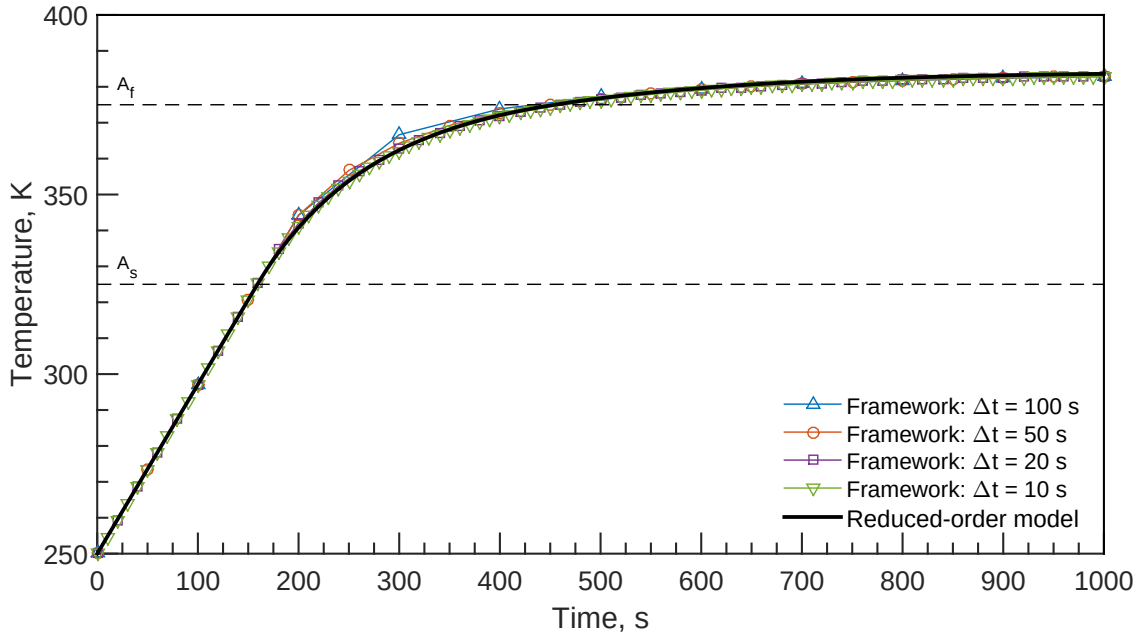

(a) Radiator temperature as computed via the analysis framework and reduced-order model. Horizontal dashed lines indicate transformation temperatures.

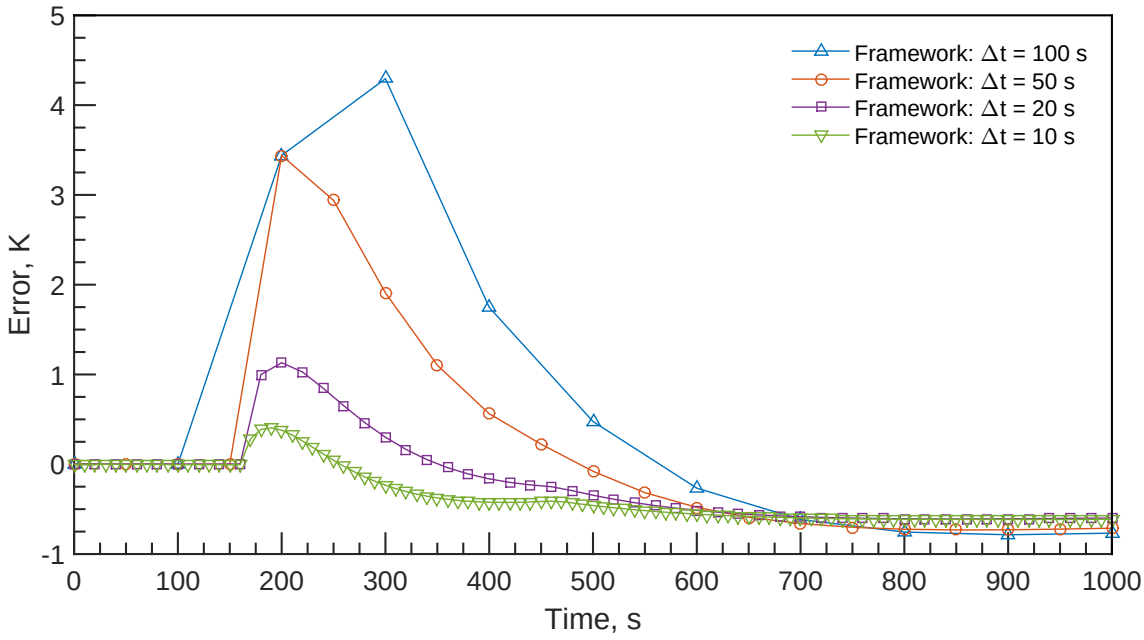

(b) Error in temperature with respect to the reduced-order model.

Figure 3.4: Comparison between the radiator temperature as predicted via the analysis framework and reduced-order model.

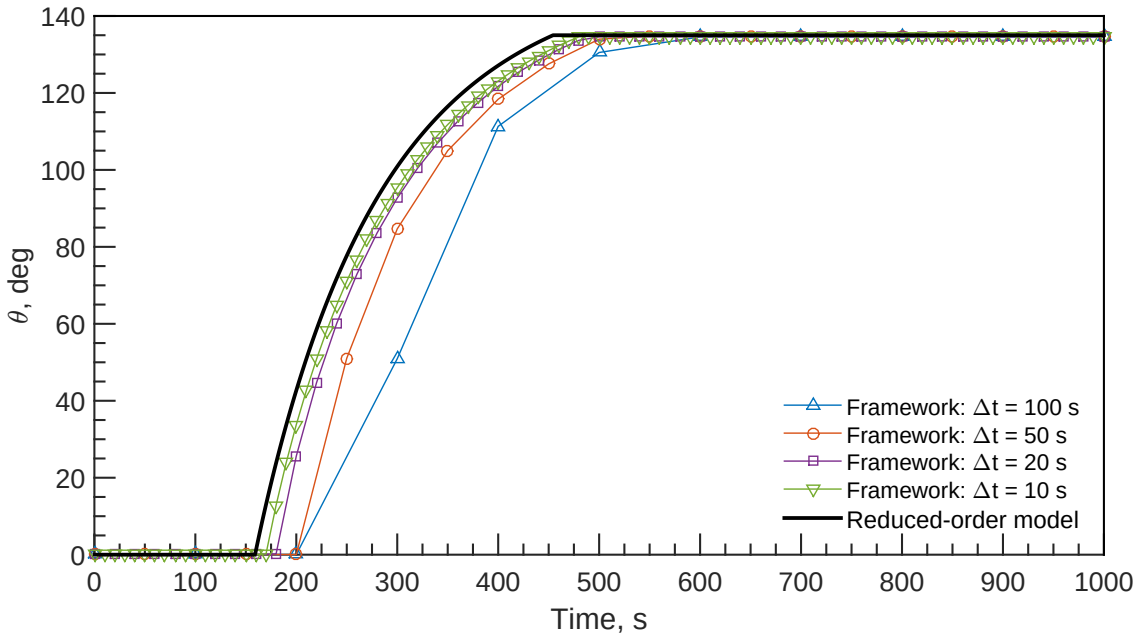

(a) Radiator panel angle as calculated via the analysis framework and reduced-order model.

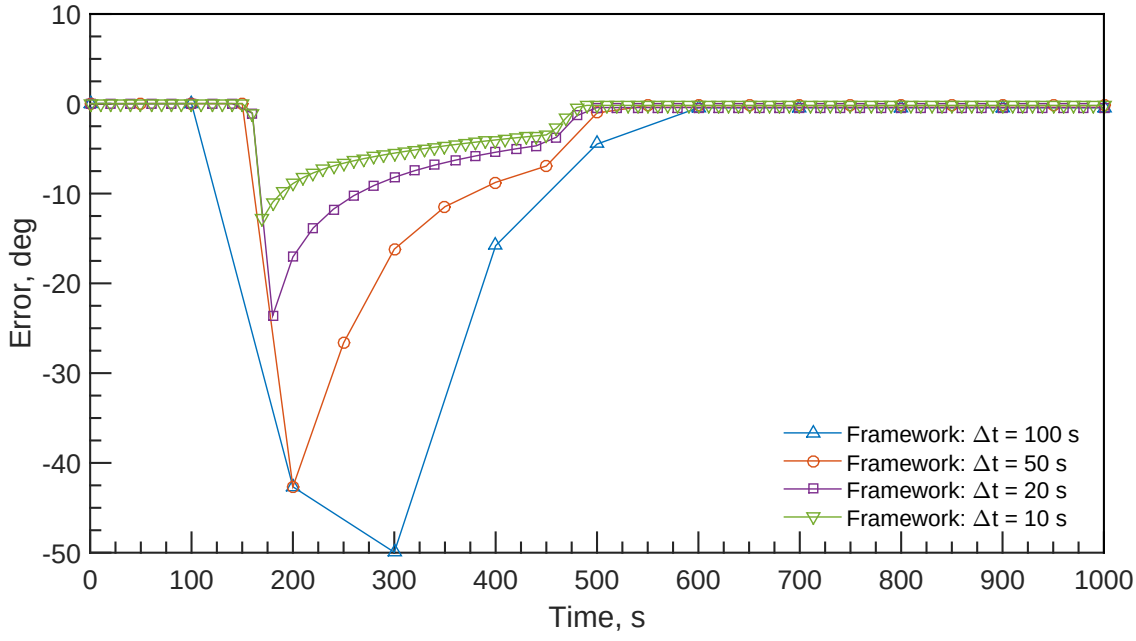

(b) Error in radiator panel angle with respect to the reduced-order model.

Figure 3.5: Comparison between the panel angle as predicted via the analysis framework and reduced-order model.

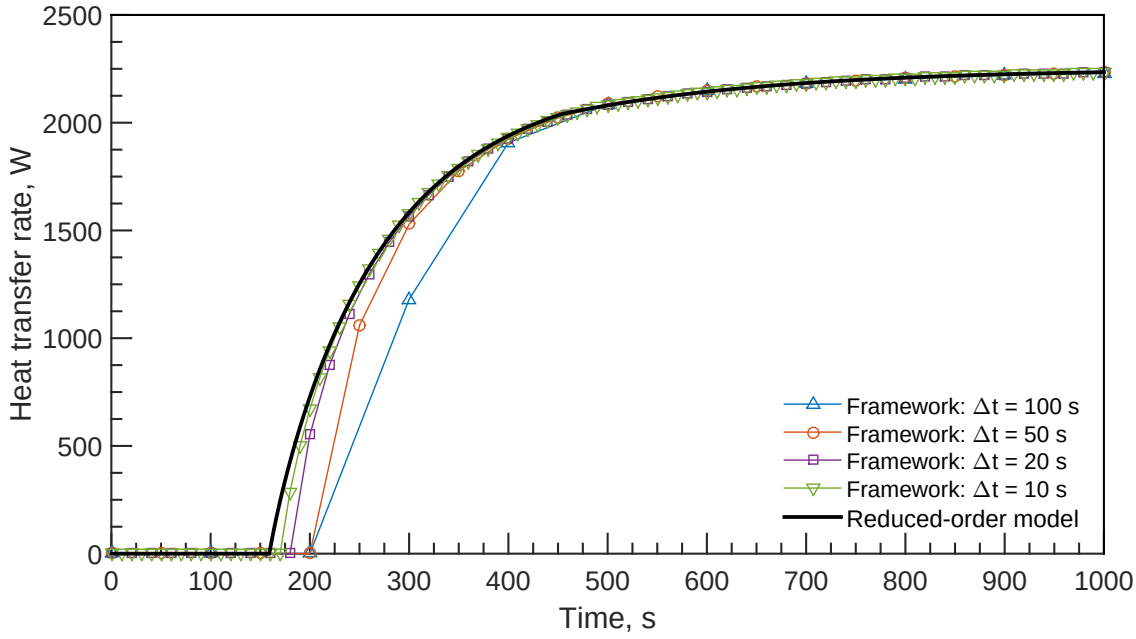

(a) Radiation heat transfer rate as calculated via the analysis framework and reduced-order model.

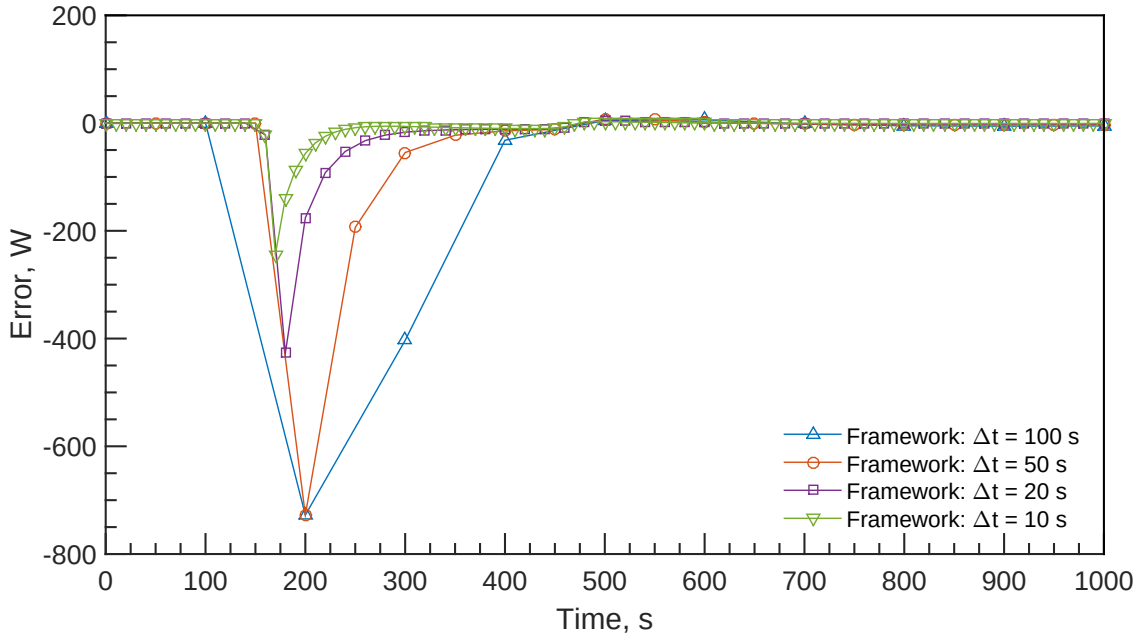

(b) Error in radiation heat transfer rate with respect to the reduced-order model.

Figure 3.6: Comparison between the heat transfer rate as predicted via the analysis framework and reduced-order model.

can be used to quickly obtain an understanding of the long term behavior of the radiator, perhaps during design studies. Once the design has been selected, a smaller time step can be used for the same geometry to obtain a more accurate understanding of the transient of the behavior of the radiator. Alternatively, the framework could be implemented using a variable time step instead of a fixed time step. This would allow the time step to be decreased automatically whenever significant geometry change is occurring. Likewise, when the geometry is no longer changing, the step size can be increased. The result is a decrease in the number of increments needed by the framework, and therefore, an increase in overall performance.

3.4 Example Problem 2: Flexible Morphing Radiator

The second example problem considers a flexible radiator panel (See Fig. 1.3), which begins in the circular configuration. The panel is 10 cm in length with an initial diameter of 7.75 cm. The total surface area of the panel is approximately 240 cm^2. The panel is composed of a five-ply composite layup consisting of three carbon plies between two glass fiber plies (see Table 3.2). Each ply has a thickness of 0.127 mm and a volume fraction of 60%. A 0.25 mm thick SMA film attached to the outer glass fiber ply provides the actuation force necessary to allow the panel to open under an increase in temperature. The material properties for the carbon and glass fiber plies are given in Table 3.3 and the properties for the shape memory alloy film are given in Table 3.4. The radiator is assumed to be fixed to the spacecraft along its line of symmetry, shown in red in Fig 3.7a.

The goal of the simulation is to predict the temperature and deformation responses to the transient heat load depicted in Fig. 3.8. The heat load consists of three heat cycles, each of which begins at 2 W, increases to 10 W, and then returns to 2 W. The load is applied uniformly to the base of the radiator along the line of symmetry

Table 3.2: Composite layup used in Example Problem 2. Ply 1 is the innermost ply and ply angles are defined with respect to the circumferential direction.

Ply	**Material**	**Angle**
1	S2 Glass	90°
2	K1100 Carbon	45°
3	K1100 Carbon	0°
4	K1100 Carbon	-45°
5	S2 Glass	90°
6	SMA	-

Table 3.3: Material properties for orthotropic K1100 carbon and S2 glass fiber plies. 2-direction is out of plane [8].

Material Property	**K1100 Carbon Fiber**	**S2 Glass Fiber**
ρ	$1812\,\mathrm{kg/m^3}$	$1969\,\mathrm{kg/m^3}$
c_p	$1000\,\mathrm{J/kg{\cdot}K}$	$1000\,\mathrm{J/kg{\cdot}K}$
$k_{11} = k_{33}$	$594\,\mathrm{W/m{\cdot}K}$	$0.861\,\mathrm{W/m{\cdot}K}$
k_{22}	$0\,\mathrm{W/m{\cdot}K}$	$0\,\mathrm{W/m{\cdot}K}$
E_1	$557\,\mathrm{GPa}$	$54.4\,\mathrm{GPa}$
E_2	$6.23\,\mathrm{GPa}$	$15.9\,\mathrm{GPa}$
ν_{12}	0.318	0.252
$G_{12} = G_{13}$	$0.451\,\mathrm{GPa}$	$5.81\,\mathrm{GPa}$
G_{23}	$0.305\,\mathrm{GPa}$	$5.69\,\mathrm{GPa}$

Table 3.4: Material properties for isotropic shape memory alloy film [8, 35].

Material Property	**Value**
ρ	$6450\,\mathrm{kg/m^3}$
c_p	$329\,\mathrm{J/kg{\cdot}K}$
k	$22\,\mathrm{W/m{\cdot}K}$
E^A	$70\,\mathrm{GPa}$
E^M	$30\,\mathrm{GPa}$
ν	0.33
M_s	$259\,\mathrm{K}$
M_f	$233\,\mathrm{K}$
A_s	$278\,\mathrm{K}$
A_f	$305\,\mathrm{K}$
C^A	$6\,\mathrm{MPa/K}$
C^M	$7\,\mathrm{MPa/K}$
$H_{min} = H_{max} = H$	3.9%
$n_1 = n_2 = n_3 = n_4$	0.5

(see Fig. 3.7a). The sink temperature is assumed to remain at 10 K throughout the simulation, a condition that might be experienced if the radiator is shadowed from the sun by a planet or another part of the spacecraft. The convex and concave surfaces of the radiator are each assigned a radiation boundary condition (see Fig. 3.7b). The emissivity of the concave surface is 0.91, which corresponds to Martin black paint N-150-1 [18]. The emissivity of the convex surface is 0.04, which corresponds to a dark mirror coating composed of SiO-Cr-Al [18].

Per the solution procedure described in Section 3.1, separate thermal and structural models are employed. For this problem, both models are implemented using a finite element formulation in Abaqus. Although heat transfer problems are often analyzed using a finite difference approach, it is advantageous to employ the finite element method as this enables the use of a single mesh common to both solvers. In particular, the transfer of data from one model to the other for use in boundary conditions is

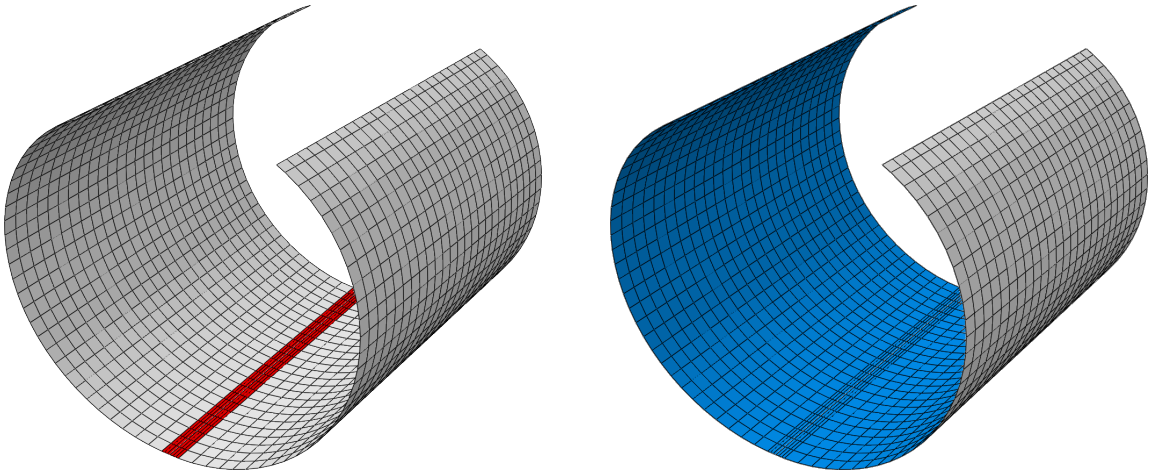

(a) Red surface: fixed boundary condition, uniform time-varying heat load [2].

(b) Blue surface: Radiation boundary condition with $\epsilon = 0.91$; white surface: radiation boundary condition with $\epsilon = 0.04$.

Figure 3.7: Finite element model showing structural and thermal boundary conditions.

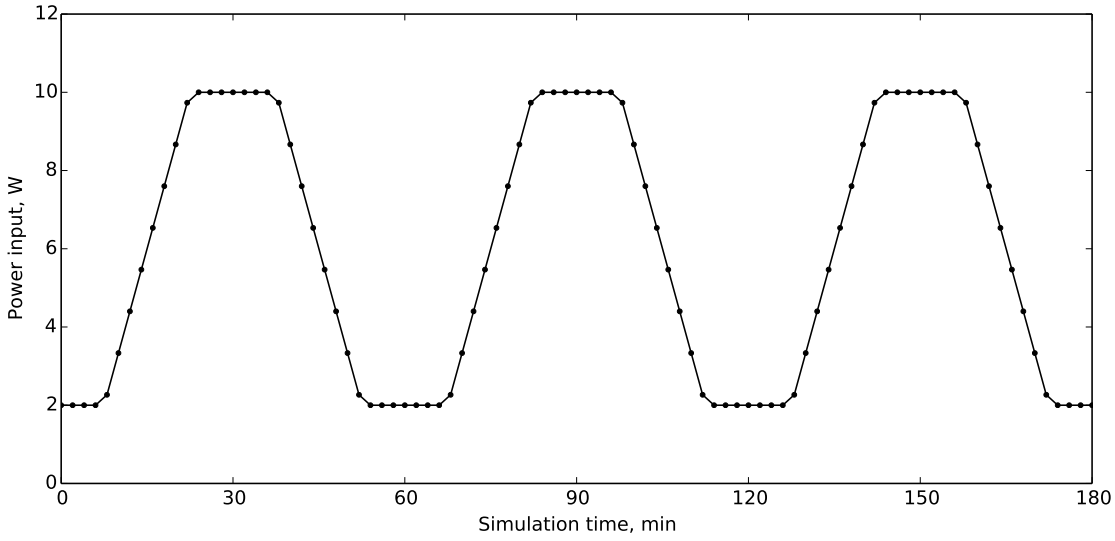

Figure 3.8: Heat load applied to the base of the radiator panel [2].

greatly simplified when the node locations are identical. For this problem, the finite element mesh consists of 1650 linear shell elements with three integration points through the thickness of each lamina.

The structural partition is implemented using a quasi-static analysis. The constitutive behavior of the shape memory alloy is included via a user material subroutine (UMAT) based on the constitutive model of Lagoudas, et al. [35], which is described in detail in Chapter 2. The structural solver uses a feature known as a *restart analysis* in order to stop and resume the simulation while maintaining its associated state variables (e.g. martensitic volume fraction) and fields (e.g. stress and strain) [12]. This feature is essential to capture the history dependence of the shape memory alloy constitutive behavior. The thermal solver is implemented with a heat transfer analysis which is capable of considering geometrically-dependent radiation boundary conditions. The heat transfer analysis may be either transient or steady-state. For this particular problem, a transient analysis is used.

The data exchange mechanisms are also simplified by using Abaqus for both partitions. The thermal model must import the displacement field from the previous structural solution, which can be accomplished in a straightforward manner. Likewise, the temperature field can be easily imported by the structural model. When using dissimilar tools for the partitions, the output data from one program may need to be modified to match the input format of the other program.

The thermal behavior of the radiator can be understood by investigating the evolution of the temperature and total heat emitted by the radiator. Figure 3.9 shows the evolution of the temperature field over the course of the simulation; the maximum, minimum, and average temperature within the radiator are plotted. Additionally, the deformed geometry is shown at several points in time with temperature contours superimposed. The horizontal dashed lines represent the stress-free transformation

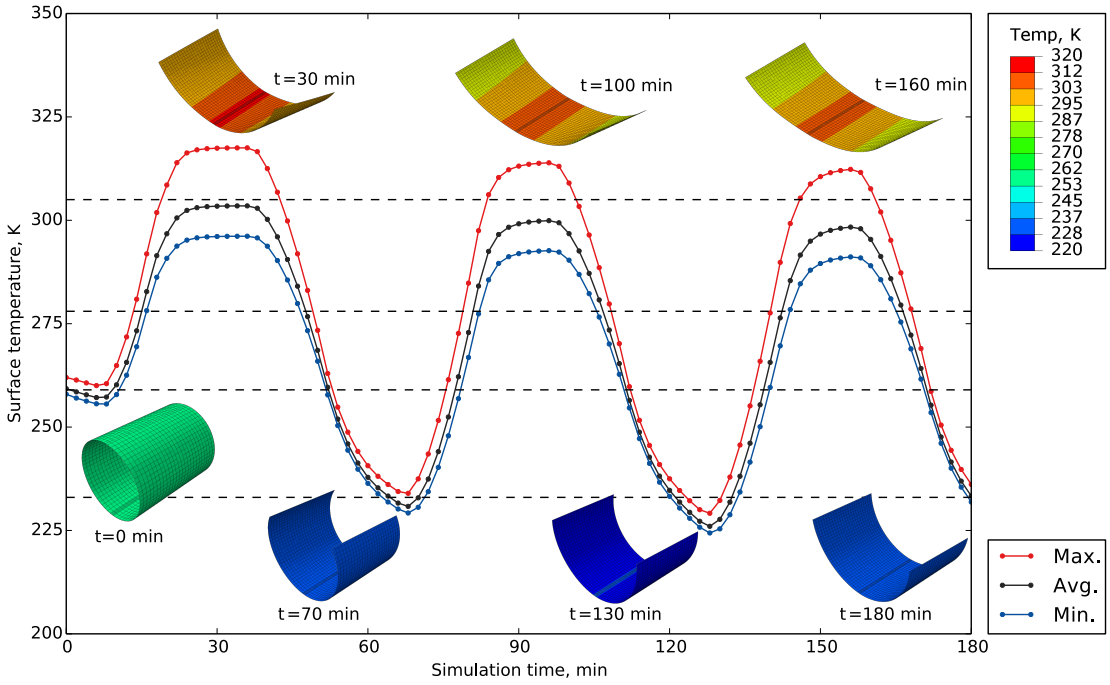

Figure 3.9: Maximum, minimum, and average temperature of the radiator in response to a time-varying heat load. Insets depict the temperature field within the radiator at various times [2].

temperatures of the shape memory alloy ($M_f < M_s < A_s < A_f$). Note that transformation from martensite to austenite occurs between A_s and A_f (reverse transformation), while transformation from austenite to martensite occurs between M_s and M_f (forward transformation). The radiator is initially in the fully-closed configuration at $T = 260\,\mathrm{K}$. As the heat load ramps from 2 W to 10 W, the temperature in the radiator begins to increase accordingly. After heating for approximately 15 min, the shape memory alloy begins to transform, causing the radiator to begin to open. By 30 min, the radiator reaches a steady-state open configuration with an average temperature of 302 K. The heat load begins to decrease at 38 min and the temperature decreases rapidly because the radiator is still fully open. As the SMA transforms

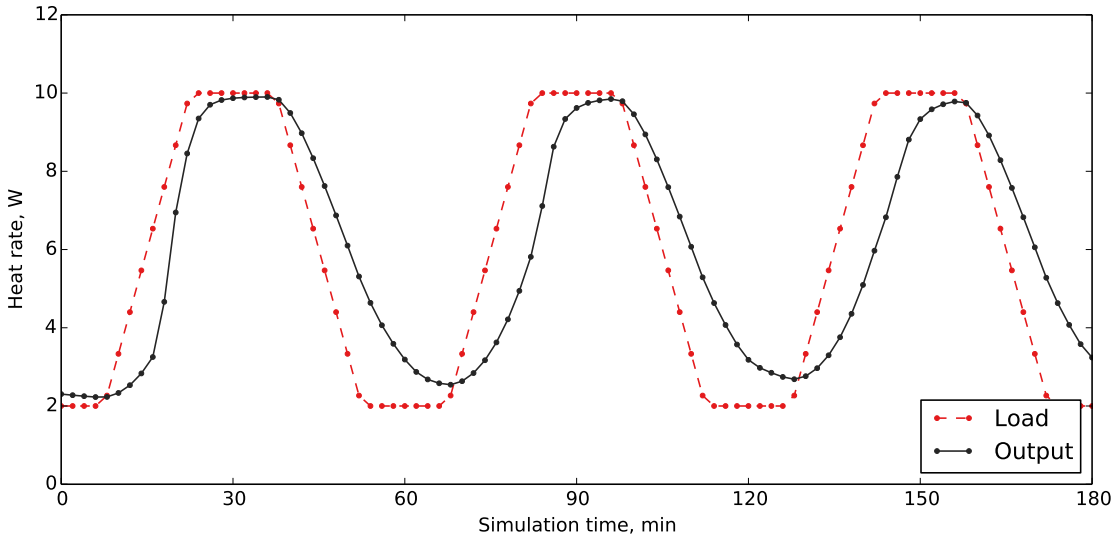

Figure 3.10: Total heat output of the radiator in response to the representative thermal load [2].

into martensite, the radiator begins to close back toward the minimum heat rejection configuration. A minimum average temperature of 230 K is reached just before the heat load begins to increase again at 70 min. The behavior of the radiator during the two remaining cycles is similar to the first cycle. Figure 3.9 also shows the spatial variation of the temperature field. In the hot condition (e.g. at $t = 30$ min), the maximum temperature is 313 K in the middle of the panel (above A_f), while the minimum temperature is only 294 K at the edges of the panel (below A_f). This implies even if the SMA transforms fully into austenite in the middle of the panel, it only transforms partially at the edges.

The total heat output of the radiator is plotted in Fig. 3.10 along with the applied heat load, where both are defined to be positive for the sake of comparison. During the heating phases (e.g. $0 < t < 30$ min), the heat output is smaller in magnitude than the load. As is seen in Fig. 3.9, this is because some of the energy is going

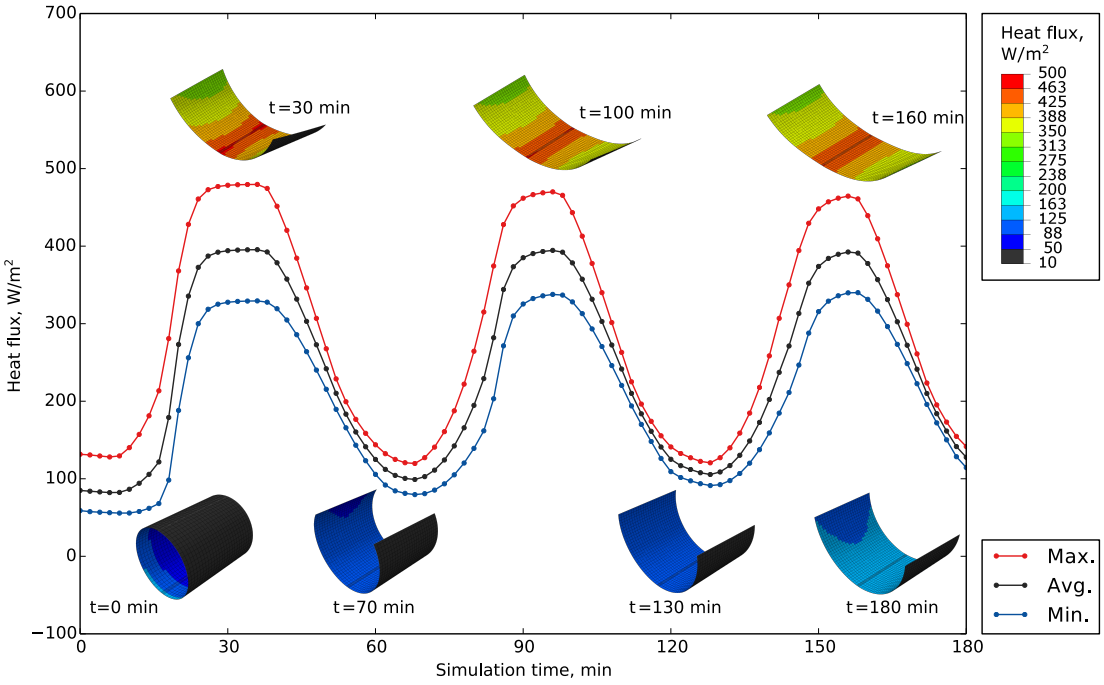

Figure 3.11: Maximum, minimum, and average radiation heat flux emitted by the concave radiating surface. Insets show the variation of heat flux over the radiating surface at various times [2].

toward increasing the temperature in the radiator panel, which means less energy is available to be radiated. Likewise, during the cooling phases (e.g. $30 < t < 70$ min), the heat output is higher than the load due to the additional heat given off during cooling. Figure 3.11 shows the variation of the heat flux emitted by the concave radiating surface. The heat flux of the convex surface is significantly lower (less than 20 W/m^2) due the surface's low emissivity; therefore, the data for the convex surface has been omitted from Fig. 3.11 for clarity. The variation in heat flux is most pronounced during the hot configuration, with the center of the panel emitting at a 47% higher rate than the outer edges (485 W/m^2 vs. 330 W/m^2).

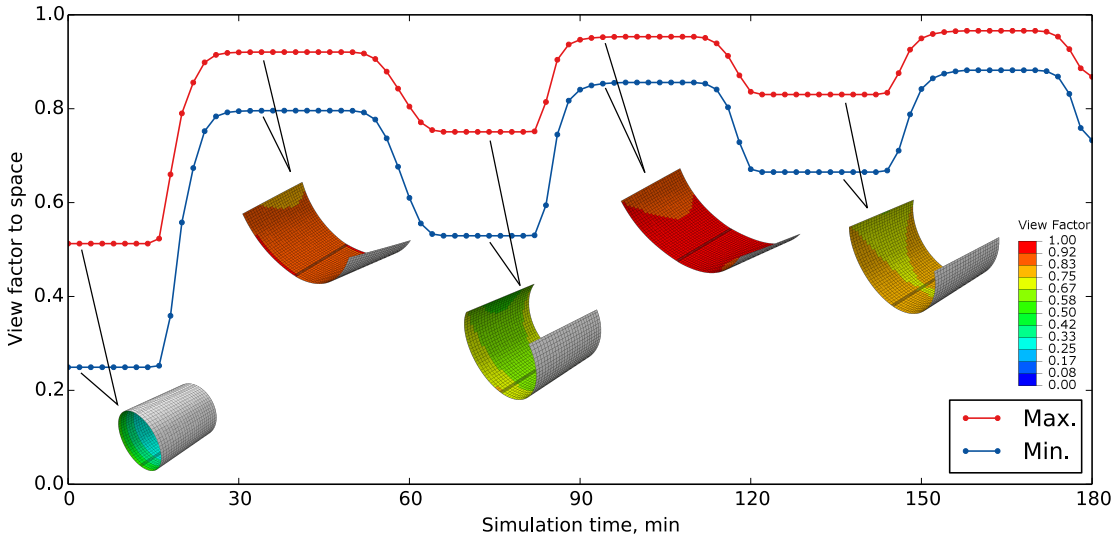

Figure 3.12: Maximum and minimum view factor to space. Insets show the variation of the view factor over the radiating surface at various times.

Figure 3.12 shows the maximum and minimum view factor of the elements on the panel to space. As before, the insets show the spatial distribution at several points in time. This plot clearly shows how the radiator is able to vary its heat rejection: the panel begins in the circular configuration at $t = 0$ with a maximum view factor of 0.51 and a minimum view factor of 0.22. As the panel opens, the view factor increases significantly to a maximum of 0.90 and a minimum of 0.79. Likewise, as the panel closes, the view factor decreases. During subsequent cycles, the panel is able to a slightly more open configuration, which results in a maximum view factor near unity.

4. EXPERIMENTAL CHARACTERIZATION OF A PROTOTYPE MORPHING RADIATOR[1]

Prior to this work, there had been little to no experimental testing of an SMA-actuated component in an exclusively radiative environment. Cognata et al. conducted experimental proof-of-concept studies on two SMA-based morphing radiator analogues; however, these studies were done in a laboratory environment where convection was the dominant mode of heat transfer [8]. As discussed in Chapter 2, for SMA-actuated components operating in a convection-dominated environment, changes to the geometry do not strongly affect the temperature field. Therefore, one of the primary goals of this work was to design, construct, and subsequently test for the first time a prototype morphing radiator in a thermal vacuum chamber in order to create a thermal environment similar to one in which the radiator is expected to operate on a future mission. In addition to demonstrating the operating principles of the morphing radiator concept, the data collected during the experiment was used to evaluate the physical accuracy of the analysis approach discussed in the prior chapter. The remainder of this chapter describes the design of the morphing radiator prototype itself as well as the overall test setup and presents the results of the test.

4.1 Morphing Radiator Prototype Design

Figure 4.1 shows the prototype morphing radiator which was designed and fabricated for the experimental study. This prototype uses shape memory alloy wires to achieve the temperature-induced morphing behavior described in the Introduction and depicted schematically in Fig. 1.3: at temperatures above the austenite finish

[1]Portions of this material reprinted from the Proceedings of the 24th AIAA/AHS Adaptive Structures Conference (2016), DOI 10.2514/6.2016-1568 [3], by permission of the American Institute of Aeronautics and Astronautics.

temperature (A_f) of the SMA wire, the radiator takes on an open, semicircular shape; at temperatures below the martensite finish temperature (M_f), the radiator takes on a closed, circular shape. Note that Fig. 4.1 shows the austenitic (high-temperature) configuration of the radiator prototype, corresponding to Fig. 1.3a. The primary component is a compliant and thermally conductive copper panel, 7 in (17.78 cm) long, 3 in (7.62 cm) wide, and 0.007 in (0.1778 mm) thick, which is rolled along its length to form the semicircular shape shown in Fig. 4.1. Ten shape memory alloy wires rest against the outer surface of the panel and are fixed at each end to the straight edges using set screws and a pair of terminal blocks fabricated from 0.25 in (6.35 mm) square aluminum stock. The wires are otherwise unconstrained, allowing them to slide along the panel as they transform locally. Benchtop tests indicated the need for an additional biasing force beyond that provided by the copper panel alone to allow the panel to close to the circular shape shown in Fig. 1.3c under cooling; a 1 in (2.54 cm) wide and 0.007 in (0.1778 mm) thick 1095 steel closing spring with a stress-free radius of curvature of 0.7 in (1.778 cm) is attached to the convex side of the panel for this purpose. In order to increase the rate of heat rejection via radiation in the open shape, the inside surface of the copper panel is painted with Aeroglaze Z307, a flexible, high-emissivity polyurethane coating. The outside of the panel remains unpainted. Note that the total hemispherical emissivities of the Aeroglaze Z307 paint, unpainted copper, and unpainted steel were measured to be 0.943, 0.047, and 0.143, respectively with a Surface Optics Corp. ET-100 emissometer. The copper panel is attached to a 0.375 in (9.53 mm) diameter stainless steel flow tube using a thermally conductive epoxy which allows the radiator to be integrated into a pumped fluid loop for the experiment.

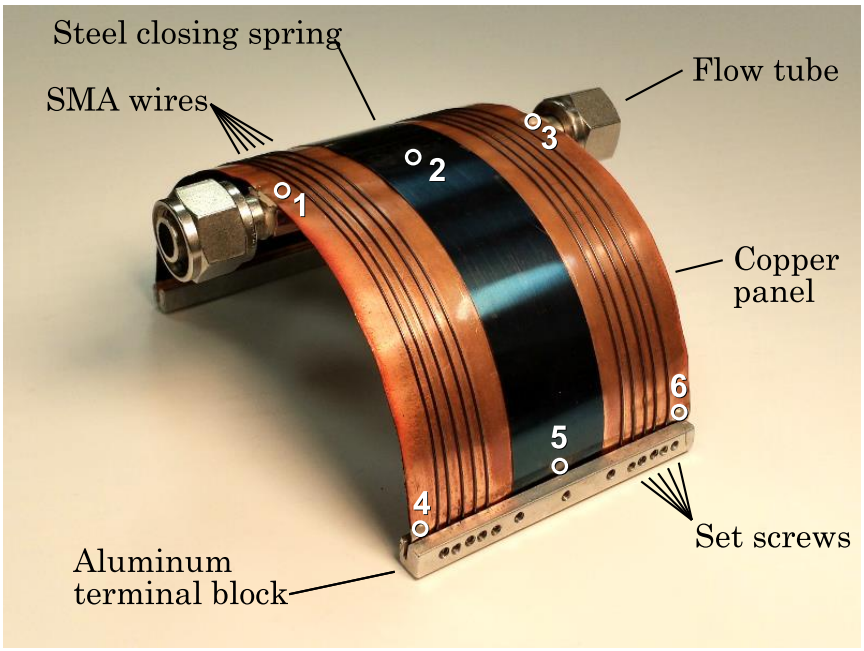

(a) Outside of prototype showing primary components.

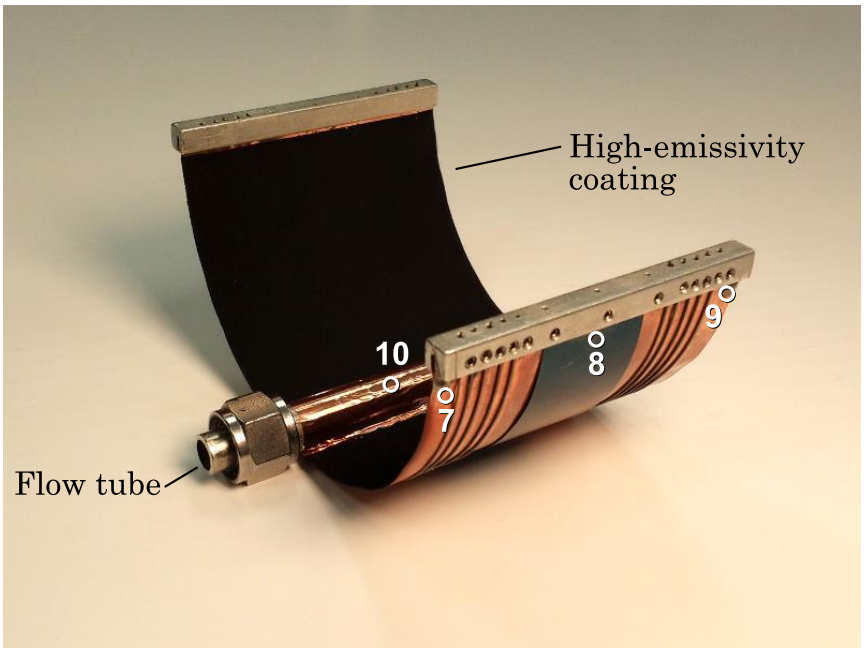

(b) Inside of prototype showing high-emissivity polyurethane coating.

Figure 4.1: Prototype morphing radiator design at room temperature demonstrating open shape. Open circles show thermocouple locations.

4.2 SMA Wire Characterization and Model Calibration

After the prototype itself had been designed, the next task was to select a particular shape memory alloy wire for the experiment. Traditional SMA actuator wire typically has an A_s temperature near 90°C, which is significantly higher than the setpoint of most thermal control systems onboard crewed spacecraft. Additionally, achieving such high temperatures can be difficult when operating in a vacuum chamber whose walls are below -150°C. As a result, this particular application called for wire with transformation temperatures below room temperature, which is sometimes referred to as *pseudoelastic* or *superelastic*.

SAES Getters provided a small quantity of trained NiTi SmartFlex wire with a diameter of 0.014 in (0.36 mm) and an austenite start temperature (A_s) of -25°C. This wire was tested using an *isobaric* thermomechanical cycle [22] prior to the experiment in order to fully characterize the behavior of the wire. For this type of test, the wire was held at a constant stress using a load frame and the temperature was cycled using a thermal chamber in order to induce transformation (see Fig. 4.2 for a picture of the load frame and thermal chamber). Figure 4.3 shows the total strain in the wire as a function of temperature for stresses of 100, 150, 200, and 250 MPa. At each stress level, the temperature was cycled between 60°C and -60°C. This plot indicates that the wire is able to provide up to approximately 6.5% transformation strain with nearly full recovery. The standard characterization method for shape memory alloys [22] was applied in order to determine the transformation temperatures at each stress level; the resulting data is shown in Fig. 4.4. The four transformation surfaces are shown with dashed lines: the blue lines indicate when transformation from austenite to martensite occurs; the red lines indicate when transformation from martensite to austenite occurs. Extrapolating the transformation temperatures to zero stress gives

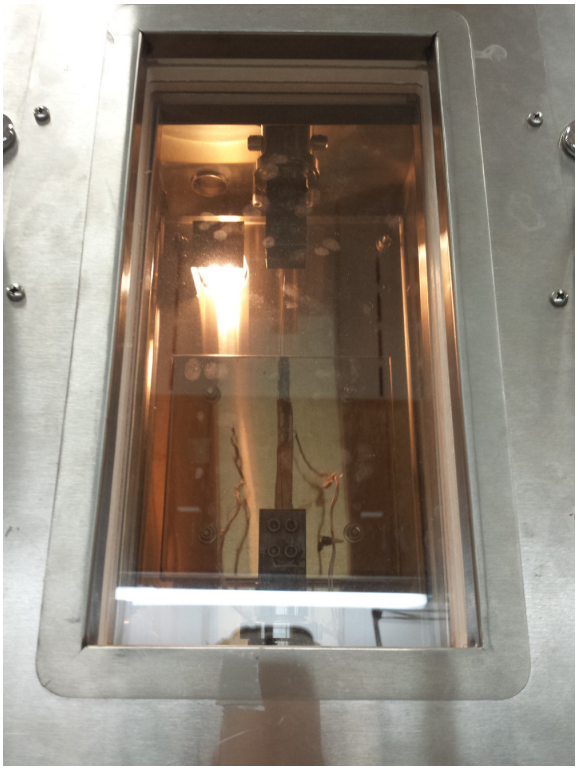

Figure 4.2: Photograph showing the load frame and thermal chamber which were used for the isobaric test.

an estimated zero-stress austenite start temperature (A_s) of -21.6°C, which agrees with the manufacturer-reported A_s of -25°C. Although this wire provides sufficient transformation strain, at low stresses, the martensite transformation temperatures are far below the freezing point of nontoxic working fluids. Based on this data, each wire was pretensioned in the prototype in order to increase the martensite transformation temperatures and allow a nontoxic, water-based working fluid to be used in the experiment.

Although the isobaric test gives a good understanding of the transformation behavior of the SMA wire, it does not provide enough data to fully calibrate the constitutive model described in Chapter 2. In particular, there is no means of

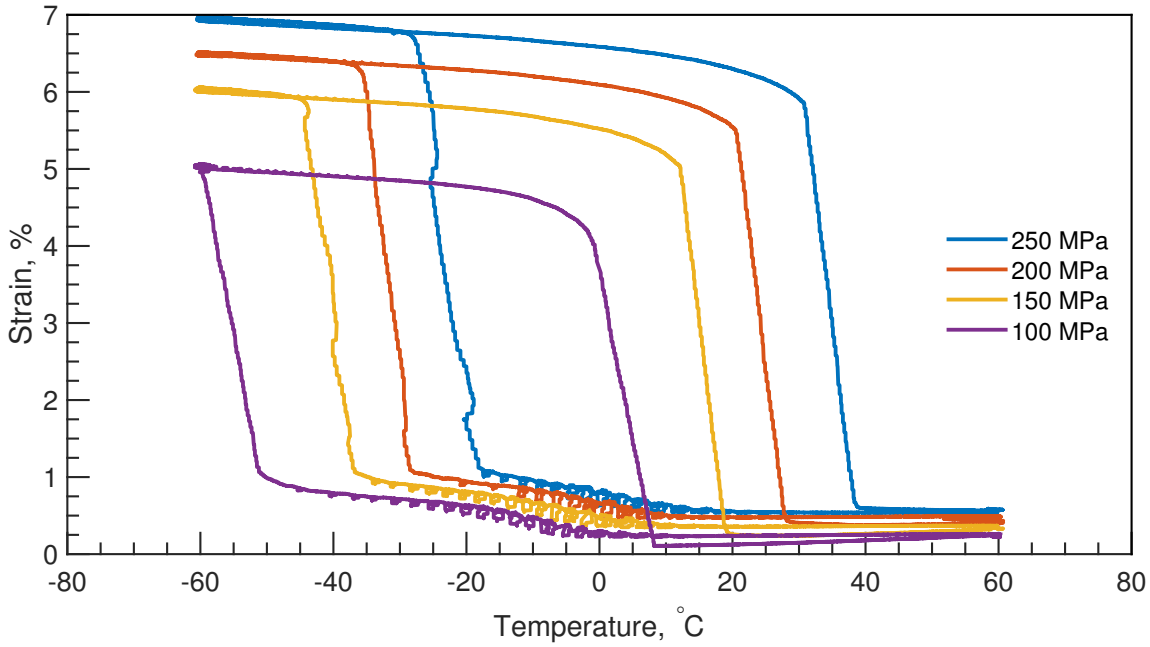

Figure 4.3: Results of the isobaric test of the 0.014 in (0.36 mm) SmartFlex SMA wire used in the morphing radiator prototype.

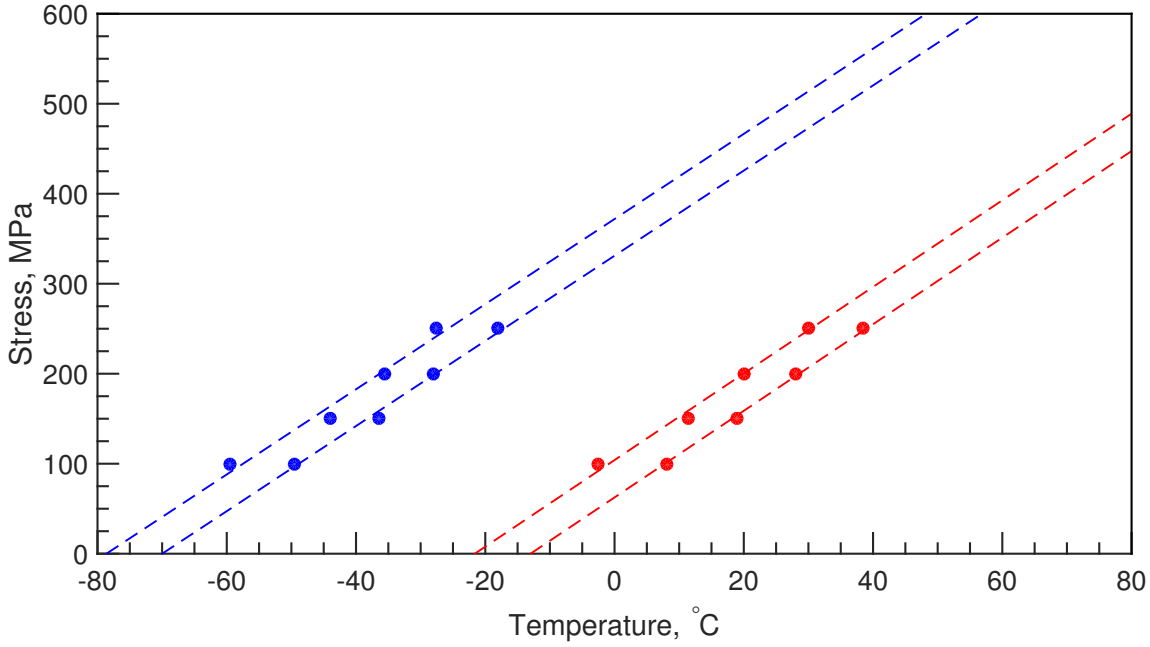

Figure 4.4: Experimentally-determined phase diagram for the SMA wire using the isobaric test data shown in Fig. 4.3.

determining E^M, the elastic modulus of martensite, from this data. Therefore, a second test was performed on the wire to allow E^M to be determined. For this test, the wire began in a stress-free configuration at room temperature in the austenite phase. First, the wire was loaded elastically to 600 MPa at a constant strain rate of 0.05%/s. Next, the wire was cooled to -40°C at a rate of 7°C/min while the stress was held at 600 MPa to allow the material to transform into martensite. Finally, the the wire was unloaded elastically at -40°C.

Figure 4.5 shows the response of the wire in stress-strain space during the second characterization test. The left diagonal part of the curve represents the elastic response of pure austenite during loading, while the right diagonal part of the curve represents the elastic response of pure martensite during unloading[2]. In order to determine E^A and E^M from this data, two tangent lines were fit using the method of least squares; the slope of each line gives the corresponding value of E. Fig. 4.5 shows the two tangent lines where the length of the lines indicates the subset of the data used in the least-squares data fits, giving $E^A = 54.6\,\text{GPa}$ and $E^M = 33.2\,\text{GPa}$.

Following the procedure outlined by Lagoudas [34, 35], the SMA constitutive model described in Chapter 2 was calibrated twice, using different assumptions for the parameters. The model was first calibrated assuming $\alpha^M \geq 0$ and $\alpha^A \geq 0$, which will be referred to as "Calibration 1." Table 4.1 lists the full set of parameters needed to define the constitutive response of the wire. Figure 4.6a shows the phase diagram as determined by the model along with the experimentally-determined transformation temperatures, which are shown with closed circles. Figure 4.6b shows the model predictions of the strain in the wire during the isobaric experiment, where grey dashed lines are used for the experimental data shown in Fig. 4.3. Overall, these figures

[2]Although it is possible to determine E^A from the isobaric data shown in Fig. 4.3, the data from the second characterization test provides a convenient means of calculating E^A and E^M simultaneously.

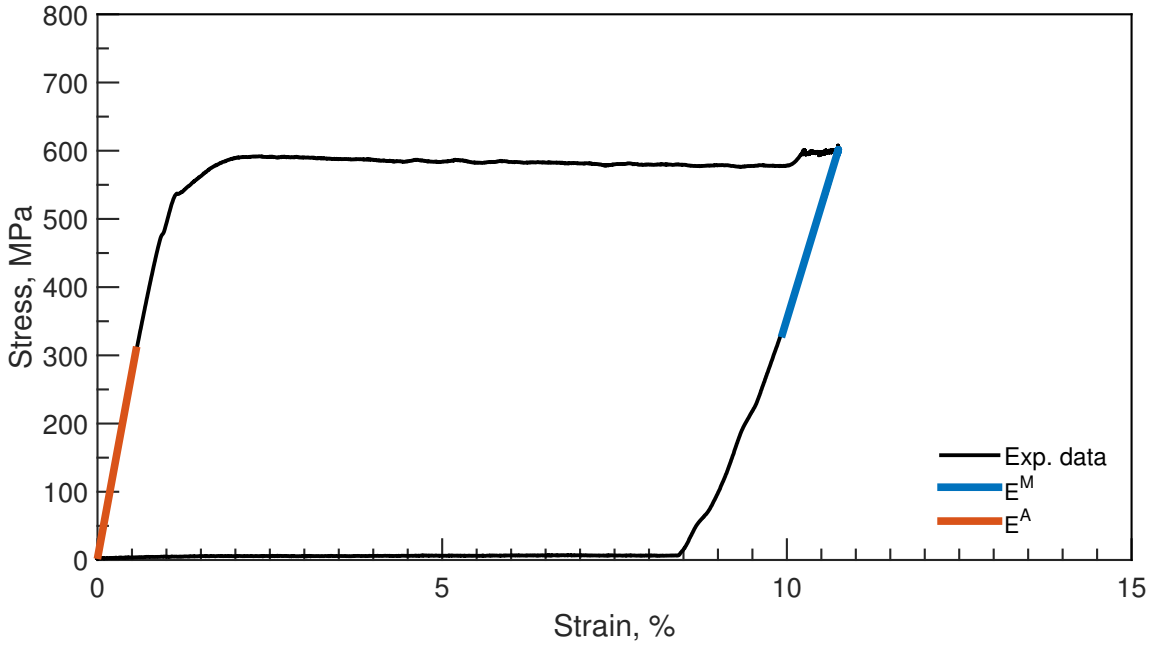

Figure 4.5: Stress-strain response of the SMA wire during the second characterization test showing data fits for E^M and E^A.

show that Cablibration 1 matches the response wire fairly closely. The austenite transformation temperatures (shown in red in Fig. 4.6a) are accurately predicted the model; this can also been on the right side of the loops in Fig. 4.6b. However, there is slightly more spread in the martensite transformation temperatures and, as a result, the model does not match the left side of the loops for all stress levels; at 100 and 200 MPa, the model matches the martensite transformation temperatures very well, however, at 150 MPa, the model slightly underpredicts the martensite transformation temperatures and at 250 MPa, the model slightly overpredicts them. Note that the model is able to very accurately predict the maximum total strain as a function of stress. For example, at 150 MPa, the maximum total strain in the wire as predicted by the model is 6%, which can be seen to match the experimental data very closely. However, Calibration 1 is unable to predict the gradual strain recovery as the wire

transforms into austenite under heating. This can be seen along the upper portion of each isobaric loop: the total strain at each stress level remains constant until the M_s temperature, whereas the experimental data indicates that the wire begins to recover the stress well before the M_s temperature.

In order to better capture this effect, the model was calibrated a second time assuming $\alpha^M < 0$, which will be referred to as "Calibration 2." Table 4.1 lists the resulting parameters, while Fig. 4.7 shows the phase diagram and isobaric response for Calibration 2. Figure 4.7 shows that setting $\alpha^M = -5{\cdot}10^{-5}$ allows the model to capture the gradual recovery much more accurately than when $\alpha^M = 0$ in Calibration 1. Note that the transformation temperatures are slightly lower than those for Calibration 1, and H_{min} and H_{max} have decreased as a result of the negative expansion coefficient.

Table 4.1: Calibrated model parameters for the 0.014 in (0.36 mm) diameter SmartFlex wire.

Model Parameter	**Calibration 1**	**Calibration 2**
E^M	33.2 GPa	33.2 GPa
E^A	54.6 GPa	54.6 GPa
ν^M	0.33	0.33
ν^A	0.33	0.33
α^M	$0 \cdot 10^{-6}$ m/(m·°C)	$-5 \cdot 10^{-5}$ m/(m·°C)
α^A	$1 \cdot 10^{-6}$ m/(m·°C)	$1 \cdot 10^{-6}$ m/(m·°C)
M_f	197.7 K	196.2 K
M_s	206.5 K	204.9 K
A_s	255.8 K	254.8 K
A_f	264.5 K	263.5 K
C^M	4.26 MPa/K	4.29 MPa/K
C^A	4.60 MPa/K	4.58 MPa/K
H_{min}	2.00%	1.40%
H_{max}	6.48%	5.88%
k	0.0123 MPa^{-1}	0.0123 MPa^{-1}
$\bar{\sigma}_{crit}$	20 MPa	20 MPa
n_1	1.00	1.00
n_2	0.87	1.00
n_3	1.00	1.00
n_4	0.87	0.51

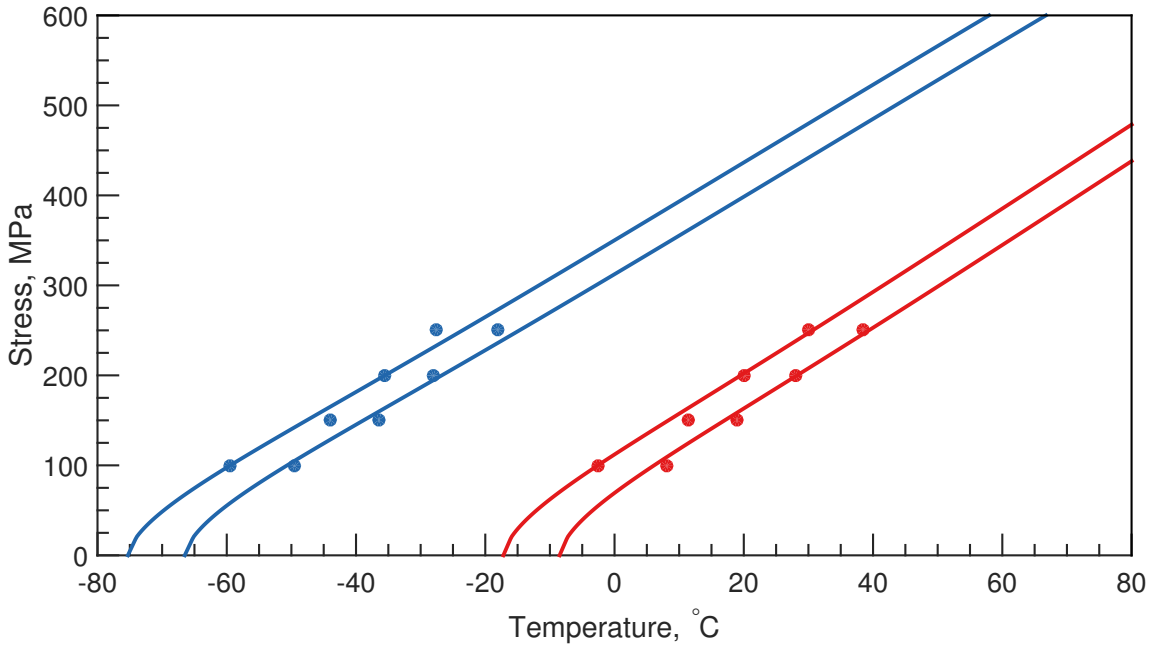

(a) SMA constitutive model phase diagram (Calibration 1).

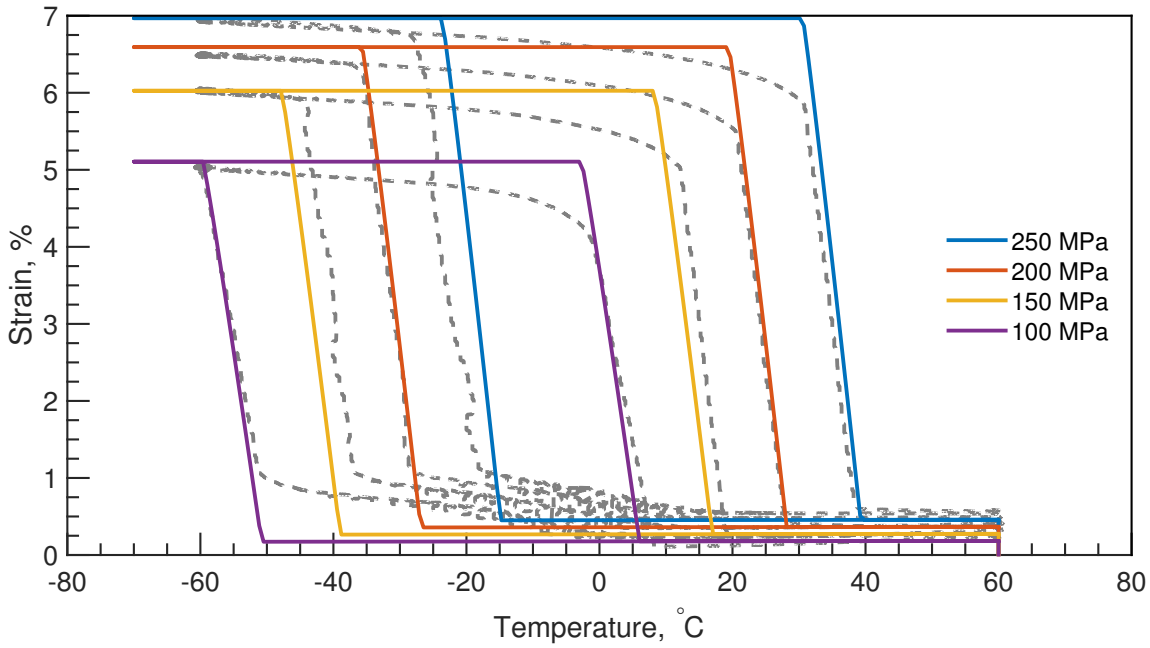

(b) SMA constitutive model prediction of the isobaric response of the wire (Calibration 1).

Figure 4.6: Phase diagram and isobaric response as determined by the SMA constitutive model (Calibration 1).

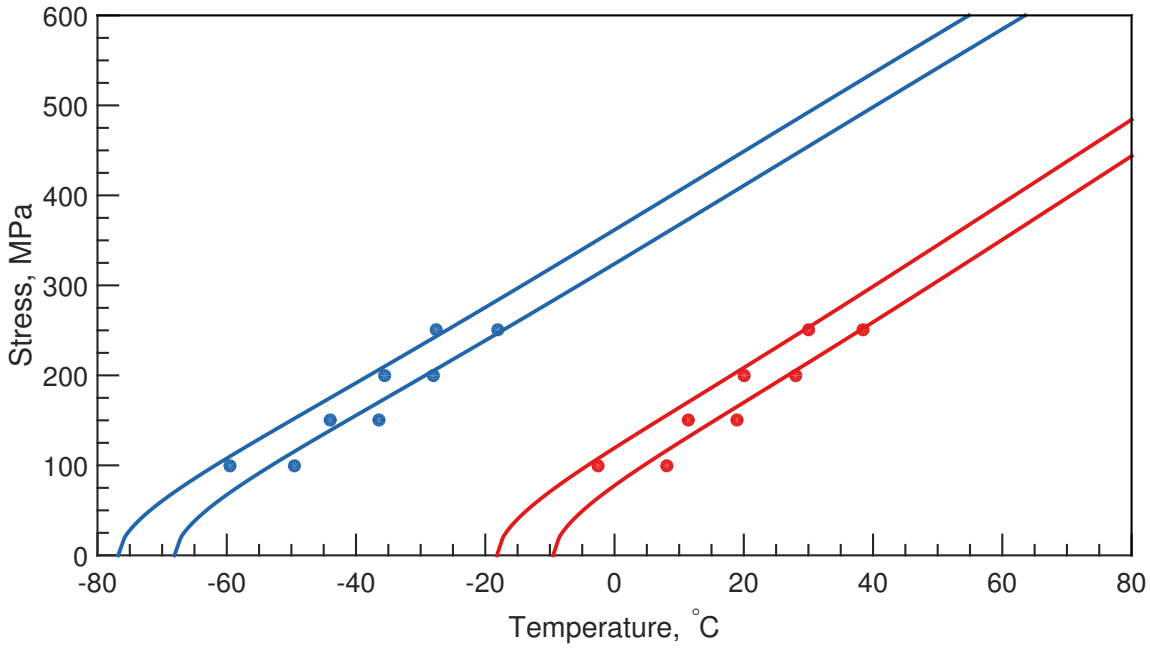

(a) SMA constitutive model phase diagram (Calibration 2).

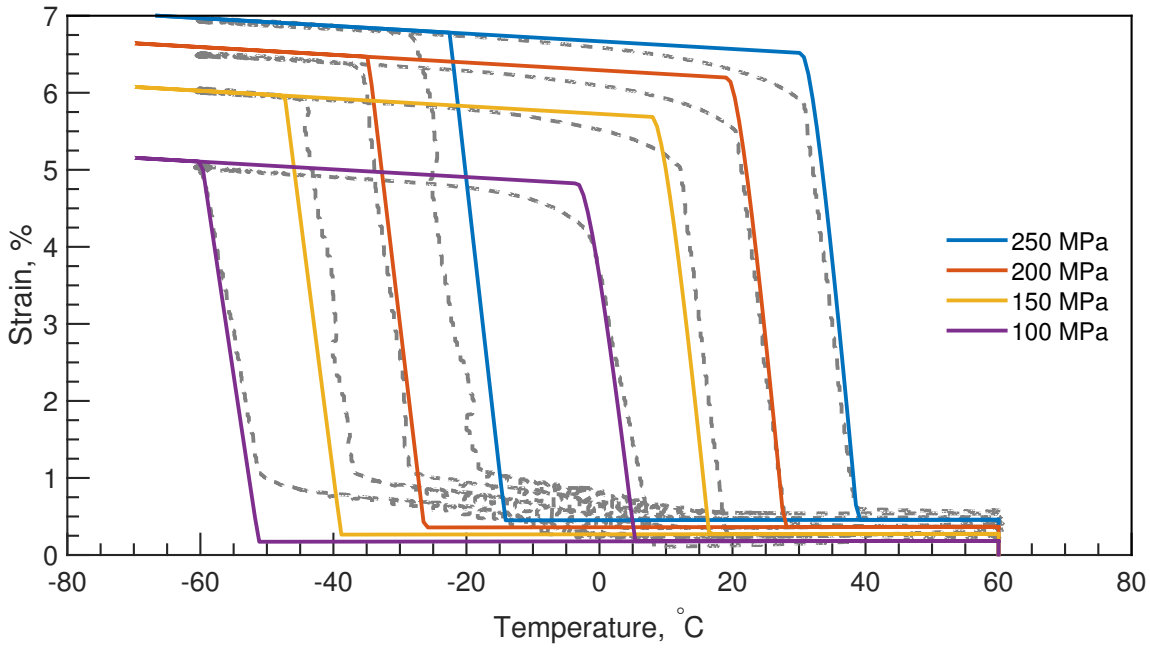

(b) SMA constitutive model prediction of the isobaric response of the wire (Calibration 2).

Figure 4.7: Phase diagram and isobaric response as determined by the SMA constitutive model (Calibration 2).

4.3 Morphing Radiator Prototype Fabrication Procedure

Figure 4.8 shows the major steps required to fabricate the test specimen. The procedure began with a flat copper panel which was cut to the desired size (7 in × 3 in) out of 0.007 in annealed copper shim stock. One side of the panel was treated with Aeroglaze 9924 primer and then painted with Aeroglaze Z307, a flexible, high-emissivity polyurethane coating. The other side was left unpainted. Figure 4.8a shows the painted side of the panel. The panel was then rolled uniformly along its length to form a semicircle; the Aeroglaze Z307 paint proved to be durable and flexible enough to allow the panel to be rolled without damaging the paint. A 3/8 in diameter stainless steel flow tube was then attached to the panel using Arctic Silver Thermal Adhesive. Figure 4.8b shows the panel after being rolled and attached to the flow tube. In this photograph, the panel is resting on top of an assembly jig which was used to hold the specimen in place during the remainder of the assembly procedure. The jig consisted of a curved aluminum plate with a radius of curvature of 5 in. A layer of tape was placed on the jig to protect the painted surface of the panel from damage and a slot allowed the panel to be placed on the jig with the painted side facing down as shown in Fig. 4.8c. After positioning the panel on the jig, the aluminum terminal blocks were then attached to the edges of the copper panel as shown in Fig. 4.8d. Next, the steel closing spring was placed on the panel and secured with set screws in the terminal blocks as shown in Fig. 4.8e. The final step was to add the SMA wires. This consisted of passing each wire through its respective guide hole in the terminal blocks, pretensioning the wire by suspending 5.33 lb from each end with a pair of locking pliers, and subsequently tightening the corresponding set screw. Figure 4.8f shows the fully constructed specimen after attaching the SMA wires.

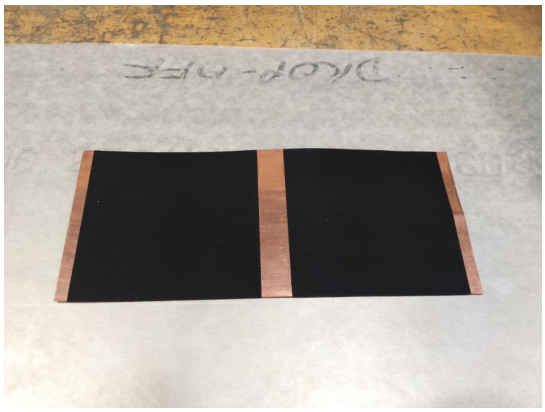

(a) Flat copper panel after being painted with high-emissivity polyurethane coating.

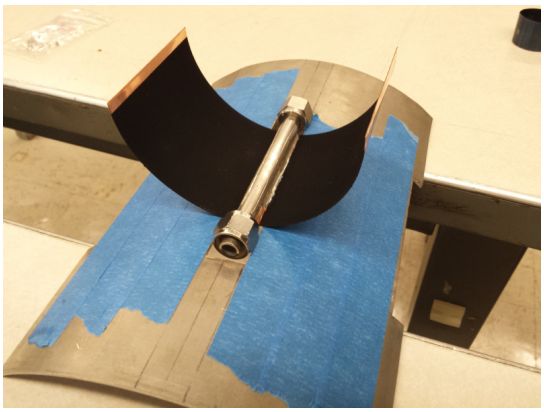

(b) After rolling panel and attaching flow tube.

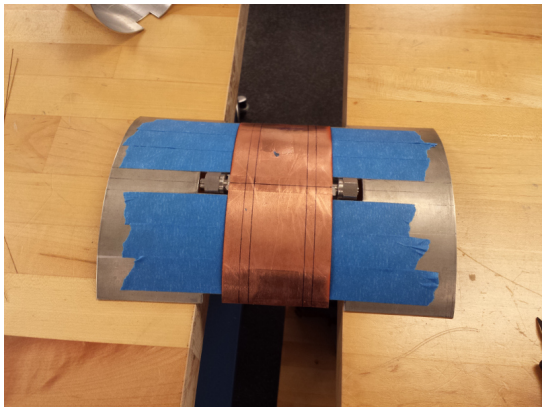

(c) On assembly jig.

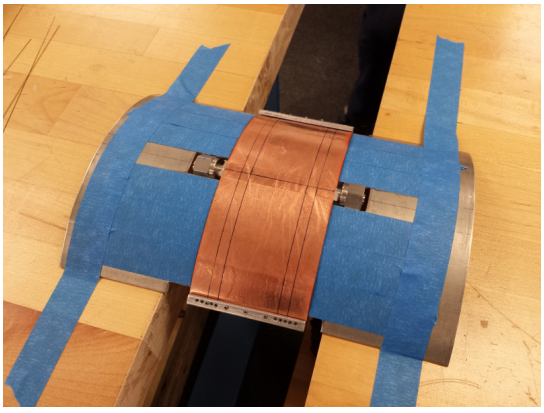

(d) After attaching terminal blocks.

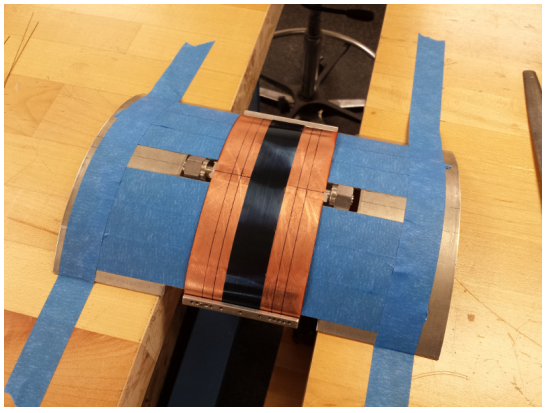

(e) After attaching spring steel strip.

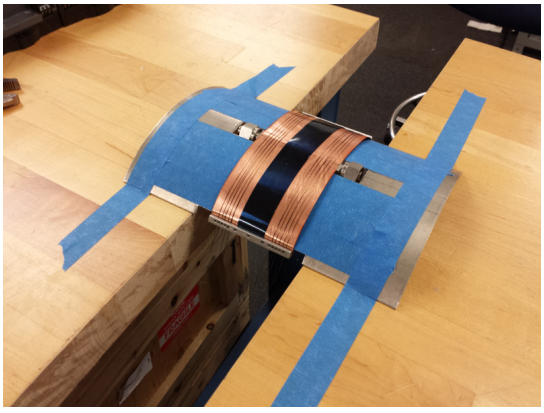

(f) After attaching SMA wires.

Figure 4.8: Sequence showing fabrication procedure for morphing radiator prototype.

Figure 4.9: Photograph showing morphing radiator on the assembly jig just prior to being installed in the vacuum chamber.

The specimen was transported to the vacuum chamber on the assembly jig to prevent any damage from handling. Figure 4.9 shows the radiator prototype and assembly jig resting inside the vaccum chamber immediately before the radiator was installed. Note that the thermocouple leads are also visible in this photograph.

4.4 Experimental Setup

The prototype morphing radiator was incorporated into a simple fluid loop which used an SP Scientific RC211 pump with an integrated heater and refrigerator to vary the fluid temperature. The fluid loop used Dynalene HC-50 as the working fluid, a nontoxic water-based coolant with a freezing point below -50°C. The flow rate of the system was set sufficiently high to ensure the fluid temperature at the radiator outlet remained within 0.5°C of that at the radiator inlet; given the high flow rate and high heat capacity of the working fluid relative to the radiator panel, the result is a boundary condition which closely approximates a uniform temperature boundary condition. The fluid loop and radiator were installed in a small, high-vacuum environment chamber located at NASA Johnson Space Center. The cylindrical test section has a diameter of 17 in (43 cm) and a depth of 23 in (58 cm) and is surrounded by a temperature-controlled shroud that provides a surface to which the radiator can reject heat. The radiator was suspended in the center of the test section with the high-emissivity surface facing downward. This position allowed the panel to be viewed through a small glass window on the door of the test section. Figure 4.10 shows the overall experimental setup, with the chamber itself, the temperature-controlled pump outside the chamber, and the working fluid lines passing into and out of the test section via ports on the side of the chamber. Ten Type T thermocouples were attached to the test specimen at the locations shown in Fig. 4.1 to measure the temperature at key points on the panel and a digital camera was attached to the outside of the window on the chamber to record the radiator's deformation.

Prior to the start of the experiment, the pump was turned on and the fluid temperature was increased from room temperature to 65°C. The chamber was pumped down to a pressure of 10^{-5} torr and the shroud was cooled with liquid nitrogen until

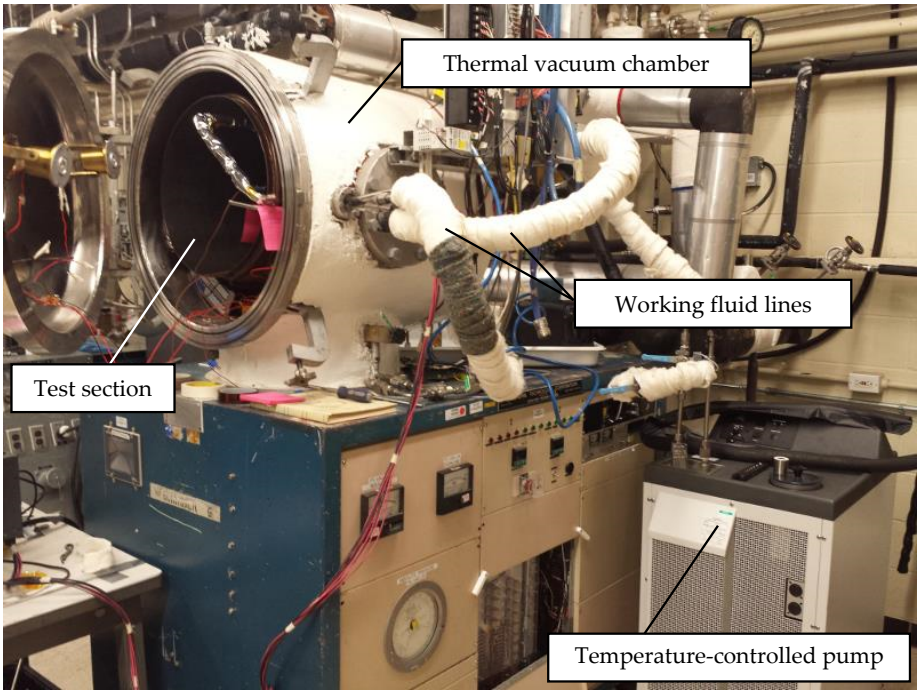

Figure 4.10: Photograph showing experimental setup, including thermal vacuum chamber and pump [3].

it reached a temperature of -178°C. The experiment began with a 10-minute dwell period to allow the system to reach equilibrium. Next, the working fluid was cooled to -45°C and maintained at -45±4°C for 20 minutes. The fluid was then heated to 60°C over the next 3 hours. Figure 4.11 shows the fluid temperature at the radiator inlet and outlet as measured by the two immersion thermocouples. This plot clearly shows that the fluid temperature remained nearly constant across the radiator throughout the experiment.

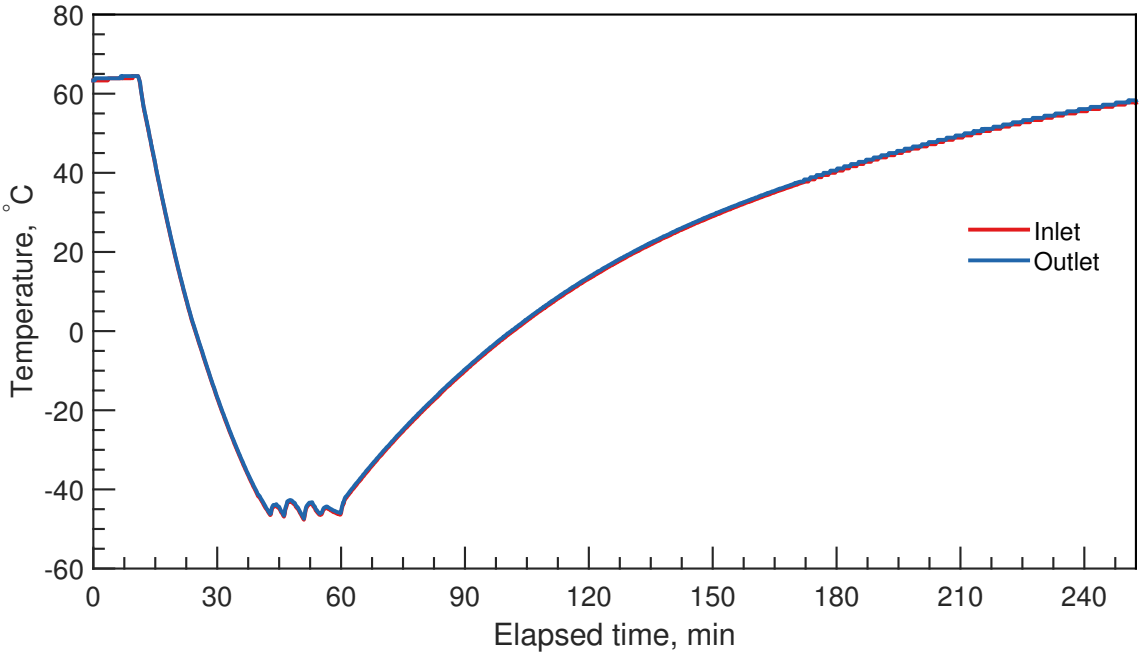

Figure 4.11: Time history of the working fluid temperature at radiator inlet and outlet.

4.5 Results and Discussion

Figure 4.12 shows the evolution of the temperature in the panel as measured by two of the attached thermocouples. The warmest temperatures are experienced by thermocouples 1 and 3 (see Fig. 4.1 for thermocouple numbering and locations), which are attached to the panel nearest to the flow tube, while the coolest temperatures are experienced by thermocouples 4, 6, 7, and 9, which are located along the edge of the panel farthest from the flow tube. As expected, these temperatures follow the trend of the fluid temperature, which is shown above in Fig. 4.11. At the beginning of the experiment, the difference between the maximum and minimum panel temperatures is approximately 25°C. As the fluid temperature decreases, the temperature field in

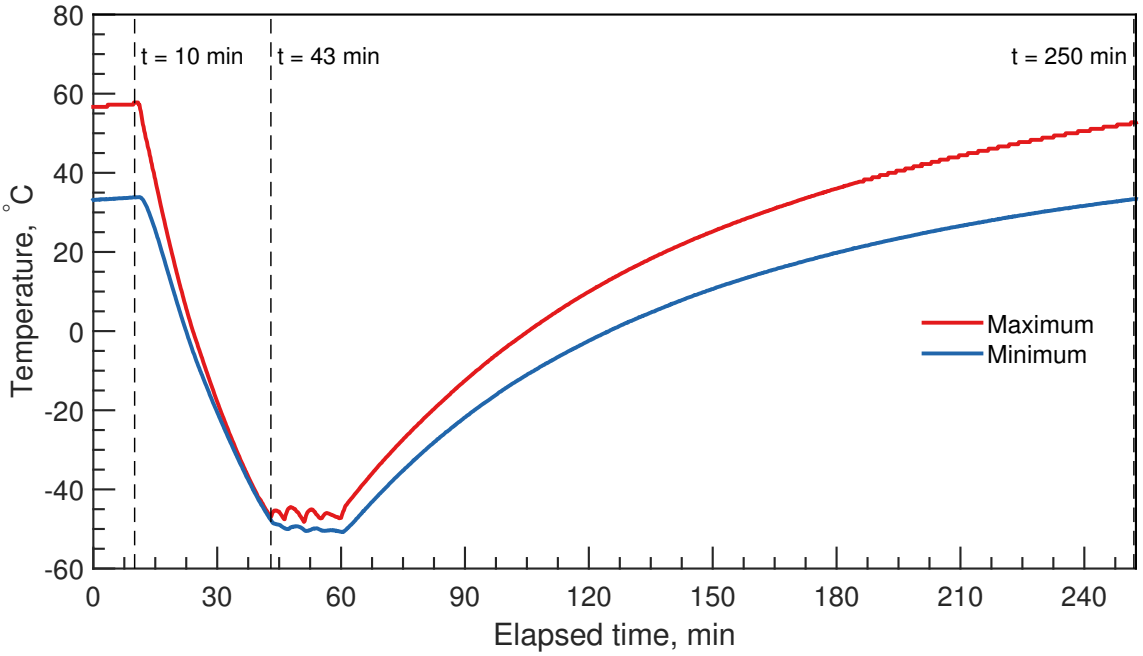

Figure 4.12: Time history of maximum and minimum panel temperatures. Vertical dashed lines correspond to images shown in Fig. 4.13.

the panel becomes more uniform. Likewise, as the fluid temperature increases, the temperature difference begins to increase.

While the temperature provides a straightforward means to characterize the thermal response of the radiator, it is more difficult to quantitatively describe the radiator's structural response (i.e. deformation) using the images captured during the test. Figure 4.13 shows three such images corresponding to key times during the experiment: Fig. 4.13a shows the initial shape of the radiator at the start of the experiment; Fig. 4.13b shows the closed shape reached by the radiator at the minimum fluid temperature; Fig. 4.13c shows the recovered shape at the end of the experiment. Note that the time corresponding to each image is marked with vertical dashed lines in Fig. 4.12. Due to imperfections in the prototype, the panel is not symmetric: in each image, the left half of the panel appears to be slightly more open than the right

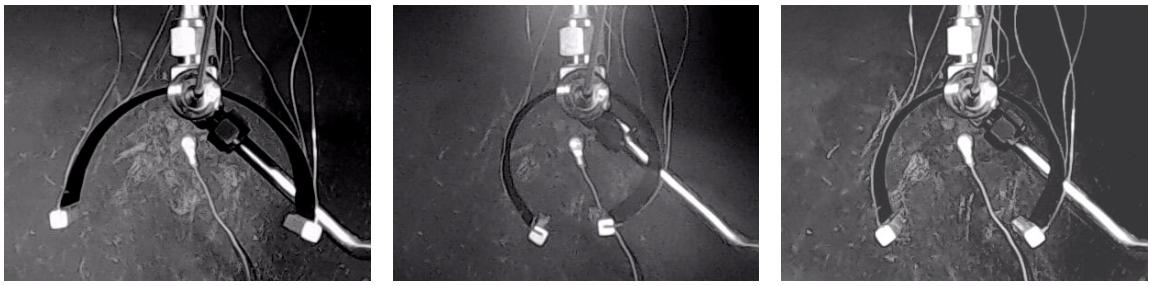

(a) Nearly semicircular shape for maximum fluid temperature ($t = 10\,\text{min}$).

(b) Nearly circular shape for minimum fluid temperature ($t = 43\,\text{min}$).

(c) Recovered shape at the end of the experiment ($t = 250\,\text{min}$).

Figure 4.13: Images of morphing radiator specimen at three points during the test demonstrating the desired temperature-induced actuation behavior [3].

half. Based on these images, it was decided to use two circular arcs to approximate the panel geometry, one for each half of the panel. Then, the radius of curvature of each arc provides a straightforward way to describe the deformation of the panel. A Matlab script employing the method of least squares was developed to fit arcs to each of a total of 18 images; the resulting data is shown in Fig 4.14. The upper and lower dashed lines in this figure correspond to an ideal, symmetric semicircular and circular shape, respectively. This plot clearly shows that the panel was able morph between a nearly semicircular shape at the beginning of the experiment (see Fig. 4.13a) and a nearly circular shape when the fluid temperature reached its minimum value (see Fig. 4.13b). It is interesting to note that the difference between the left and right radii, a measure of the asymmetry in the panel attributable to small fabrication errors/imperfections, remains approximately constant throughout the experiment.

It is challenging to describe the behavior of the shape memory alloy wires over the course of the experiment due to the temperature variation along the length of each wire: the local temperature at the material point in the wire nearest to the flow tube is

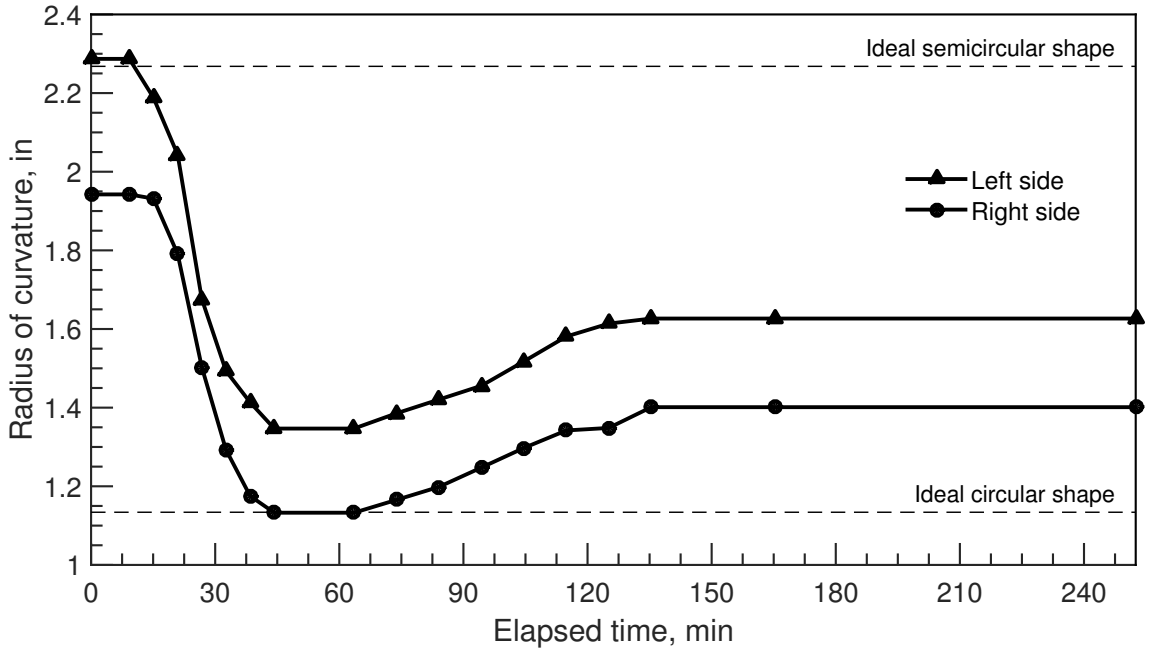

Figure 4.14: Time history of radius of curvature of left and right sides of morphing radiator panel.

higher than that at a material point at the edge of the panel near the terminal blocks. As a consequence, the wires do not transform uniformly along their length. Therefore, instead of considering the behavior of the entire wire, it is more helpful to consider the response of a single material point in the SMA wire. In particular, consider the material point nearest to the flow tube, which is also the warmest point in the wire. Figure 4.15 shows a simplified version of the experimentally-determined phase diagram shown above in Fig. 4.4 which will be used to explain the transformation behavior of this material point over the course of the experiment. Assume the material point begins at *1*, in the austenite phase at approximately 60°C and with an initial stress of 500 MPa. It should be noted that since there was no means of directly measuring the stress in the wire during the experiment, the values of the stress in this discussion should be understood as estimated values. No transformation occurs

as the material point cools from *1* to *2*; the temperature simply decreases while the stress remains at its initial value of 500 MPa. Beginning at *2*, the material point transforms from austenite to martensite as the temperature continues to decrease. As the material point transforms, the stress decreases due to the linearly elastic biasing load caused by the closing spring. This stress relaxation, in turn, causes the martensite finish temperature (shown with the leftmost dashed line) to decrease. The result is that the material point is unable to fully transform into martensite once the temperature reaches -45°C at *3*. As the temperature increases, no transformation occurs between *3* and *4*. At *4*, the material point begins to transform into austenite, increasing the stress in the process. This shifts the austenite finish temperature (shown with the rightmost dashed line) upward, preventing the material point from fully transforming into austenite (*5*). This diagram explains why the radiator was unable to fully recover the initial semicircular shape by the end of the experiment: even though the temperature returned to its initial value, the stress in the wires at the end of temperature cycle is less than that at the beginning of the experiment.

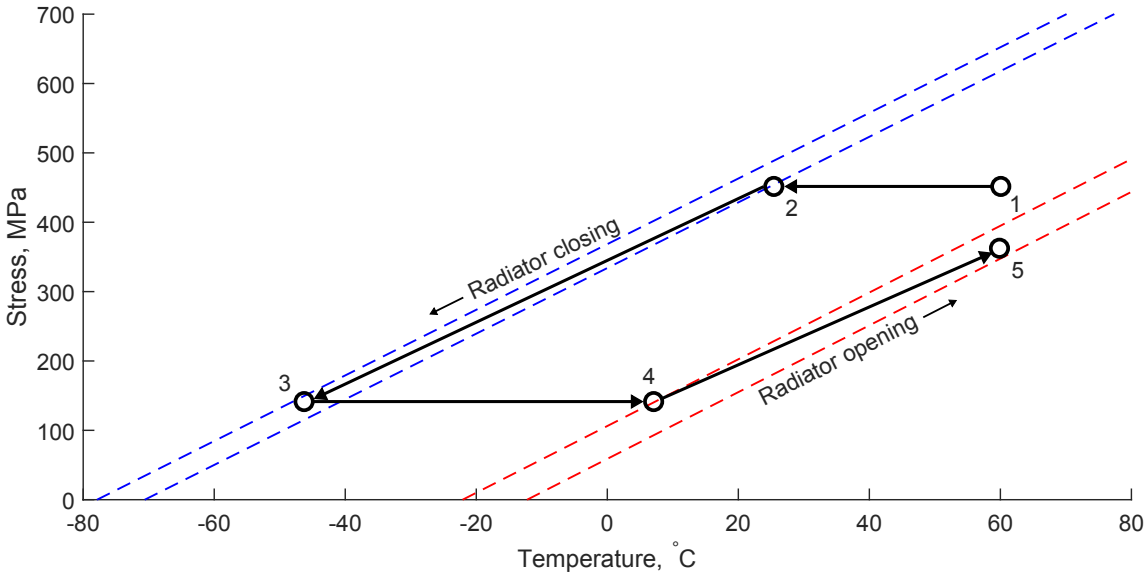

Figure 4.15: Phase diagram for the SMA wire showing the thermomechanical path experienced by the point nearest to the flow tube [3].

5. EVALUATION STUDIES

5.1 Thermal Finite Element Model

Although the data presented in the previous chapter gives an understanding of the morphing radiator's thermomechanical behavior over the course of the test, it is not possible to directly compute the radiator's rate of heat rejection from this data. Instead, a finite element model of the prototype was developed using the thermal module in Abaqus to allow this quantity to be determined. The model uses the data shown in Fig. 4.14 to construct an idealized representation of the radiator geometry corresponding to each radius pair. A constant temperature boundary condition is applied to the copper panel at the location of the flow tube using the corresponding maximum temperature measured in the panel (shown in Fig. 4.12). Radiation boundary conditions are applied to the surface of the panel using the emissivity values given in Sec. 4.1 and the panel is assumed to be radiating to an environment at -180°C, which was the measured temperature of the liquid-nitrogen-cooled chamber shroud during the experiment. The thermal response of the panel was assumed to be quasi-steady state, as the temperature field evolved over the course of several hours in the experiment. The model is meshed with 510 8-node quadratic shell elements with temperature degrees of freedom. The model was executed for each pair of radii from Fig. 4.14 along with the corresponding maximum panel temperature from Fig. 4.12. The minimum temperature as computed by the model is plotted in Fig. 5.1 along with the minimum temperature measured by the thermocouples during the experiment. This figure shows that the minimum temperature as computed by the finite element model closely matches the experimental data, which gives confidence in the thermal

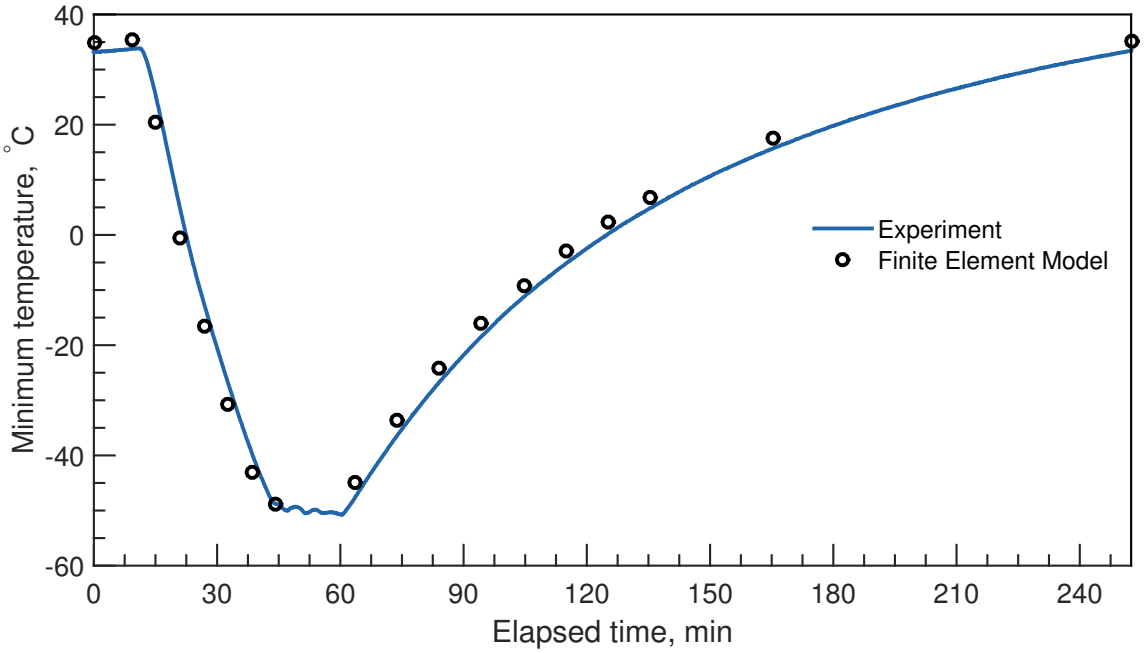

Figure 5.1: Comparison between the minimum panel temperature measured during the experiment and computed via the thermal finite element model.

analysis procedure in Abaqus, including its implementation of radiation boundary conditions.

More importantly, this model can be used to compute the radiator's total rate of heat rejection over the course of the experiment, which is plotted with the square markers and solid line in Figure 5.2. As expected, the heat rejection rate is relatively high, 5.93 W, at the beginning of the experiment when the fluid temperature is warmest and the radiator is in its most open configuration. As the fluid temperature decreases and the radiator closes, the heat rejection rate dramatically decreases to 0.92 W. The rate of heat rejection increases as the temperature subsequently increases and the panel returns to its open configuration. Taking the ratio between the maximum and minimum heat rejection values gives an estimated turndown ratio ($\dot{Q}_{max}$:$\dot{Q}_{min}$) of 6.4:1. To understand the effect of the morphing behavior on the

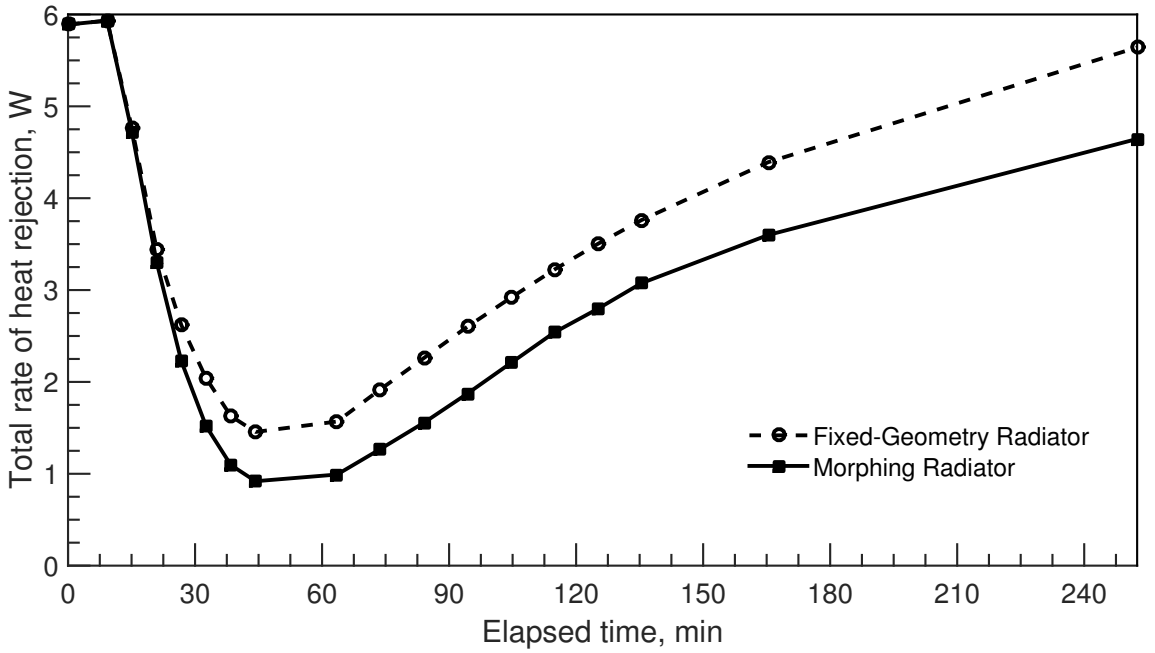

Figure 5.2: Total rate of heat rejection as computed via the finite element model for morphing and equivalent fixed-geometry radiators.

turndown ratio, the finite element model was executed again assuming the radiator remained in its initial, nearly-semicircular shape throughout the experiment. The heat rejection rate of this fixed-geometry (i.e. non-morphing) radiator is shown with the circular markers and dashed line in Fig. 5.2. Starting at approximately 30 min, the fixed-geometry radiator has a higher rate of heat rejection than the morphing radiator. The maximum heat rejection rate remains at 5.93 W, however, the minimum heat rejection rate increases 1.46 W, giving a turndown ratio of 4.1:1. These results show that the morphing behavior led to an increase of nearly 60% in the turndown ratio versus an equivalent fixed-geometry radiator panel.

5.2 Thermomechanically Coupled Finite Element Model

It is important to note that the preceding model was only intended to predict the thermal behavior of the morphing radiator prototype. In order to predict both the structural and thermal behavior, a fully-coupled model was developed in order to evaluate the physical accuracy of the analysis approach described in Chapter 3. Figure 5.3b shows the geometry of the corresponding finite element model which was developed for this evaluation study. The model includes each of the parts shown in Fig. 5.3a, with the exception of the flow tube, which was left out of the model. Rather than modeling each individual wire, the wires are homogenized into two "wire bundles" with a rectangular cross-section whose area is equal to the total cross-sectional area of five wires. Small regions near the ends of the wire are given elastic material properties to improve the stability of the numerical solution. The model takes advantage of the symmetry of the prototype in order to reduce the computational domain to one quarter of that shown in Fig. 5.3b. Table 5.1 gives the thermoelastic properties for the various materials used in the finite element model, while Table 4.1 gives additional parameters needed to define the constitutive behavior of the shape memory alloy wires. The goal of the model is to predict the evolution of both the temperature field and displacement field in the radiator when subjected to the conditions of the experiment. As described above, this requires a special analysis procedure that decouples the thermal and structural aspects of the problem into separate partitions which exchange data to capture the coupling.

The thermal partition is implemented using an uncoupled thermal analysis procedure in Abaqus. This procedure supports geometry-dependent radiation boundary conditions of the form in Eq. 2.14. The panel, spring, and terminal block are meshed using 4-node elements with temperature degrees of freedom (DS4 elements), while

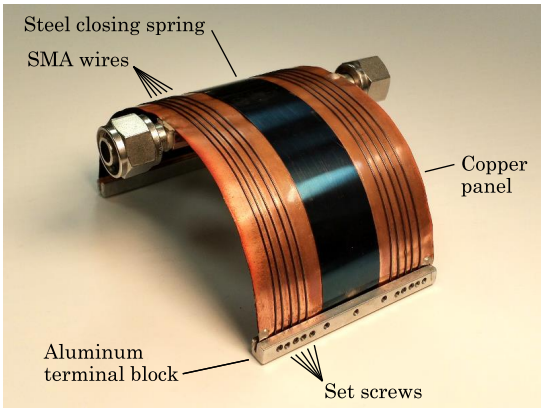

(a) Photograph of morphing radiator test specimen.

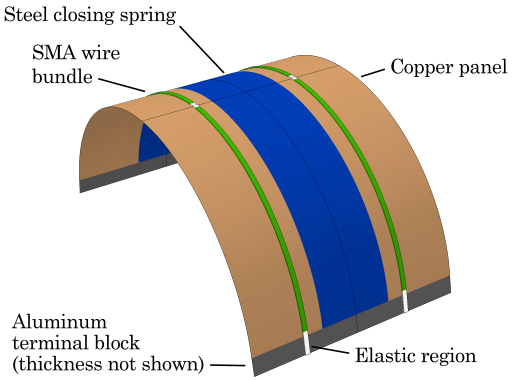

(b) Finite element model of morphing radiator prototype.

Figure 5.3: Morphing radiator test specimen and corresponding finite element model.

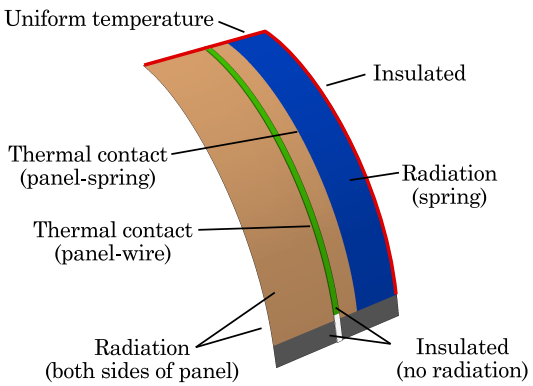

(a) Boundary conditions for thermal partition.

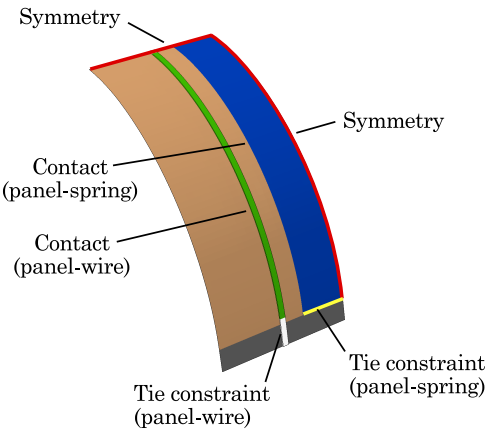

(b) Boundary conditions for structural partition.

Figure 5.4: Boundary conditions for the thermal and structural partitions.

Table 5.1: Thermoelastic properties for materials used in the thermomechanically coupled finite element model.

Material Property	**Aluminum**	**Copper**	**Steel**	**SMA**	**Elastic SMA**
E	70 GPa	110 GPa	200 GPa	54.6 GPa (E^A) 33.2 GPa (E^M)	54.6 GPa
ν	0.30	0.33	0.34	0.33	0.33
k	205 W/m·K	385 W/m·K	50 W/m·K	22 W/m·K	22 W/m·K
ρ	2700 kg/m^3	8960 kg/m^3	7850 kg/m^3	6450 kg/m^3	6450 kg/m^3
c_p	910 J/kg·K	390 J/kg·K	490 J/kg·K	329 J/kg·K	329 J/kg·K

the wire is meshed with 8-node elements (DS8 elements). Figure 5.4a shows the problem domain with the thermal boundary conditions superimposed. To capture the temperature change induced by varying the fluid temperature, a uniform temperature boundary condition is defined along the upper edge of the panel according to experimental data recorded by a thermocouple attached to the panel at this location. The other symmetric edge is given an insulated boundary condition. Two thermal contact conditions are included to allow the parts to exchange heat; the contact conditions assume zero thermal resistance between the parts. Radiation boundary conditions are included on both sides of the panel and the convex side of the spring; owing to their relatively small area, radiation is neglected from the wires and terminal block region.

The structural partition is responsible for solving for the time history of the displacement field and is implemented in Abaqus using a nonlinear implicit dynamic analysis procedure considering finite rotations. Figure 5.4b shows the boundary conditions for the structural partition. Symmetry boundary conditions are used along the edges of symmetry. Tie constraints are used to attach the wire and closing spring to the panel. In particular, the spring and wire are both tied to the panel at their ends to simulate the effect of the terminal blocks. The wire is not tied to the panel along its entire length; rather, a frictionless contact condition is prescribed between the wire and panel which prevents the nodes of the meshed wire from penetrating the surface of the panel. The spring and panel are meshed with 4-node reduced-integration shell elements (S4R elements), while the wire is meshed with 8-node fully-integrated brick elements (C3D8 elements). The constitutive behavior of the shape memory alloy is included via a user material subroutine (UMAT) in Abaqus which implements the constitutive model of Lagoudas et al. [35].

The two partitions are given identical meshes: the panel is meshed with 1416 4-node shell elements, the spring is meshed with 440 4-node reduced-integration

elements, and the wire bundle is meshed with 60 8-node fully-integrated solid elements. Although there is no fundamental requirement that the meshes be identical between the partitions, doing so simplifies the implementation, as there is no need to interpolate or extrapolate between dissimilar meshes.

As described above, in order to capture the effects of the coupling, there must be a means by which the partitions can exchange data as the simulation progresses. In particular, the thermal partition must be provided with the displacement from the previous increment (see Fig 3.1). This is accomplished using the *Import Part* feature in Abaqus, which allows the deformed geometry from one analysis to be imported into a new analysis. The temperature field from the previous increment is used as an initial condition and the uniform temperature and radiation boundary conditions are then applied to the imported geometry. Additionally, the structural partition must be provided with the current temperature field. In Abaqus, this can be accomplished using a *Predefined Field* which has an option to specify the temperature field using the results of a previous analysis. Due to the hysteretic behavior of shape memory alloy material [34], the structural partition must also be able to consider the full history of the displacement field. A feature known as a *restart analysis* in Abaqus is able to retain the state of the material, including stresses and internal state variables.

The partitions were integrated into the custom framework Python which is responsible for executing the partitions in an alternating series and passing the requisite field data between them. The framework was executed a total of 16 times, once for each of the entries in Table 5.2. The outcome of each analysis is indicated in the "Result" column. Only five runs completed successfully; during the remaining runs, the structural model failed to converge. Note that all of the analysis runs which used SMA Calibration 2 failed at approximately $t = 30\,\text{min}$.

Table 5.2: Summary of the individual analysis runs of the fully-coupled model. See Table 4.1 for the parameters corresponding to SMA Calibration 1 and 2.

ID	SMA Cal.	Thermal Response	Timestep	Result
1	1	Transient	30 min	Failed at $t = 150$ min
2	1	Transient	15 min	Failed at $t = 120$ min
3	1	Transient	10 min	Failed at $t = 100$ min
4	1	Transient	5 min	Completed
5	1	Quasi-steady state	30 min	Completed
6	1	Quasi-steady state	15 min	Completed
7	1	Quasi-steady state	10 min	Completed
8	1	Quasi-steady state	5 min	Completed
9	2	Transient	30 min	Failed at $t = 30$ min
10	2	Transient	15 min	Failed at $t = 30$ min
11	2	Transient	10 min	Failed at $t = 30$ min
12	2	Transient	5 min	Failed at $t = 30$ min
13	2	Quasi-steady state	30 min	Failed at $t = 30$ min
14	2	Quasi-steady state	15 min	Failed at $t = 30$ min
15	2	Quasi-steady state	10 min	Failed at $t = 30$ min
16	2	Quasi-steady state	5 min	Failed at $t = 25$ min

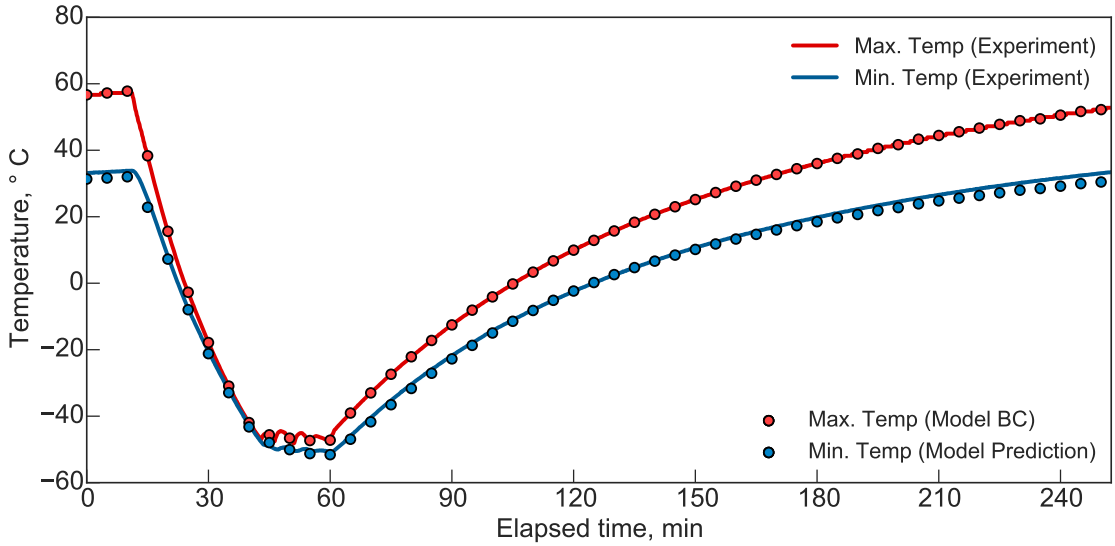

Figure 5.5: Comparison between panel temperatures measured during the experiment and computed via the fully-coupled model implemented using the analysis framework (Analysis 4).

Figure 5.5 shows the evolution of the minimum temperature as predicted by Analysis 4 along with the maximum and minimum temperatures recorded during the experiment; the solid lines are used to represent the experimental data, while the circles show the results from the finite element model. As described above, the maximum temperature from the experiment is used as a boundary condition in the finite element model. Therefore, the minimum panel temperature provides the primary comparison for the temperature field. Between $t = 0\,\text{min}$ and $t = 15\,\text{min}$, the temperature field matches very closely because there is no geometry change occurring during this period. The panel begins to close soon after the maximum temperature begins to decrease and continues to do so until the temperature reaches its minimum value at $t = 45\,\text{min}$. During this period, the model predictions match the experimental data closely, although the model predicts a slightly lower temperature

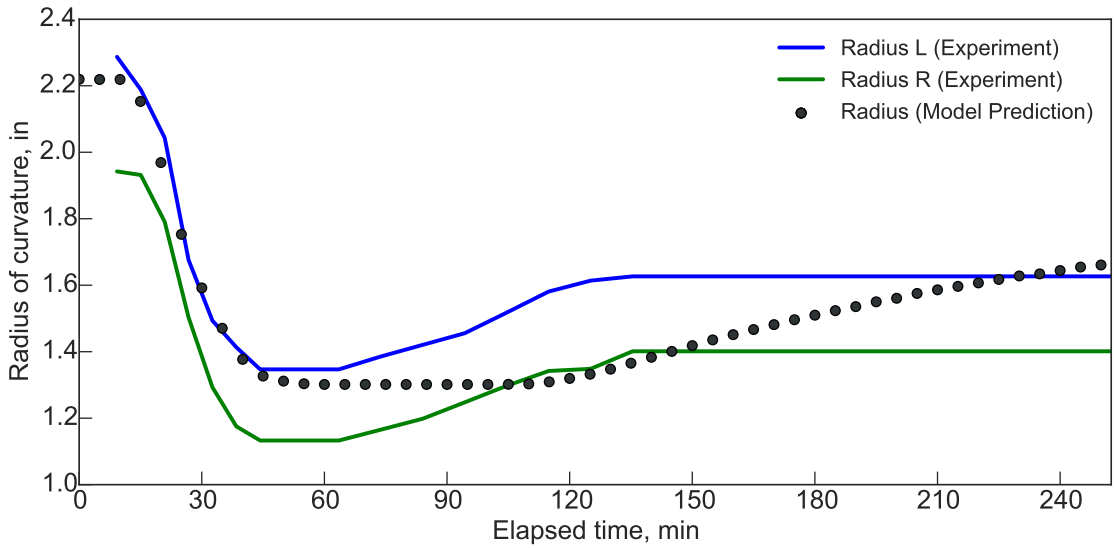

Figure 5.6: Comparison between panel radius of curvature measured during the experiment and computed via the fully-coupled model implemented using the analysis framework (Analysis 4).

than was recorded during the experiment. During the period between $t = 45\,\text{min}$ and $t = 60\,\text{min}$, the model does a very good job of predicting the temperature. During the remainder of the experiment, the radiator begins to warm up and begins to recover its initial shape in the process.

Figure 5.6 compares the radius of curvature from Analysis 4 to the experimental data; as before, solid lines represent the experimental data, while the model prediction is shown with circular markers. Up to $t = 60\,\text{min}$, the model predictions closely match the experimental data corresponding to the left side of the panel (recall that asymmetry in the panel meant that the left and right sides of the panel had different a different radius of curvature). In particular, the model is able to accurately predict the minimum radius of curvature between $t = 45$ and $t = 60\,\text{min}$. However, during the remainder of the simulation, there appears to be a significant lag in the model

predictions relative to the experimental data, i.e., the experimental radiator began to open soon after $t = 60\,\text{min}$, whereas the model predicted that the radiator stayed closed much longer, until $t = 130\,\text{min}$. In order to understand why this is the case, it is important to revisit Figs. 4.6b and 4.7b, which give the SMA constitutive model predictions of the isobaric response of the SMA wire used in the experiment. In particular, Fig. 4.6b gives the prediction corresponding to Calibration 1, which is the calibration that was used in Analysis 4. As described above, although Calibration 1 matches the transformation strain magnitude and transformation temperatures very closely, it is not able to predict the gradual strain recovery seen along the upper portion of each isobaric loop of the experimental data. This inability to capture gradual transformation is one of the primary shortcomings of the SMA constitutive model used in this work and is the is the primary source of the significant error seen in Fig. 5.6. Although Calibration 2 is able to better represent the behavior of the SMA wire (see Fig. 4.7b), each of the analyses that used Calibration 2 failed to converge (see Table 5.2). In spite of the significant transient error, the model matches the experimental data once again at the end of the experiment ($t = 250\,\text{min}$).

Figure 5.7 shows the evolution of the total heat rejection rate as predicted by Analysis 4. In addition, the heat rejection rate predicted by the uncoupled thermal model discussed in Section 5.1 is also plotted as the solid line labeled "Experiment." In spite of the discrepancies seen in the previous plot, the model appears to predict the heat rejection rate fairly closely. Note that the model slightly overpredicts the heat rejection rate, which is a consequence of the symmetry assumption used in the coupled model; in the physical prototype, the right side of the panel was slightly more closed than the left side, which results in a slightly lower heat rejection rate.

Figures 5.8 and 5.9 show the results from two of the other anlayses in Table 5.2. In particular, Fig. 5.8 presents the results of Analysis 3, which used a timestep of

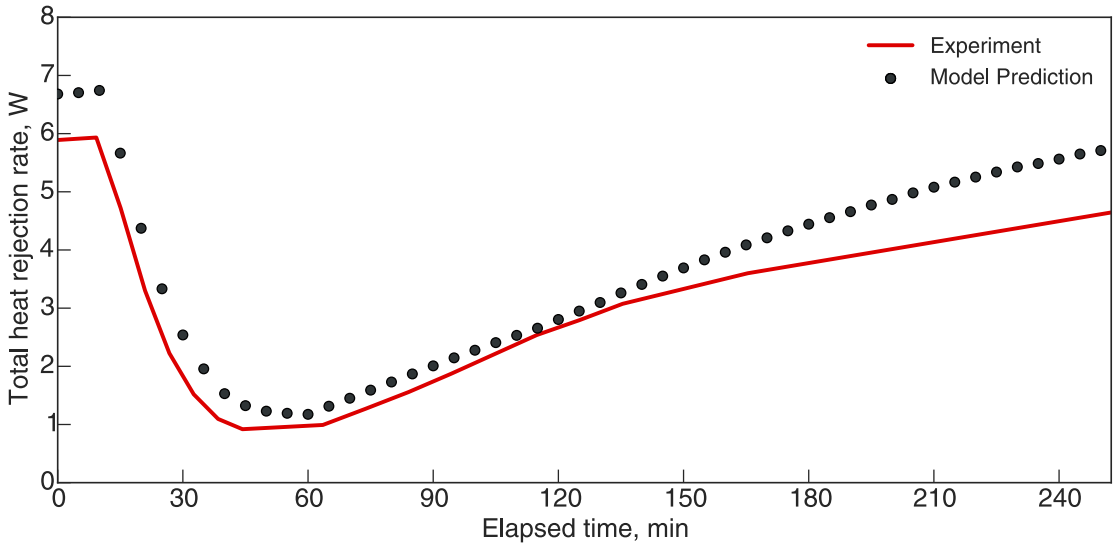

Figure 5.7: Comparison between panel heat rejection rate determined via the uncoupled model and computed via the fully-coupled model implemented using the analysis framework (Analysis 4).

10 min instead of 5 min. These results are notable because the model predictions of radius of curvature appear to match the experimental data much more closely than the predictions of Analysis 4 shown in Fig. 5.6. Unfortunately, the structural model failed to converge at $t = 100$. Figure 5.9 shows the results of Analysis 8, which used a timestep of 5 min (identical to Analysis 3), but assumed the thermal response was quasi-steady state instead of transient.

These results demonstrate the ability of the framework to predict the behavior of the prototype morphing radiator over the course of the experiment, giving confidence in the partitioned analysis procedure described in Chapter 3.

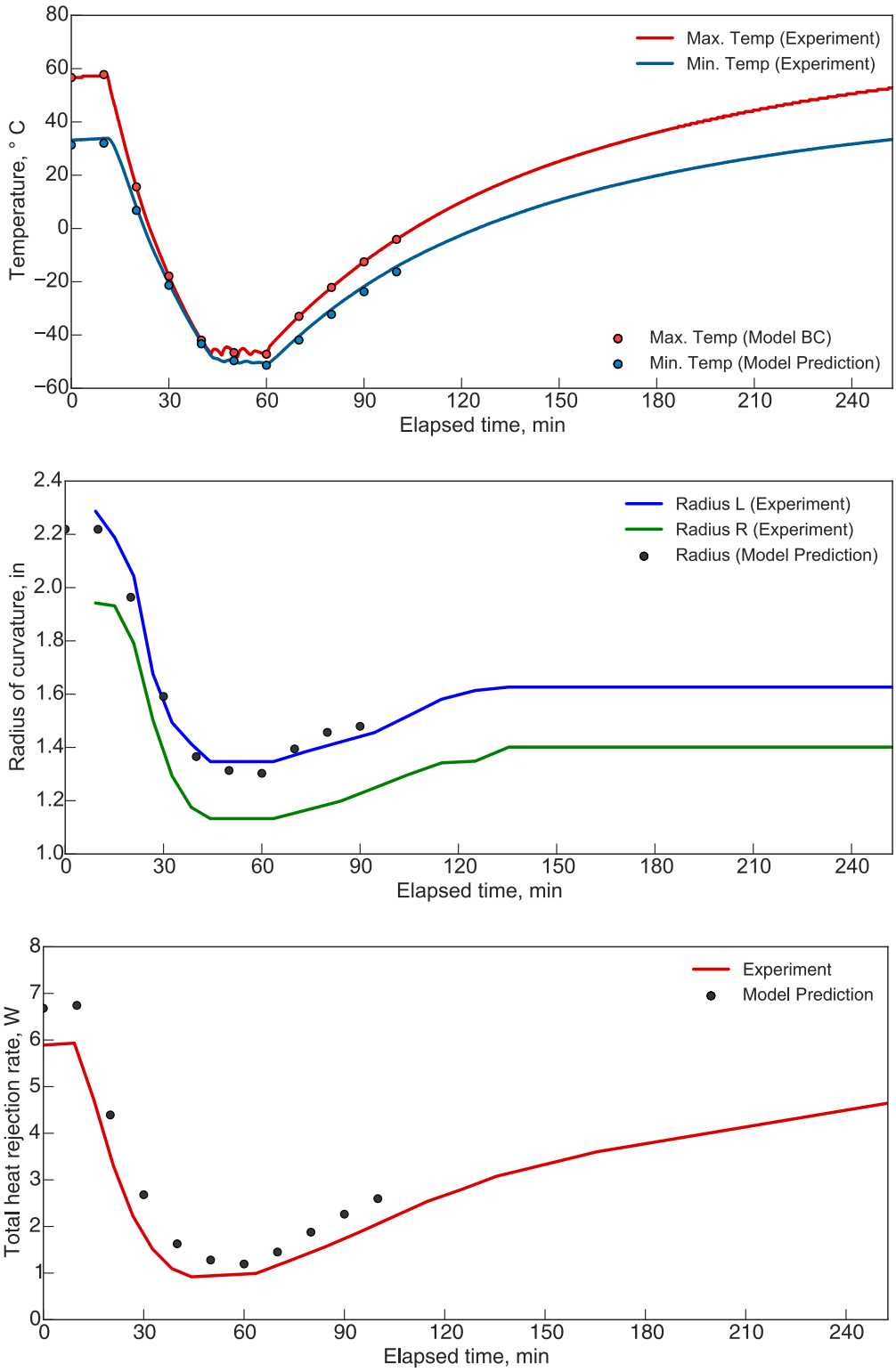

Figure 5.8: Temperature, radius of curvature, and heat rejection as computed via the fully-coupled model (Analysis 3).

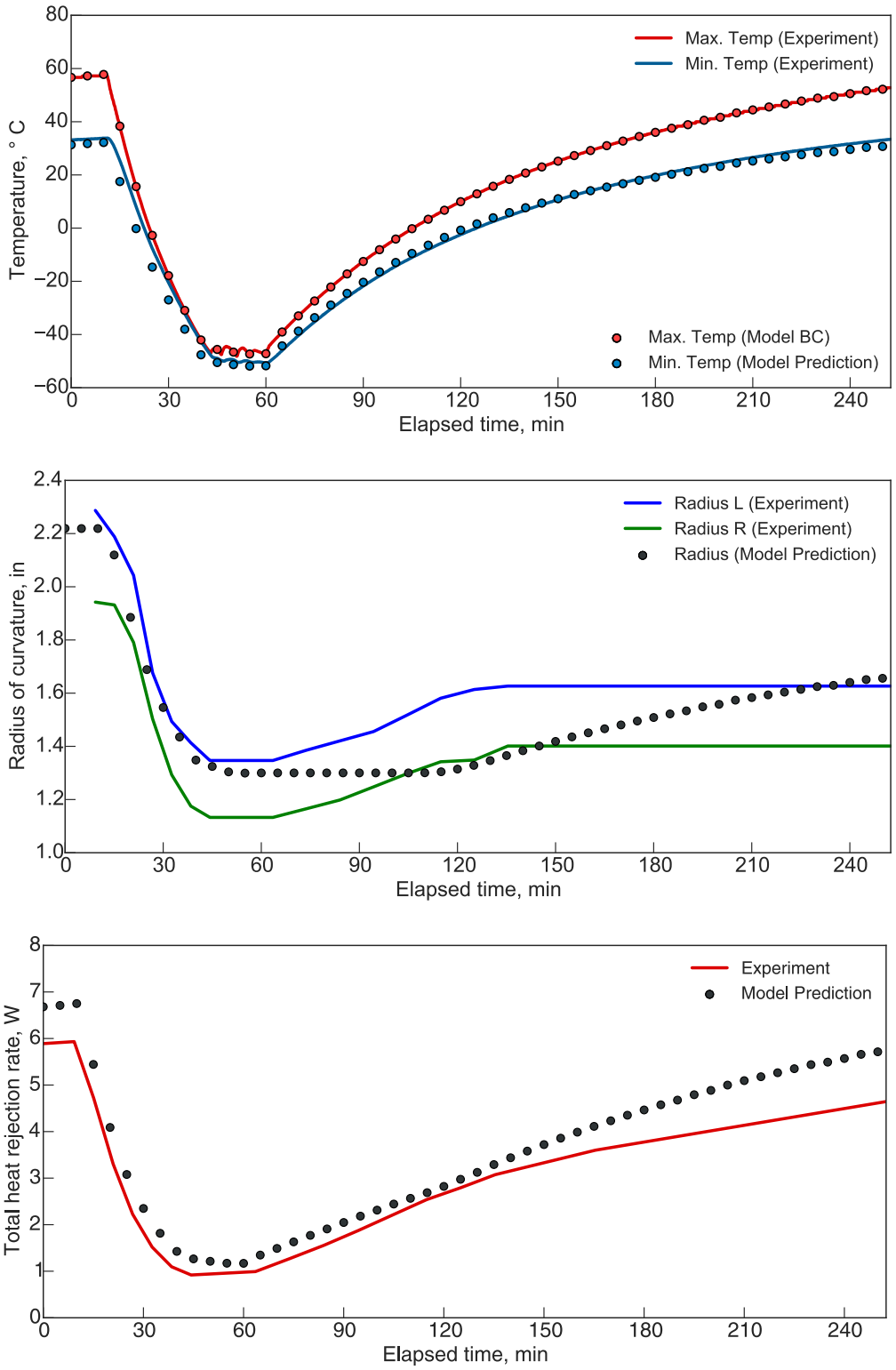

Figure 5.9: Temperature, radius of curvature, and heat rejection as computed via the fully-coupled model (Analysis 8).

6. CONCLUSIONS AND FUTURE WORK

As discussed previously, morphing radiators exhibit a unique type of thermomechanical coupling which most existing analysis tools are incapable of modeling. In order to overcome this present shortcoming, a multiphysics framework has been developed which allows general problems involving morphing radiators to be modeled using existing analysis tools. The framework relies on a technique known as a partitioned analysis procedure. Chapter 3 described the implementation of the partitioned approach in detail and presented the results from several example problems, which successfully demonstrated the ability of the approach to model complex and realistic problems involving morphing radiators. Following the initial development of the modeling framework, a morphing radiator prototype was designed, fabricated, and subsequently tested in a thermal vacuum chamber to simulate the thermal conditions which might be experienced by the radiator on a future mission. The test, discussed in detail in Chapter 4, successfully demonstrated the desired temperature-induced morphing behavior which drives the ability of the morphing radiator to vary its heat rejection. Chapter 5 described a detailed finite element model of the morphing radiator prototype which was developed and implemented in the analysis framework, allowing the physical accuracy of the framework to be evaluated. Some discrepancies were noted; however, these are primarily due to shortcomings in the ability of the SMA constitutive model to represent the behavior of the wire, rather than underlying errors in the framework itself.

By decoupling the problem into separate structural and thermal partitions, the shortcomings present in existing analysis tools are bypassed, allowing complex geometrically-dependent radiation boundary conditions to be considered along with the constitutive behavior of shape memory alloy material. This represents powerful

and novel analysis capability, as there is a present lack of software packages that can simulate this class of problem. Simulations such as those presented here will be essential in understanding the interaction of morphing radiators with the overall thermal control system in the full range of mission environments. Thus, this work represents an important step in the process of deploying morphing radiators in future space missions.

However, it is important to note that the present approach does have several fundamental limitations. Chief among these is the significant execution time required to simulate a problem using the framework, stemming from the inefficiencies inherent in the implementation. Most of the results presented required at least six hours of runtime on a desktop workstation; several of the more complex examples required over 24 hours. This severely restricts the utility of the framework, particularly during the early stages of the design process. Future work could address these shortcomings in order to increase the accuracy, efficiency, and overall utility of the framework. The serial execution method used in this work requires each analysis to wait for the preceding one to complete before it can access field data. Lower-level coupling mechanisms could provide direct access to the field data during execution, rather than only upon completion of the analysis. Alternate coupling methods could also be implemented which are able to achieve second-order time accuracy. This would allow larger time steps to be used, decreasing the total number of increments needed to simulate a given problem. Future efforts could also focus on implementing efficient and versatile reduced-order models which are able to execute in seconds, thereby expediting the early stages of the design process. Further, although not directly related to this work, improvements to the SMA constitutive model could be implemented to better capture the gradual transformation seen in the SMA wire used in the morphing radiator prototype.

REFERENCES

[1] E. T. Bannon, C. E. Bower, R. Sheth, R. Stephan, P. Chandrasekhar, and B. Zay. Electrochromic radiator coupon level testing and full scale thermal math modeling for use on altair lunar lander. In *40th International Conference on Environmental Systems*, page 6110, 2010.

[2] C. Bertagne, R. Sheth, D. Hartl, and J. D. Whitcomb. Simulating coupled thermal-mechanical interactions in morphing radiators. In *Proceedings of SPIE, Active and Passive Smart Structures and Integrated Systems*, volume 9431, pages 94312F–94312F–10, San Diego, CA, 9–12 March 2015.

[3] C. L. Bertagne, J. B. Chong, J. D. Whitcomb, D. J. Hartl, L. R. Erickson, and R. B. Sheth. Experimental characterization of a shape memory alloy-based morphing radiator. In *Proceedings of 24th AIAA/AHS Adaptive Structures Conference*, page 1568, San Diego, CA, 4–8 January 2016.

[4] J. G. Boyd and D. C. Lagoudas. A thermodynamical constitutive model for shape memory materials. Part I. The monolithic shape memory alloy. *International Journal of Plasticity*, 12(6):805–842, 1996.

[5] F. Calkins, G. Butler, and J. Mabe. Variable geometry chevrons for jet noise reduction. *Proceedings of the 27th Annual AIAA Aeroacoustics Conference*, pages 1–11, 8–10 May 2006.

[6] F. Calkins and J. Mabe. Shape memory alloy based morphing chevrons: full scale static engine test. In *Proceedings of the 28th Annual AIAA Aeroacoustics Conference*, number 3438 in AIAA 2007, pages 1–12, Rome, Italy, 21–23 May 2007.

[7] B. Carpenter and J. Lyons. EO-1 technology validation report: Lightweight flexible solar array experiment. Technical report, NASA Godard Space Flight Center, Greenbelt, MD, 8 August 2001.

[8] T. Cognata, D. Hartl, R. Sheth, and C. Dinsmore. A morphing radiator for high-turndown thermal control of crewed space exploration vehicles. In *Proceedings of 23rd AIAA/AHS Adaptive Structures Conference*, Kissimmee, FL, 2015.

[9] B. D. Coleman. Thermodynamics of materials with memory. *Archive for Rational Mechanics and Analysis*, 17:1–46, 1964.

[10] B. D. Coleman and M. E. Gurtin. Thermodynamics with internal state variables. *The Journal of Chemical Physics*, 47(2):597–613, July 1967.

[11] B. D. Coleman and W. Noll. Material symmetry and thermostatic inequalities in finite elastic deformations. *Archive for Rational Mechanics and Analysis*, 15:87–111, 1964.

[12] Dassault Systèmes of America Corp., Woodlands Hills, CA. *Abaqus Analysis User's Manual*, 2007.

[13] J. Degroote. Partitioned simulation of fluid-structure interaction. *Archives of Computational Methods in Engineering*, 20(3):185–238, 2013.

[14] A. Feingold. Radiant-interchange configuration factors between various selected plane surfaces. *Proceedings of the Royal Society of London. Series A. Mathematical and Physical Sciences*, 292(1428):51–60, 1966.

[15] C. A. Felippa, K. Park, and C. Farhat. Partitioned analysis of coupled mechanical systems. *Computer Methods in Applied Mechanics and Engineering*, 190(24):3247–3270, 2001.

[16] D. H. Friedman, S. Bieniawski, and D. Hartl. Simulation and control design for shape memory alloy torque tubes. In *ASME 2011 Conference on Smart Materials, Adaptive Structures and Intelligent Systems*, pages 303–313. American Society of Mechanical Engineers, 2011.

[17] G. B. Ganapathi, E. T. Sunada, G. C. Birur, J. R. Miller, and R. Stephan. Design description and initial characterization testing of an active heat rejection radiator with digital turn-down capability. Technical report, SAE Technical Paper, 2009.

[18] D. G. Gilmore. *Spacecraft Thermal Control Handbook: Fundamental Technologies*, volume 1. AIAA, Reston, VA, 2nd edition, 2003.

[19] O. Godard, M. Lagoudas, and D. Lagoudas. Design of space systems using shape memory alloys. In *Proceedings of SPIE, Smart Structures and Materials*, volume 5056, pages 545–558, San Diego, CA, 2–6 March 2003.

[20] M. E. Gurtin, E. Fried, and L. Anand. *The mechanics and thermodynamics of continua.* Cambridge University Press, New York, NY, 2010.

[21] D. C. Hamilton and W. R. Morgan. Radiant-interchange configuration factors. Technical Note NACA-TN-2836, National Advisory Committee for Aeronautics, 1952.

[22] D. Hartl and D. Lagoudas. Thermomechanical characterization of shape memory alloy materials. In D. Lagoudas, editor, *Shape Memory Alloys: Modeling and Engineering Applications.* Springer-Verlag, New York, NY, 2008.

[23] D. Hartl, D. Lagoudas, J. Mabe, F. Calkins, and J. Mooney. Use of Ni60Ti shape memory alloy for active jet engine chevron application, Part II: Experimentally

validated numerical analysis. *Smart Materials and Structures*, 19(1):015021, 2009.

[24] D. J. Hartl and D. Lagoudas. Aerospace applications of shape memory alloys. *Proceedings of the Institution of Mechanical Engineers, Part G: Journal of Aerospace Engineering*, 221 (Special Issue):535–552, 2007.

[25] D. J. Hartl, A. Solomou, D. C. Lagoudas, and D. Saravanos. Phenomenological modeling of induced transformation anisotropy in shape memory alloy actuators. *SPIE Smart Structures and Materials+ Nondestructive Evaluation and Health Monitoring*, pages 83421M–83421M, 2012.

[26] J. Herrington, L. Hodge, C. Stein, Y. Babbar, R. Saunders, D. Hartl, and J. Mabe. Development of a twisting wing powered by a shape memory alloy actuator. *AIAA SciTech, American Institute of Aeronautics and Astronautics Inc*, 2015.

[27] S. A. Hill, C. Kostyk, B. Motil, W. Notardonato, S. Rickman, and T. Swanson. Thermal Management Systems Roadmap: Technology Area 14. Technical report, NASA, July 2015.

[28] G. Hou, J. Wang, and A. Layton. Numerical methods for fluid-structure interaction—a review. *Commun. Comput. Phys*, 12(2):337–377, 2012.

[29] J. R. Howell, R. Siegel, and M. P. Menguc. *Radiation Heat Transfer*. CRC Press, Boca Raton, FL, 5th edition, 2011.

[30] J. M. Jani, M. Leary, A. Subic, and M. A. Gibson. A review of shape memory alloy research, applications and opportunities. *Materials & Design*, 56:1078–1113, 2014.

[31] H. R. N. Jones. *Radiation heat transfer*, volume 89. Oxford University Press, Oxford, United Kingdom, 2000.

[32] W. Joppich and M. Kürschner. Mpcci—a tool for the simulation of coupled applications. *Concurrency and computation: Practice and Experience*, 18(2):183–192, 2006.

[33] A. J. Juhasz and G. P. Peterson. Review of advanced radiator technologies for spacecraft power systems and space thermal control. *NASA STI/Recon Technical Report N*, 94, 1994.

[34] D. Lagoudas, editor. *Shape Memory Alloys: Modeling and Engineering Applications.* Springer-Verlag, New York, NY, 2008.

[35] D. Lagoudas, D. Hartl, Y. Chemisky, L. Machado, and P. Popov. Constitutive model for the numerical analysis of phase transformation in polycrystalline shape memory alloys. *International Journal of Plasticity*, 32–33:155–183, 2012.

[36] D. C. Lagoudas, Z. Bo, and M. A. Qidwai. A unified thermodynamic constitutive model for SMA and finite element analysis of active metal matrix composites. *Mechanics of Composite Materials and Structures*, 3:153–179, 1996.

[37] D. C. Lagoudas, P. B. Entchev, P. Popov, E. Patoor, L. C. Brinson, and X. Gao. Shape memory alloys, Part II: Modeling of polycrystals. *Mechanics of Materials*, 38(5–6):430–462, 2006.

[38] W. M. Lai, D. H. Rubin, D. Rubin, and E. Krempl. *Introduction to continuum mechanics.* Butterworth-Heinemann, Burlington, MA, 4th edition, 2009.

[39] J. Mabe, B. Fischer, and D. Hartl. Characterization and modeling of trained nitinol torsional actuators under reverse bias loads. *TMS2013 Supplemental Proceedings*, pages 987–998, 2013.

[40] J. H. Mabe, F. Calkins, and G. Butler. Boeing's variable geometry chevron, morphing aerostructure for jet noise reduction. In *47th AIAA/ ASME / ASCE / AHS / ASC Structures, Structural Dynamics and Materials Conference*, pages 1–19, Newport, Rhode Island, 1–4 May 2006.

[41] L. Machado and D. Lagoudas. Thermomechanical constitutive modeling of SMAs. In D. Lagoudas, editor, *Shape Memory Alloys: Modeling and Engineering Applications*, chapter 3, pages 122–187. Springer-Verlag, New York, 2008.

[42] J. Miller, G. Birur, G. Ganapathi, E. Sunada, D. Berisford, and R. Stephan. Design and testing of an active heat rejection radiator with digital turn-down capability. In *41st International Conference on Environmental Systems*. AIAA, July 2010.

[43] M. F. Modest. *Radiative Heat Transfer*. McGraw-Hill, New York, 1993.

[44] MSC Software, Newport Beach, CA. *MSC Nastran Thermal Guide*.

[45] NASA's journey to mars: Pioneering next steps in space exploration. Technical report, NASA, October 2015.

[46] NASA. TA 14: Thermal management systems. In *NASA Technology Roadmaps*. July 2015.

[47] R. Naumann. Optimizing the design of space radiators. *International Journal of Thermophysics*, 25(6):1929–1941, 2004.

[48] G. Nellis and S. Klein. *Heat Transfer*. Cambridge University Press, New York, NY, 2009.

[49] D. A. Ochoa, W. Vonau, and M. K. Ewert. A comparison between one- and two-loop ATCS architectures proposed for CEV. Technical report, SAE Technical Paper, 2009.

[50] K. Otsuka and C. M. Wayman, editors. *Shape Memory Materials.* Cambridge University Press, Cambridge, 1999.

[51] M. N. Ozisik. *Heat conduction.* John Wiley & Sons, New York, NY, 1993.

[52] A. Paivia and M. Savi. An overview of constitutive models for shape memory alloys. *Mathematical Problems in Engineering*, 2006:1–30, 2006.

[53] K. Park. Partitioned transient analysis procedures for coupled-field problems: stability analysis. *Journal of Applied Mechanics*, 47(2):370–376, 1980.

[54] E. Patoor, D. C. Lagoudas, P. B. Entchev, L. C. Brinson, and X. Gao. Shape memory alloys, Part I: General properties and modeling of single crystals. *Mechanics of Materials*, 38(5–6):391–429, 2006.

[55] R. Ponnappan, J. Beam, and E. Mahefkey. Conceptual design of an 1 m long 'roll out fin' type expandable space radiator. *Rep./AIAA*, 1984.

[56] N. Ramesh, C. Balaji, and S. Venkateshan. Numerical analysis of a cavity radiator with mutual interaction. *Applied Mathematical Modelling*, 20(6):476 – 484, 1996.

[57] J. N. Reddy. *An Introduction to Nonlinear Finite Element Analysis: with applications to heat transfer, fluid mechanics, and solid mechanics.* Oxford University Press, Oxford, United Kingdom, 2nd edition, 2014.

[58] W. M. Rohsenow, J. P. Hartnett, Y. I. Cho, et al. *Handbook of heat transfer.* McGraw-Hill, New York, NY, 3rd edition, 1998.

[59] R. N. Saunders, D. J. Hartl, J. G. Boyd, and D. C. Lagoudas. Modeling and development of a twisting wing using inductively heated shape memory alloy actuators. In *SPIE Smart Structures and Materials+ Nondestructive Evaluation*

and Health Monitoring, pages 94310U–94310U. International Society for Optics and Photonics, 2015.

[60] R. A. Stephan. Overview of NASA's thermal control system development for exploration project. *SAE ICES*, 2009.

[61] R. J. Stephenson, A. M. Moulin, M. E. Welland, J. Burns, M. Sapoff, R. P. Reed, R. Frank, J. Fraden, J. V. Nicholas, F. Pavese, J. Stasiek, T. Madaj, J. Mikielewicz, and B. Culshaw. Temperature measurement. In J. G. Webster, editor, *The Measurement, Instrumentation, and Sensors: Handbook*, chapter 32. CRC Press, Boca Raton, FL, 1999.

[62] Swanson Analysis Systems, Inc, Houston, PA. *ANSYS Engineering Analysis System Users Manual.*

[63] S. Timoshenko. Analysis of bi-metal thermostats. *JOSA*, 11(3):233–255, 1925.

[64] T. L. Turner, R. T. Kidd, D. J. Hartl, and W. D. Scholten. Development of a SMA-based, slat-cove filler for reduction of aeroacoustic noise associated with transport-class aircraft wings. In *ASME 2013 Conference on Smart Materials, Adaptive Structures and Intelligent Systems.* American Society of Mechanical Engineers, 2013.

[65] T. L. Turner and D. L. Long. Development of a sma-based, slat-gap filler for airframe noise reduction. In *Proceedings of 23rd AIAA/AHS Adaptive Structures Conference*, Kissimmee, FL, 5–9 January 2015.

[66] N. Viswanatha and T. Murali. A novel mechanism using shape memory alloy to drive solar flaps of the insat-2e satellite. In *Proceedings of the 34th Aerospace Mechanisms Symposium*, pages 241–251, 2000.

[67] G. N. Walton. *Calculation of Obstructed View Factors by Adaptive Integration.* NISTIR 6925. U.S. Department of Commerce, Technology Administration, National Institute of Standards and Technology, 2002.

[68] J. R. Wertz and W. J. Larson. *Space Mission Analysis and Design.* Microcosm Press, El Segundo, CA, 1999.

[69] R. Wheeler, R. Saunders, K. Pickett, C. Eckert, H. Stroud, T. Fink, K. Gakhar, J. Boyd, and D. Lagoudas. Design of a reconfigurable sma-based solar array deployment mechanism. In *ASME 2015 Conference on Smart Materials, Adaptive Structures and Intelligent Systems*, pages V001T02A010–V001T02A010. American Society of Mechanical Engineers, 2015.

[70] R. Zwaan and B. Prananta. Fluid/structure interaction in numerical aeroelastic simulation. *International Journal of Non-Linear Mechanics*, 37(4):987–1002, 2002.

APPENDIX A

A COMPARISON BETWEEN THERMOELASTIC AND SHAPE MEMORY ALLOY BI-MATERIAL ACTUATORS

Most materials expand or contract when subjected to changes in temperature. This behavior can be employed to create a *bi-material strip*, a device which uses differences in the thermal expansion coefficient of two materials to induce bending in response to temperature change. A typical bi-material strip consists of two strips of material with dissimilar thermal expansion coefficients that are bonded together along their length. Upon an increase in temperature, the two materials expand by different amounts, thereby causing the strip to bend in the direction transverse to the bond line. Thus, differential thermal expansion offers a potential alternative means of morphing a radiator panel in place of shape memory alloys. This appendix presents a first-order comparison between these two actuation methods.

Consider an initially curved radiator panel whose cross-section is a circular arc of radius r_0 at temperature T_0, as shown in Fig. A.1a. The primary goal of this study is to design the panel such that it is deforms to a more open configuration with $r > r_0$ as shown in Fig. A.1b upon an increase in temperature ($T > T_0$) and in the absence of externally applied forces. To do this, we will assume that the panel is a bi-material strip where Material 1 is defined to be the material on the inner (i.e., concave) side of the panel and Material 2 is defined to be the material on the outer (i.e., convex) side of the panel (see Fig. A.2).

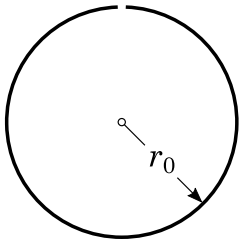

(a) Reference configuration with radius of curvature r_0 at temperature T_0.

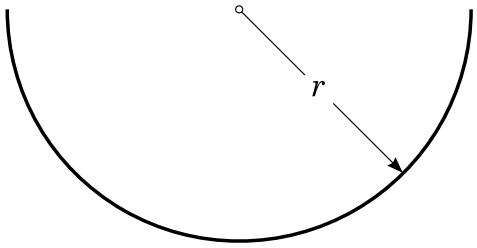

(b) Deformed configuration with radius of curvature $r > r_0$ at temperature $T > T_0$.

Figure A.1: Reference and deformed configurations of a morphing radiator panel.

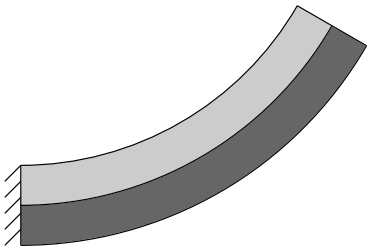

(a) Reference configuration with radius of curvature r_0.

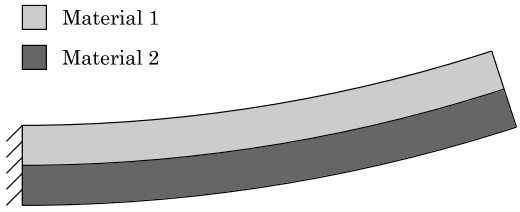

(b) Deformed configuration with radius of curvature $r > r_0$.

Figure A.2: Reference and deformed configurations of a bi-material strip used to actuate a morphing radiator panel.

To begin, consider the general equation governing the change in curvature of a bi-material strip in the absence of external forces, which is given by [61, 63]

$$\Delta\kappa = \frac{1}{r} - \frac{1}{r_0} = \frac{6(1+m)^2\Delta\varepsilon}{t\left[3\left(1+m\right)^2 + \left(1+mn\right)\left(m^2 + \frac{1}{mn}\right)\right]}, \tag{A.1}$$

where $n = E_2/E_1$ is the ratio between the extensional stiffnesses of the two materials, $m = t_2/t_1$ is the ratio between the thicknesses of the two strips, $t = t_1 + t_2$ is the overall thickness of the composite strip, and $\Delta\varepsilon = \varepsilon_2 - \varepsilon_1$ is the *differential strain.* In this case, $r > r_0 \iff \Delta\kappa < 0$, which implies that $\Delta\varepsilon < 0 \iff \varepsilon_1 > \varepsilon_2$. In other words, Material 2 must expand less than Material 1 in order for the bi-material strip to open the panel. To simplify the discussion, we will define a nondimensional parameter ζ by

$$\zeta = \frac{6(1+m)^2}{3\left(1+m\right)^2 + \left(1+mn\right)\left(m^2 + \frac{1}{mn}\right)}, \tag{A.2}$$

which allows Eq. A.1 to be written as

$$\Delta\kappa = \frac{\zeta\Delta\varepsilon}{t}. \tag{A.3}$$

Rearranging this expression to solve for the overall thickness of the panel gives

$$t = \frac{\zeta\Delta\varepsilon}{\Delta\kappa}. \tag{A.4}$$

In order to design the most thermally-efficient radiator panel, we wish to maximize the overall thickness (t) for a given change in curvature ($\Delta\kappa$). Therefore, in Eq. A.4, we will treat $\Delta\kappa$ as a known constant and ζ and $\Delta\varepsilon$ as design variables. It can be shown that the maximum value of ζ is $1/4$. Furthermore, it can also be shown that for every value of $n > 0$, there is a particular value of m for which $\zeta = 1/4$. Thus, for

this first-order investigation, we will simply assume that m is chosen in this manner such that we can substitute $\zeta = 1/4$ into Eq. A.4, giving

$$t_{max} = \frac{\Delta\varepsilon}{4\Delta\kappa}. \tag{A.5}$$

Clearly, in order to maximize the thickness of the panel, we must maximize the differential strain. We begin by assuming both Material 1 and Material 2 are thermoelastic. In this case, the differential strain is given by

$$\Delta\varepsilon = (\alpha_2 - \alpha_1)\Delta T. \tag{A.6}$$

If we assume a fairly generous ΔT of 100°C and choose aluminum for Material 1 ($\alpha_1 = 22.2 \cdot 10^{-6}$ °C^{-1}) and copper for Material 2 ($\alpha_2 = 16.6 \cdot 10^{-6}$ °C^{-1}), we compute

$$\Delta\varepsilon_{thermoelastic} = -0.56\%. \tag{A.7}$$

If we now replace Material 2 with a shape memory alloy which has an initial transformation strain of ε^t in the reference configuration, the differential strain is given by

$$\Delta\varepsilon = (\alpha_2 - \alpha_1)\Delta T - \varepsilon^t \approx -\varepsilon^t. \tag{A.8}$$

For many shape memory alloys, the maximum transformation strain is approximately 5% [34], thus

$$\Delta\varepsilon_{SMA} = -5\%. \tag{A.9}$$

Comparing Eqs. A.7 and A.9, we see that the shape memory alloy bi-material strip is able to achieve a differential strain magnitude approximately two orders of magnitude higher than an equivalent bi-material strip composed of two thermoelastic materials.

Consequently, the panel which uses shape memory alloys is able to be approximately two orders of magnitude thicker than the thermoelastic panel for a given change in curvature.

APPENDIX B

NUMERICAL VERIFICATION OF THE HEAT TRANSFER ANALYSIS PROCEDURE USING RADIATION BOUNDARY CONDITIONS IN ABAQUS

This verification study considers a pair of radiator panels which are attached to a pipe containing a cooling fluid. Figure B.1a shows a schematic diagram of the radiator assembly under consideration. The assembly consists of two panels which share a common edge along $x = 0$ and are separated by an angle of 90°. Each panel has length a and width b. The thickness of the panels is denoted by t. Coolant fluid is assumed to be passing through the small gap shown in the lower-left of Fig. B.1a. The shaded surfaces are painted with a high-emissivity paint, and therefore are radiating surfaces; all other surfaces, as well as the $-z$ face of Panel 1 and the $-y$ face of Panel 2 are assumed to be insulated. The panels are composed of an isotropic material with thermal conductivity k.

The temperature variation through the thickness can be neglected by assuming that the thickness of the panels is small relative to their width and height and that the thermal conductivity is sufficiently high. This allows the panels to be represented as a pair of rectangular surfaces, as shown in Fig. B.1b. The thermal boundary conditions are also shown in this figure. The effect of the coolant is modeled by specifying the temperature ($T = T_c$) of both panels along the common edge[1]; this is shown with a red line. All remaining edges are insulated, which is shown with the blue lines. As described above, the $+z$ face on Panel 1 and the $+y$ face of Panel 2 are radiating surfaces, while the $-z$ face of Panel 1 and the $-y$ face of Panel 2 are assumed to be insulated. The radiator assembly is surrounded by a nonparticipating

[1] A convection boundary condition would be more suitable to model the behavior of the fluid; however, the constant-temperature boundary condition was chosen to simplify the problem.

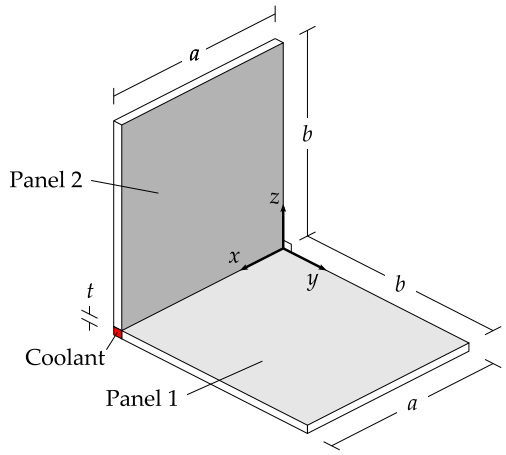

(a) Three-dimensional radiator geometry.

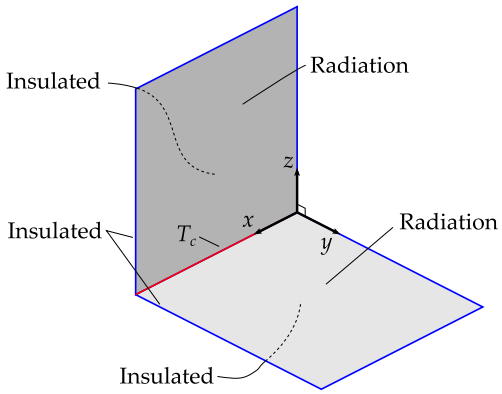

(b) Two-dimensional domain with thermal boundary conditions.

Figure B.1: Schematic diagrams depicting radiator geometry and thermal boundary conditions.

vacuum which is at temperature T_∞. The two panels share identical geometry and boundary conditions. Therefore, it is only necessary to model a single panel, as the radiation exchange between the two panels can be taken into account without the need to mesh both panels.

The goal is to predict the steady-state thermal behavior of the radiator panels considering the effects of conduction and grey-body radiation. The primary quantities of interest for this problem are the minimum radiator temperature, the minimum and maximum radiation heat flux, and the total heat rejected by both panels.

The values for the selected geometric and material parameters are given in Table B.1. The problem will be solved for multiple values of emissivity in the range 0.1-1.0 to determine the effect of surface coating on the performance of the radiator.

The radiation boundary condition adds significant complexity to the problem because of the nature of radiation heat transfer. A detailed description of the black-

Table B.1: Values for problem parameters.

Param.	Value
a	1.0 m
b	1.0 m
t	5.0 cm
k	167 W/m·K
ϵ	0.1-1.0
T_c	310 K
T_∞	50 K

and grey-body radiation theories is beyond the scope of this Appendix; however, a brief summary of the important details will be presented. The following discussion is based on the texts of Howell & Siegel [29] and Nellis & Klein [48].

In a conduction-convection problem, a given element can only exchange heat with its immediate neighbors via conduction and with the surroundings via convection. In a general radiation problem, any given element exchanges heat via radiation with every other element in the mesh as well as with the surroundings. Consider two arbitrary elements: element Ω_i at temperature T_i and element Ω_j at temperature T_j. Assuming black-body radiation ($\epsilon = 1$), the net rate of heat transfer from Ω_i to Ω_j by radiation (denoted as $Q^b_{i\to j}$) is given by

$$\dot{Q}^b_{i-j} = \sigma A_i F_{i-j}(T_i^4 - T_j^4), \tag{B.1}$$

where σ is the Stefan-Boltzmann constant (in SI units, $\sigma = 5.67\text{E-}8$ W/m^{2}K^4), and A_i is the area of Ω_i. The term $F_{i\to j}$ is known as the *view factor*. The view factor is defined as the fraction of radiation emitted by Ω_i that goes directly to Ω_j and is a function of the geometric configurations of both surfaces. The view factor between any

two surfaces must lie between zero and unity. The next section gives the expressions used to compute the view factors for this problem.

For grey-body radiation ($\epsilon < 1$), the equation is modified by using the *transfer factor* (denoted as $\mathscr{F}_{i-j}$) in place of the view factor:

$$\dot{Q}^{g}_{i\to j} = \sigma A_i \mathscr{F}_{i\to j}(T_i^4 - T_j^4) \tag{B.2}$$

The transfer factor is analogous to the view factor in Eq. B.1, except that the transfer factor accounts for the fact that the emissivity of the two surfaces is less than unity. If all surfaces are black, Eq. B.2 reduces to Eq. B.1 as $\mathscr{F}_{i\to j} = F_{i\to j}$ in this case. Recall from Sec. 2.1 that the transfer factors $\mathscr{F}_{i\to j}$ can be determined from the view factors $F_{i\to j}$ by first computing a set of intermediate parameters, known as the $\hat{F}_{i\to j}$ parameters [48]:

$$\hat{F}_{i-j} = F_{i-j} + \sum_{k=1}^{N}(1-\epsilon_k)F_{i-k}\hat{F}_{k-j} \qquad \text{for} \quad i,j = 1,2,...,N. \tag{B.3}$$

Once the $\hat{F}$ parameters have been computed, the transfer factors can be computed by

$$\mathscr{F}_{i-j} = \epsilon_i \epsilon_j \hat{F}_{i-j}. \tag{B.4}$$

Assuming the temperatures of each element are specified and the view factors/transfer factors have been computed, the net heat transfer rate from Element i can be determined with the following expressions[2]:

$$\dot{Q}_i^{net,b} = \sum_{j=1}^{N_s} \dot{Q}^{b}_{i-j} = \sigma A_i \sum_{j=1}^{N_s} F_{i-j}(T_i^4 - T_j^4). \tag{B.5}$$

[2]The surroundings can be treated as an additional surface, therefore, $N_s = N + 1$, where N is the number of elements.

$$\dot{Q}_i^{net,g} = \sum_{j=1}^{N_s} \dot{Q}_{i-j}^{g} = \sigma A_i \sum_{j=1}^{N_s} \mathscr{F}_{i-j}(T_i^4 - T_j^4). \tag{B.6}$$

Note that the above equations are expressed in terms of the element temperature, denoted by T. This is because black- and grey-body radiation theory assume that each surface is isothermal, which is not generally the case for a finite element. However, provided the temperature variation over a given element is relatively small, the element can be treated as isothermal for the radiation calculations. For this project, the element temperature (T_i) is defined to be the temperature at the center of the element. This can be interpolated from the nodal temperatures (u_n) and the interpolation functions ψ_n evaluated at $(\xi, \eta) = (0, 0)$ as

$$T_i = \sum_{n=1}^{N_n} u_n \psi_n(0,0), \tag{B.7}$$

where N_n denotes the number of nodes in the element.

For this problem, an analytical expression for the view factor between two arbitrary rectangular panels lying in perpendicular planes (Fig. B.2a) is given in Modest [43]:

$$\begin{aligned} 2A_i F_{i\to j} = \; & f(y_2,z_2,x_3) - f(y_2,z_1,x_3) - f(y_1,z_2,x_3) + f(y_1,z_1,x_3) \\ & + f(y_1,z_2,x_2) - f(y_1,z_1,x_2) - f(y_2,z_2,x_2) + f(y_2,z_1,x_2) \\ & - f(y_2,z_2,x_3-x_1) + f(y_2,z_1,x_3-x_1) + f(y_1,z_2,x_3-x_1) \\ & - f(y_1,z_1,x_3-x_1) + f(y_2,z_2,x_2-x_1) - f(y_2,z_1,x_2-x_1) \\ & - f(y_1,z_2,x_2-x_1) + f(y_1,z_1,x_2-x_1). \end{aligned} \tag{B.8}$$

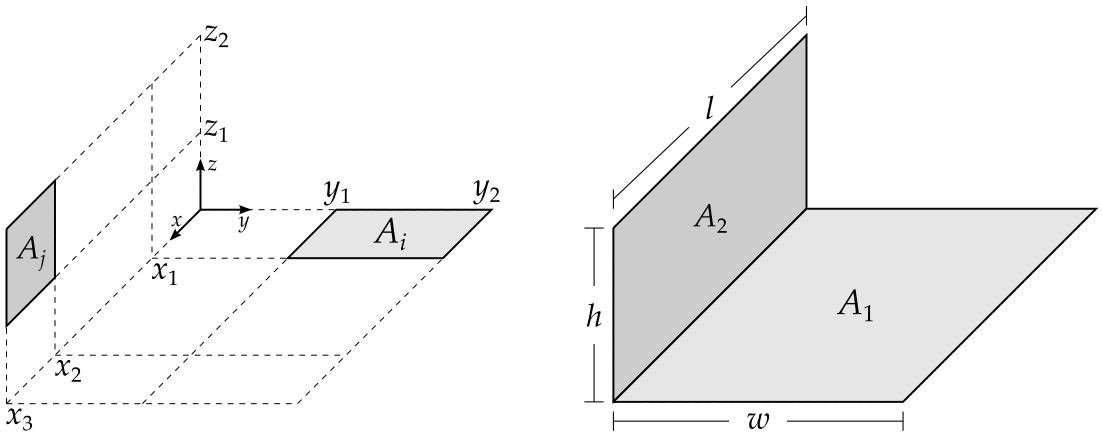

(a) General configuration. $F_{i\to j}$ is defined in Eq. B.8 in terms of $F^{39}_{1\to 2}$.

(b) Configuration 39. $F^{39}_{1\to 2}$ is defined in Eq. B.9.

Figure B.2: Schematics of geometry used in view factor expressions.

In this expression, $f = F^{39}_{1\to 2}$, which is the view factor between perpendicular rectangles of the same length, sharing a common edge, and separated by an angle of 90°:

$$F^{39}_{1\to 2}(w,h,l) = \frac{1}{\pi W}\left(W\tan^{-1}\frac{1}{W} + H\tan^{-1}\frac{1}{H} - \sqrt{H^2+W^2}\tan^{-1}\frac{1}{\sqrt{H^2+W^2}} + \frac{1}{4}\ln\left\{\frac{(1+W^2)(1+H^2)}{1+W^2+H^2}\left[\frac{W^2(1+H^2+W^2)}{(1+W^2)(H^2+W^2)}\right]^{W^2}\left[\frac{H^2(1+H^2+W^2)}{(1+H^2)(H^2+W^2)}\right]^{H^2}\right\}\right), \tag{B.9}$$

with the following definitions for H and W:

$$H = h/l,$$

$$W = w/l.$$

For a problem with N_s radiating surfaces[3], there will be a total of N_s^2 view factors. It is convenient to store the view factors in a matrix. In general, the view factor matrix is not symmetric, as $F_{i \to j} \neq F_{j \to i}$ in general.

The most straightforward way to implement this problem is to treat it as a two-dimensional conduction problem with a special type of boundary condition. This approach builds upon the two-dimensional heat transfer finite element model developed by Reddy [57]. The details of the conduction model are discussed at length in this textbook and will be not presented here, as the stiffness matrix and load vector remain unchanged. The matrix representation of the finite-element model for two-dimensional conduction is given by

$$[\mathbf{K}(\mathbf{U})]\{\mathbf{U}\} = \{\mathbf{F}\}, \tag{B.10}$$

where $\mathbf{K}$ is the assembled coefficient matrix, $\mathbf{U}$ is the vector of nodal temperatures to be determined, and $\mathbf{F}$ is the assembled source vector. This model can be extended by adding an additional vector to the right side of the equation, which represents the nodal contributions from the radiation boundary condition:

$$[\mathbf{K}(\mathbf{U})]\{\mathbf{U}\} = \{\mathbf{F}\} + \{\mathbf{G}\}. \tag{B.11}$$

The primary challenge is that the radiation calculations described in the previous section are expressed in terms of element quantities, whereas Eq. B.11 is written in terms of nodal quantities. However, it is straightforward to transform between the two representations. Consider an element Ω_i. The element temperature (T_i) was

[3]The surroundings can be treated as an additional surface, therefore, $N_s = N + 1$, where N is the number of elements.

defined above as the interpolated temperature at the center of the element:

$$T_i = \sum_{n=1}^{N_n} u_n \psi_n(0,0), \tag{B.12}$$

where N_n denotes the number of nodes in the element. This is done for each element in the mesh. Next, Eq. B.6 is used to compute the net rate of heat transfer from Ω_i. Finally, this load is distributed evenly among the nodes in the element:

$$\{G_i\}_n = \frac{\dot{Q}_i^{net}}{N_n}, n = 1, ..., N_n \tag{B.13}$$

where the subscript n denotes the local node number. It is a simple task to transform from the local node numbering to the global node numbering in order to add the contributions to the global $\mathbf{G}$ vector. Clearly, this vector depends on all the nodal temperatures. Thus, Eq. B.11 can be understood in the following manner:

$$[\mathbf{K}(\mathbf{U})]\{\mathbf{U}\} = \{\mathbf{F}\} + \{\mathbf{G}(\mathbf{U})\}. \tag{B.14}$$

This expression differs from Eq. B.10 because $\mathbf{U}$ appears on both sides of the equation. Following the procedure for a nonlinear stiffness matrix, the solution at iteration $r-1$ ($\mathbf{U}^{r-1}$) is used to compute $\mathbf{G}$ as follows:

$$[\mathbf{K}(\mathbf{U}^{r-1})]\{\mathbf{U}^r\} = \{\mathbf{F}\} + \{\mathbf{G}(\mathbf{U}^{r-1})\}. \tag{B.15}$$

This expression clearly shows that the radiation boundary condition is an additional source of nonlinearity. For this problem, the direct iteration method was used to solve Eq. B.15. When using an initial temperature equal to the fluid temperature (310 K), the program required fewer than five iterations to converge.

The Abaqus model was created with the parameters that are defined in the Problem Statement. Thermal shell elements with temperature degrees of freedom were used to provide the closest match to the 2D model described above. The temperature was assumed to be constant through the thickness of the elements. The simulation was conducted using a Heat Transfer analysis in Abaqus, which is a nonlinear solution procedure capable of modeling conduction as well as grey-body radiation.

Tables B.2 and B.3 present the numerical results of the verification study for the linear and quadratic elements. The results from the two models agree very closely, giving a high degree of confidence in heat transfer analysis and radiation boundary conditions in Abaqus.

Table B.2: Results of verification study for 16×16 mesh of linear elements.

	T_{min} (K)		$\dot{q}^r_{min}$ (W/m^2)		$\dot{q}^r_{max}$ (W/m^2)		$\dot{Q}^r_{tot}$ (W)	
ϵ	FEM	Abaqus	FEM	Abaqus	FEM	Abaqus	FEM	Abaqus
1.0	288.8035	288.7703	276.5230	276.6314	374.0129	374.0602	688.7791	688.6023
0.9	290.3103	290.2908	261.7469	261.8380	345.7633	345.8144	640.9946	640.9011
0.8	291.8494	291.9047	245.2714	245.3431	315.9798	316.1116	589.6611	589.9552
0.7	293.5940	293.6228	226.8050	226.8631	284.7169	284.7956	535.2470	535.3816
0.6	295.4459	295.4575	206.0097	206.0539	251.6415	251.6846	476.6877	476.7297
0.5	297.4325	297.4236	182.4642	182.4948	216.5516	216.5656	413.5044	413.4656
0.4	299.5159	299.5388	155.6486	155.6678	179.1586	179.1868	344.8952	344.9507
0.3	301.7922	301.8244	124.9192	124.9288	139.2253	139.2471	270.3527	270.4125
0.2	304.2820	304.3067	89.4678	89.4699	96.3751	96.3833	188.8799	188.9062
0.1	307.0087	307.0194	48.2676	48.2658	50.1523	50.1515	99.2610	99.2614

Table B.3: Results of verification study for 8×8 mesh of quadratic elements.

	T_{min} (K)		$\dot{q}^r_{min}$ (W/m^2)		$\dot{q}^r_{max}$ (W/m^2)		$\dot{Q}^r_{tot}$ (W)	
ϵ	FEM	Abaqus	FEM	Abaqus	FEM	Abaqus	FEM	Abaqus
1.0	288.7482	288.7839	286.2065	286.2094	367.1390	366.8545	689.0173	688.6856
0.9	290.2587	290.3026	270.4718	270.4684	339.6006	339.4077	641.2234	640.9932
0.8	291.8024	291.9149	252.9543	252.9508	310.3957	310.5359	589.8797	590.0515
0.7	293.5510	293.6313	233.3905	233.3816	280.2439	280.2691	535.4439	535.4773
0.6	295.4072	295.4643	211.4443	211.4313	248.1922	248.1867	476.8587	476.8197
0.5	297.3979	297.4287	186.7188	186.7030	214.0317	214.0034	413.6425	413.5450
0.4	299.4868	299.5424	158.7266	158.7146	177.4430	177.4514	345.0017	345.0148
0.3	301.7692	301.8266	126.8854	126.8759	138.1973	138.2104	270.4250	270.4579
0.2	304.2658	304.3078	90.4652	90.4576	95.8877	95.8919	188.9188	188.9316
0.1	307.0001	307.0197	48.5538	48.5491	50.0221	50.0200	99.2729	99.2694